# Development of lumped parameters models for aerostatic gas bearings

*Original*
Development of lumped parameters models for aerostatic gas bearings / Moradi, Mona. - (2019 May 15), pp. 1-122.

*Publisher:*
Politecnico di Torino

*Published*
DOI:

ScuDo
Scuola di Dottorato ~ Doctoral School
WHAT YOU ARE, TAKES YOU FAR

Doctoral Dissertation
Doctoral Program in Mechanical Enginering (31.th cycle)

# Development of a lumped parameter model of aerostatic rectangular bearings

## Static and dynamic study

**Mona Moradi**

* * * * * *

**Supervisors**
Prof. Terenziano Raparelli, Supervisor
Prof. Federico Colombo, Co-supervisor

**Doctoral Examination Committee:**
Prof. P.Beomonte Zobel, Referee, Università de L'Aquila
Prof. G.Mantriota, Politecnico di Bari

Politecnico di Torino
February 26, 2019

I hereby declare that, the contents and organisation of this dissertation constitute my own original work and does not compromise in any way the rights of third parties, including those relating to the security of personal data.

. . . . . . . . . . . . . . . . . . . . . . . . . . . . . . . . . . . . . . .
Mona Moradi
Turin, February 26, 2019

# Summary

The main issue of this thesis is the development of a lumped parameters model for dynamic analysis of aerostatic pads with multiple supply holes and rectangular shape. The model starts supposing the pressure distribution under the pad; from this distribution, the lumped pneumatic capacitances and resistances are individuated, then the mass continuity equations are written for each capacitance together with the mass flow balance equations in order to obtain the non linear system of equations that describes the system. Then the perturbation approach is adopted and the dynamic pressures are defined as the sum of the static pressures and the perturbations. Therefore, the system of equations is linearized and the transfer function between the air gap and the load capacity is calculated in Laplace domain. The LP model is applied also for a rectangular aerostatic pad, in a case found in literature, in which only the squeeze effect is analyzed (without supply holes).

The model is validated with a comparison with the distributed parameters model of the pad, which was obtained by discretizing the Reynolds equation and implementing the finite difference approach. An experimental estimation of the static and dynamic characteristics of an aerostatic pad was also carried out for a further comparison with the results of the LP model.

# Acknowledgements

And I would like to acknowledge Prof. Terenziano Raparelli for giving me the chance to pursue my dream and passion in this field under his valuable guidelines. Also, I would thank Doc. Federico Colombo for all his patience and supports during these years. Finally, I would like to acknowledge Prof. Vladimir Viktorov, Doc. Andrea Trivella and all the personnel of laboratory for helping me in accomplishing this career.

*I would like to dedicate*
*this thesis to my loving*
*parents and all people*
*who love and support*
*me unconditionally!*

# Contents

# List of Tables

# List of Figures

# Chapter 1

# Introduction

## 1.1 Motivation

The backbone motivation of this research is to provide a faster and enough-accurate model for simulation of rectangular aerostatic thrust bearings.

As in literature, mainly the study of gas bearings are based on solutions of the Reynolds equation with finite difference, finite elements or Computational Fluid Dynamics (CFD) and although these solutions are accurate, their implementation is not immediate. Therefore, introduction of an accurate faster instrument for study of this kind of bearing can be very useful and efficient especially for designers, when the air pad design is addressed to meet a required load capacity, stiffness and air flow consumption so that the designers may be eager to quickly investigate the influence of changing the design parameters on the behavior of the pad. That is exactly one example to use an efficient lumped model.

The main drawback of the air bearings can be mentioned as low stiffness and damping in comparison with other types of the bearings. In turn, a lumped model can provide a fast way to achieve higher stiffness and damping by changing the pads geometry and performing sensitivity analysis. This sensitivity analysis can later on be used as a fast and enough accurate manual for the designers of the air bearings whenever there is a need of obtaining a fast feedback from the effects of geometrical parameters on the static and dynamic characteristics of rectangular thrust bearings which in turn highly affects their behavior.

## 1.2 Research Objectives

The first part of this thesis is dedicated to development of the lumped model. This is an attempt in order to reduce the calculation time required by distributed models for simulating air thrust bearings. This lumped model is not only faster, but it is also enough accurate by enrolling a correction coefficient it can also simulate properly air pads working on low air gaps. Afterwards, this part of the thesis continues with validating the model by comparing it with a distributed model based on solving the Reynolds equation by means of finite different method. The second kind of validation of the lumped model takes place by considering a rectangular thrust bearing with no supply holes. A pad with the shape ratio (length/width) in the range from 0.5 to 2 was simulated and validated with literature data in the case of a 1D parallel slider. The last part of the validation occurs by comparing the results obtained by the LP model with those of experiments.

On the other hand the second part of the thesis deals with investigating the influences of geometrical parameters of the pad on its behavior by performing some sensitivity studies for both static and dynamic cases. This part can be provided as a fast, enough-accurate and easy to use manual for the rectangular air bearing designers to help them reach their desired characteristics for the pad.

## 1.3 Thesis structure

The layout of this thesis can be described as:

Chapter 2: The literature of gas bearings and the history of Reynolds equation is reviewed. This chapter also discusses the characteristics and various type and performances of gas bearings.

Chapter 3: Development of a new method which is time and complexity efficient to study the rectangular gas thrust bearings in both static and dynamic conditions. The following chapters are aimed to be used as verification of this model.

Chapter 4: A brief description of distributed parameter model implementation for study of rectangular bearings. The results obtained with this model are then compared with those obtained by lumped model.

Chapter 5: Describes the details of performing the experimental test including the static and dynamic test benches and also the experimental equipment.

Chapter 6: Validation of the lumped model is the main subject of this chapter which is achieved by comparing the results obtained by experiments and distributed model with the results of the developed lumped model. This chapter concludes with using the lumped model to perform some sensitivity analysis.

Chapter 7: After validation of the lumped model it is used for study of a rectangular thrust bearing in squeeze condition.

Chapter 8: the conclusion and the further work are discussed.

# Chapter 2

# Review on Gas Bearings

## 2.1 Introduction

It is hard to trace back to who first had the idea of an air bearing. The first patents are related to the beginning of the last century; Westinghouse in 1904, De Ferranti in 1906 and Abbot in 1916. Willis is the first to perform experiments on a radial flow between parallel planes [1], measuring the Bernoulli forces and comparing them with the repulsive force between the planes constituting the externally pressurized thrust bearing. Many externally pressurized air bearings are designed and manufactured in the sixties, for various applications, such as mechanical machining machines, spherical bearings for space simulators and dental drills. The modern production industry require more and more cutting speeds, to be able to use drill bits of lower diameter and to also reduce machining times in milling and grinding. These applications which are very different from each other in terms of the required power, rotation speed and shear forces, are united by the need to obtain high tangential velocities. These speeds entail a rapid deterioration of the normally used rolling bearings. One way to overcome these limits are to use air bearings. The uses of these bearings are very different: dental, textile, food, chemical, electronic, optical, metrological, and robotic. The air bearings can withstand rotating shafts or sliding rails. They are suitable both for high speeds of rotation and for small shifts of precision, even at very low speeds. The industrial use of air bearings is not yet widespread compared to classic rolling bearings, but the market for possible applications are becoming more and more numerous both for the production needs that have a higher speed objectives and for the consolidation of the knowledge of these bearings that is going to be stating over time. A real, easily usable design algorithm does not yet exist, due to the problems related to the instability and the prediction of the dynamic behavior of the rotor-bearings system. Traditional applications include the use of oil-lubricated rolling bearings, and they present the drawback of rapid deterioration at high speeds. This wear involves the imposing of the bearings with high frequencies, causing a significant increase in the maintenance costs of the machine. There are several alternative solutions, depending on the needs of the various fields of application. The most widespread solution seems to be the use of hybrid bearings with ceramic spheres that their characteristic of being harder than steel also guarantees a longer life. When a fluid is interposed between the rotating surfaces in a relative motion the friction is less than that which is present in the direct contact (dry friction) or in the contact with the interposed rolling objects (rolling friction). This is the case with hydrodynamic bearings, where thanks to the incompressibility of the oil and the possibility of reaching pressures of even 200 bar, high stiffness is obtained, with a dissipation still comparable to rolling bearings. If we compare the viscosity of the oil with air, the latter is 4 orders of magnitude lower than the first. It is therefore understandable how they can satisfy the needs of low wear and dissipation, for the high speeds. The need of rotating organs with low friction and wear, high speed and precision, repeatability of positioning and high reliability are becoming more and more frequent in industrial applications and air bearings can be the solution for many of these problems. The pneumatic solution offers a number of advantages over classic bearings due mainly to the physical properties of the air, which replaces traditional lubricating fluids. The salient features of the pneumatic bearings can be mentioned as the ability to operate at high temperatures, low friction and wear and no contamination of the environment. Unlike liquid lubricants, the chemical-physical characteristics of the air are maintained unchanged for a wide range of temperature and speed. This concludes into power saving due to the reduced friction, and also lower power needed in the cooling system because of the lower temperatures reached. The operating cost of these components is therefore low both in terms of energy and maintenance. These devices can operate for a long time without maintenance even in difficult operating conditions (at high temperatures or in radioactive environments). Also the use of air (unlike oil) does not constitute contaminant, and the absence of stick slip permits infinitive motion resolutions and high positioning repeatability. A problem not to be underestimated in the design of pneumatic bearings is the possible emergence of instability. The increase in the speed shows a self-excited phenomenon that brings the rotor to collide on the supports. This phenomenon is called "whirling instability" and in most cases it is destructive since the accumulated energy of the rotor is such that in case of contact with the fixed parts the temperature locally grows to melt the materials and to weld fixed and movable parts together at the contact point . The speed at which this phenomenon occurs is "threshold speed" and its value depends on the mass of the rotating parts The technical solutions adopted to increase the instability threshold are: bearings with modified geometry, foil bearings, pivot, with damping elements in general. The damping introduced by these elements causes transition of a part of the energy from the rotor to the bearing to be dissipated and thus the instability is reduced as well.

## 2.2 History of fluid film lubrication

Friction and wear have generated drastic economic damages and environmental problems through history. The mechanical and thermal severities caused by friction along with the consequent wear are some of the most relevant issues faced by engineers in machine design. Different kinds of lubricants and coatings are adopted solutions for reducing friction and avoiding wear. Gas lubricants make it possible to significantly reduce friction and wear because of their remarkable performance, and therefore providing systems with high positional accuracy and low environmental impact. Hence, gas lubricated systems are employed for high-precision applications.

### 2.2.1 Fluid mechanics

Leonhard Euler (1707-1783) was the founder of the fluid mechanics although Daniel Bernoulli (1700-1782) was the first to publish a book in the field. Euler provided the continuity equation and motion equations for non-viscous flows. Jean Léonard Marie Poiseuille (1799-1869) analyzed the properties of viscous fluids. He performed experimental investigations on human blood flow. Gotthilf Heinrich Ludwig Hagen (1797-1884) independently achieved the same results during his study on the fluid flow within brass tubes therefore nowadays this formula is known as Hagen-Poiseuille's law. In the same period, Claude Louis Navier (1785-1836) along with Sir George Gabriel Stokes took advantage of Euler and Poiseuille's contributions to provide one of the milestones of fluid mechanics known as Navier-Stokes Equations used for modelling the viscous fluids motion.

$$\begin{cases} \rho\dfrac{Du}{Dt} = \rho X - \dfrac{\partial P}{\partial x} + \mu\Big(\dfrac{\partial^2 u}{\partial x^2} + \dfrac{\partial^2 u}{\partial y^2} + \dfrac{\partial^2 u}{\partial z^2}\Big) \\ \\ \rho\dfrac{Dv}{Dt} = \rho Y - \dfrac{\partial P}{\partial y} + \mu\Big(\dfrac{\partial^2 v}{\partial x^2} + \dfrac{\partial^2 v}{\partial y^2} + \dfrac{\partial^2 v}{\partial z^2}\Big) \\ \\ \rho\dfrac{Dw}{Dt} = \rho Z - \dfrac{\partial P}{\partial z} + \mu\Big(\dfrac{\partial^2 w}{\partial x^2} + \dfrac{\partial^2 w}{\partial y^2} + \dfrac{\partial^2 w}{\partial z^2}\Big) \end{cases} \tag{2.1}$$

### 2.2.2 Lubrication theory and reynolds equation

Gustave Adolphe Hirn (1815-1890) was the first who investigated the frictional properties of different kinds of fluids. He performed many experiments on fluid bearings by testing twelve natural oils, air and water as lubricants. Hirn's studies were refined by Robert Henry Thurston (1839-1903) who showed that, giving an increasing speed, the friction coefficient within a fluid bearing initially decreases below its static value, and reaches its minimum and then increases to a constant value. He also noted that the value of the minimum friction coefficient varied together with the applied load. Tthis research was finalized by the Nikolay Pavlovitch Petroff (1836-1920) who performed further viscosity measurements with the aid of an experimental apparatus similar to the one employed by Poiseuille. He provided the first analytical formulation for evaluating friction coefficients in the presence of hydrodynamic lubrication. Petroff was not able to find the relation between the load carrying capacity of a fluid bearing and the friction.

Beauchamp Tower (1845-1904) was the first who explained the conceptual relationship between friction and the load carrying capacity. He developed a test rig to measure the friction of a fluid lubricated bearings and concluded that the shaft rotation pressurized the oil film, which provides a load carrying capacity for the bearing. Additionally, Tower obtained the first map of hydrodynamic pressure by use of several pressure gauges installed on the bearing surface. Although Tower performed a great research in the field but he was not able to describe the pressure gradient in the lubricant film. In 1886, Osborne Reynolds reviewed Tower's reports and he combined continuity equation with a simplified format of Navier-Stokes equations, and obtained a set of partial differential equations to compute the pressure distribution within lubricants. He considered a Cartesian reference frame where $x$ and $z$ were the axis parallel to the bearing surface and $y$ was the direction along the lubricant film thickness $h$.

$$\frac{\partial u}{\partial x}+\frac{\partial v}{\partial y}+\frac{\partial w}{\partial z}=0 \tag{2.2}$$

$$\begin{cases} \dfrac{\partial P}{\partial x}=\mu\dfrac{\partial^2 u}{\partial y^2} \\ \\ \dfrac{\partial P}{\partial y}=0 \\ \\ \dfrac{\partial P}{\partial z}=\mu\dfrac{\partial^2 w}{\partial y^2} \end{cases} \tag{2.3}$$

Where, $P$ and $\mu$ are the pressure and viscosity of the lubricant, while $u$, $v$ and $w$ are the velocities respectively along $x$, $y$ and $z$ directions. It was also considered that fluid film thickness is small compared to dimensions of the bearing in addition as weight and inertial terms were small in comparison with viscous ones, they were neglected and by considering the case of incompressible lubricant (oils) and the following boundary conditions:

$$\begin{gathered} y=0, \qquad u=U0, \qquad w=0, \qquad v=0 \\ y=h, \qquad u=U1, \qquad w=0, \qquad v=U1+\frac{\partial h}{\partial x}V1 \end{gathered} \tag{2.4}$$

Afterwards, the well-known Reynold's Equation was obtained:

$$\frac{\partial}{\partial x}\Big(h^3\frac{\partial P}{\partial x}\Big)+\frac{\partial}{\partial z}\Big(h^3\frac{\partial P}{\partial z}\Big)=6\mu\Big[(U_0+U_1)\frac{\partial h}{\partial x}+2V1\Big] \tag{2.5}$$

Reynolds made it possible to identify the bearing load carrying capacity, including Poiseuille, Couette and squeeze effects. The Poiseuille term describes the net flow rates due to the pressure gradient within the lubricated area, while the Couette and the Squeeze terms describe the net entering flow rates due to respectively the tangential and normal velocities of the interacting surfaces. Although Hirn was the first to use air as a lubricant, Albert Kingsbury (1863-1943) is considered as the father of gas lubrication as he accidentally discovered that gas films exhibit load carrying capacity while he was performing frictional measurements on his screw threads device.

He is supposed to be the first one who designed an air bearing in history. Once he made sure that pressurized air gaps could bear loads, he designed a fine air bearing device

Kingsbury [2] recognized the existence of a center pressure and oppressed this insight to perceive the first tilting pad in history (1898). This bearing had pivoted surfaces around the center of pressure so that because of the asymmetric shape of the pressure distribution, they can automatically provide a convergent gap and increase the carrying capacity (Figure 8a).

In parallel to Kingsbury research, Anthony George Maldon Michell [3] filed a similar patent in 1905 (Figure 9). In addition, Michell solved the Reynolds' equation for the case of an inclined rectangular block sliding over a plane surface with finite width. It was a three-dimensional solution which provided the possibility to evaluate the effects of side leakage for the first time [4].

Many studies consisted of trying to solve Reynolds' equation in presence of further hypotheses and different boundary conditions.

Sommerfeld [5] obtained an explicit analytical expression for pressure distribution, load locus of shaft center and friction which were used by W.J. Harrison [6] for deriving the basic equation today known as Harrison's Equations. Rather than considering a constant density, Harrison combined Reynold's and gas equations under the assumption of isothermal conditions, and obtained:

$$\frac{\partial}{\partial x}\Big(\frac{h^3}{\mu}\frac{\partial P^2}{\partial x}\Big)+\frac{\partial}{\partial z}\Big(\frac{h^3}{\mu}\frac{\partial P^2}{\partial z}\Big)=12U\frac{\partial Ph}{\partial x} \tag{2.6}$$

Harrison was not able to obtain a closed form analytical solution due to nonlinearity of his formulation, and by applying Runge-Kutta's method he achieved an approximated solution. By 1921, Stone [7] designed a thrust bearing. It was an air bearing with a glass thrust collar and a quartz shoe. for the first time it was possible to measure the air gap thickness by an optical interferometer bands. Another valuable study on the oil whip phenomenon was performed in 1925 by

Stodola and Newkirk [8] describing it as a vibration occurring due to the spinning of the shafts above their critical speed because of the stiffness and damping of the bearings. This insight raised a new field of research that today is known as rotordynamics. In the period of second world war, the only worthy work on the subject was Swift's work [9] who rearranged Reynolds' equation to extend it to cases where dynamic loads are applied to bearings which made it possible to carry out the first stability analysis. He also provided one of the first optimal designs for fluid bearings.

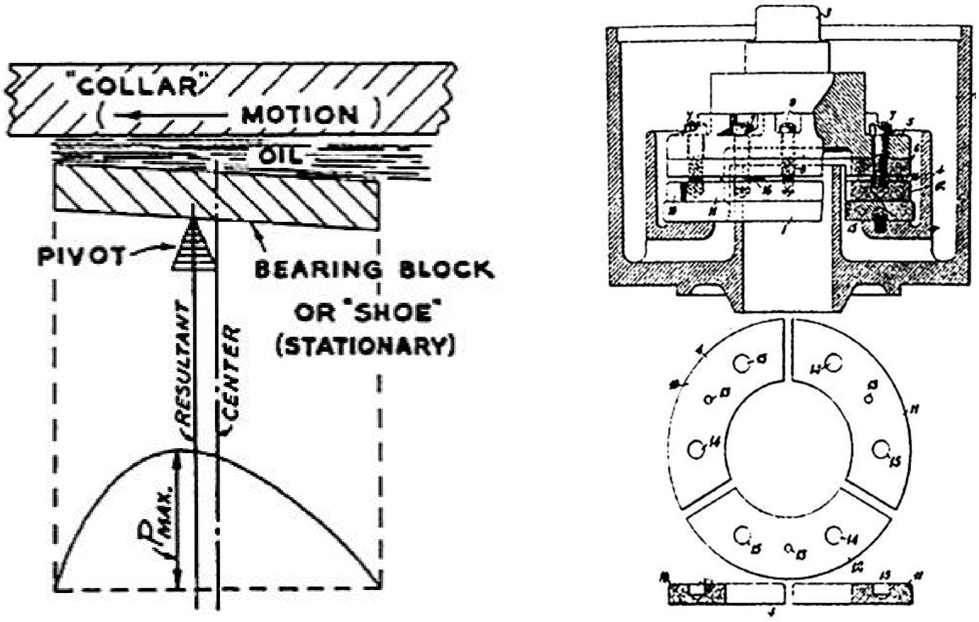

(a)

(b)

Figure 2.1: (a) Sketch of the pressure distribution and (b)Sketch of Kingsbury's tilting pad [2].

In the fifties, thanks to the low influence of temperature variations on air properties, the small viscosity changes over a wide range of temperature, low tendency to change in phase and exhibit cavitation; aerostatic bearings were successfully employed for different applications and a large interest was formed for using air bearings because of their particular features according to the industrial requirements. In addition, because of the low changes in viscosity with temperature variations and almost zero friction and wear, gas bearings were effectively used in high speed spindles and metrology. The birth of gas technology field as an independent field can be mentioned as 1959, when the First International Symposium was held in Washington where various activities and the future directions of gas lubrication technology were defined.

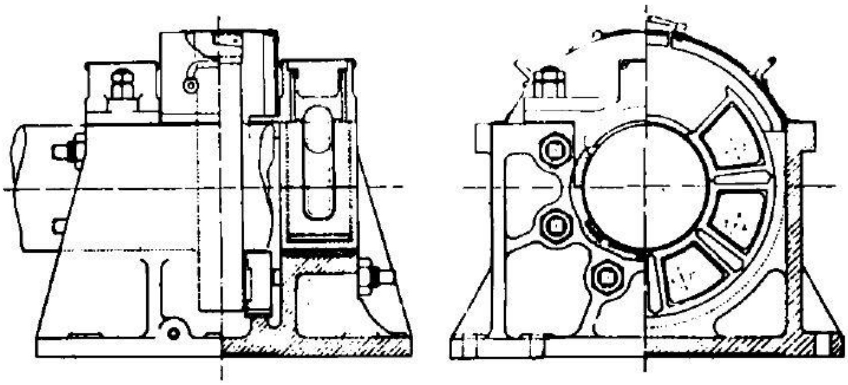

Figure 2.2: Michell's thrust bearing, used in the early merchant marine installation [3].

The increasingly demand for ultra-precise supports and positioning systems to produce large hard disk drives and semiconductor parts was another thriving force behind the boom in gas lubrication was . In 1957 Roudebush [10] developed one of the first investigations on the influence of geometrical parameters and temperature over bearing performance. Several linearized models were proposed in order to study the dynamic performance of both journal and thrust bearings.

In the period between the sixties and seventies, Journal of Lubrication Technology was initiated and Gross ("Gas film lubrication") [11] and Powell ("Design of aerostatic bearings") [12] provided two of the most important milestones of gas bearing designs.

## 2.3 Definition of air bearing

Figure 13 presents a sketch of a conventional aerostatic thrust bearing with a thin air gap which separates the floating bearing 1 and the stationary part 2 with its associated block diagram. Donald and Wilcock [13] employed a new method to study behavior of the bearing with the idea of control theory by considering bearings as closed loop servo-systems.

The air is pressurized by a compressor up to the supply pressure $P_s$ and passes through the bearing before being exhausted by the restrictors. the air flows through the bearing and it gradually reduces its pressure to $P_c$ close to the restrictor area and finally to the atmospheric pressure $P_{Amb}$ at the outer edge of the bearing. This pressure distribution can be estimated by a mean pressure $P_m$ which multiplied by the bearing area provides the ability to balance the load F applied on the bearing. When the bearing is subjected to increasing (decreasing) load variations the air gap reduces, providing an increase (decrease) of the mean pressure that permits the

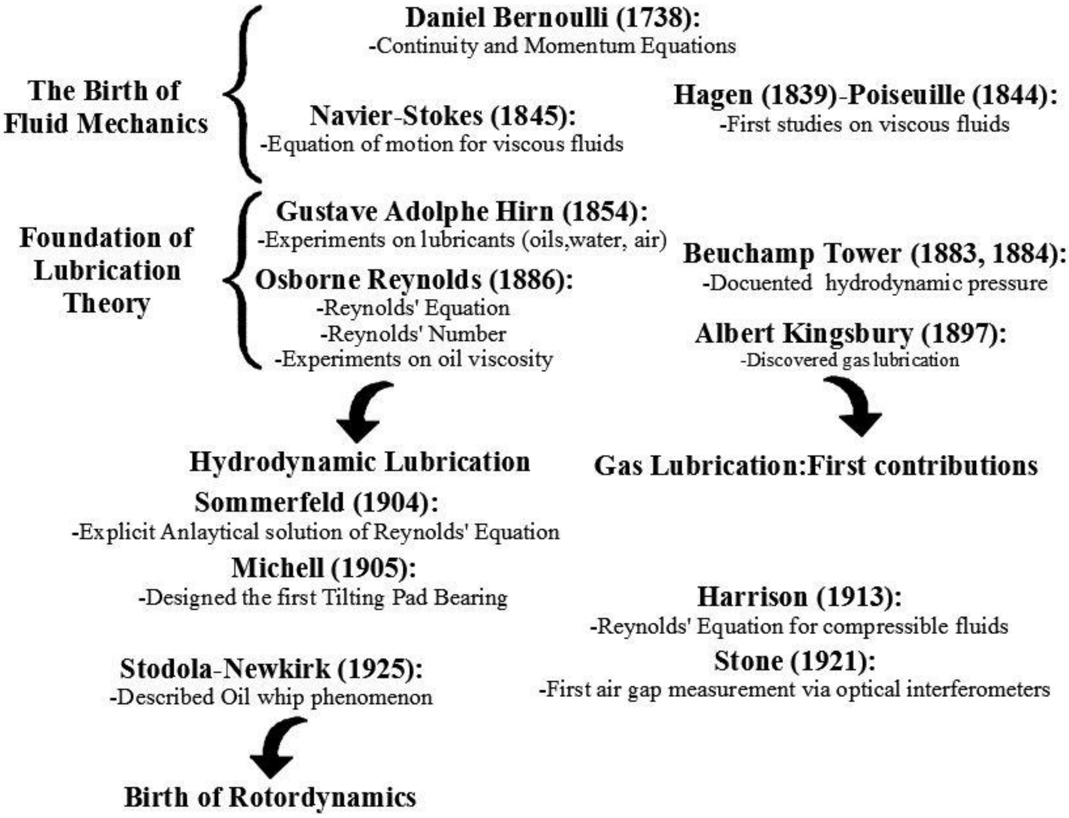

Figure 2.3: Historical perspective regarding lubrication theory and fluid mechanics between 1738 and 1925.

compensation of the load variations. An example of these block diagrams is shown in Figure 2.4 (b) where all variables are expressed as functions of time t. This block diagram consists of a direct branch that comprises the inertial transfer function $G_m(t)$, which embodies the masses of the bearing and the supported structure and, a whole feedback branch which represents the air gap transfer function given by the product of the transfer function $G_(P/h)(t)$ [14, 15, 16]. The external force variation $\Delta F(t)$ is the input to the bearing that produces the air gap variation $\Delta h(t)$ that is the output. The relation between input and output depends on the inertial transfer function $G_m(t)$ and the equilibrium conditions are reached when the difference between the external force $\Delta F(t)$ and the bearing force variation $\Delta F_b(t)$ is null. The variation of the bearing force $\Delta F_b(t)$ is given by the product of the air gap pressure variation $\Delta P_c$ multiplied by the bearing surface.

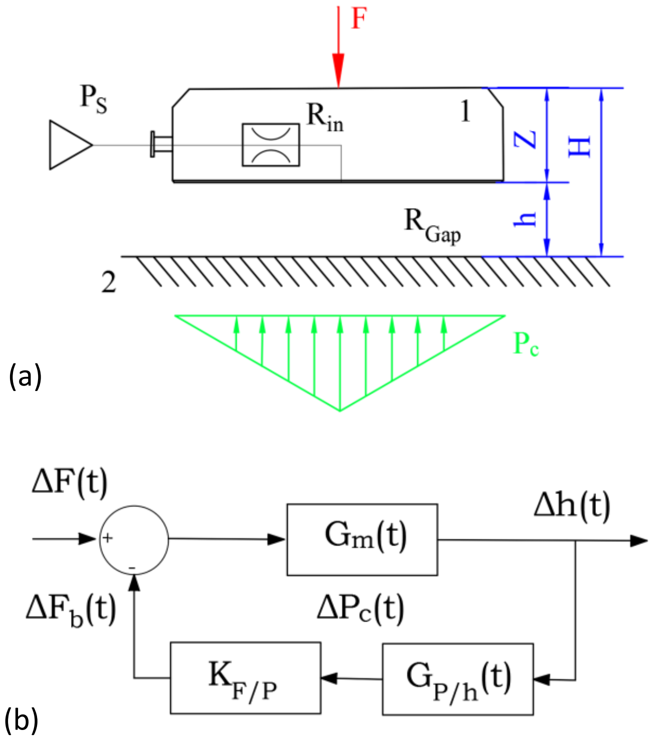

Figure 2.4: (a) Schematic representation of an aerostatic thrust bearing (b) Closed-loop servo model of a conventional gas bearing.

## 2.4 Application, advantages, disadvantages, hazards

Aerostatic thrust bearings offer some distinct advantages in comparison with contact bearings as there is no contact between the moving and stationary parts, linear positioning control is not affected by the highly nonlinear friction forces, and high precision positioning or high speed can be achieved. Furthermore, the use of air bearings usually does not contribute to the environmental contamination. Their maintenance and environmental advantages are due to the fact that no lubrication is needed. Aerostatic bearings are often found in high precision applications, such as machine tools, measuring instruments such as coordinate measuring machines (CMM), precise positioning systems, manufacturing and medical equipment and wafer-steppers. However, these capacities have not been fully utilized because air bearings are difficult to manufacture and need extensive calculations for investigating their behavior. In addition, the main drawbacks of aerostatic bearings are low stiffness and damping in comparison to contact bearings, so that their application in some sectors, e.g. machine tools, is less popular.

### 2.4.1 Advantages

As air bearings work without contact the only present friction is due to the flow of the air in the gap. Thus, the durability of air bearings is unlimited if they are accurately designed and maintained. The perfect combination of acceleration and precision (repeatability and positioning) offers very high productivity of machines in the semiconductor and electronics industry. There are lots of applications which require high repeatability and accurate positioning. For example in the chip production, repeatability accuracy of 1-2 $\mu$m must be reached with the wire bonder. At the die bonder, even 5 $\mu$m must be achieved. With such a precision, roller bearings reach their physical limit without a lower acceleration. Due to the lack of wear, accuracy is maintained throughout the entire life of the bearing and is the reason why air bearings have very high repeatability. Air bearings can provide motion repeatability of less than 1 $\mu$m. In lots of applications e.g. chip-on board, flip-chip technology or wafer-level-chip packaging, a repeatability accuracy of less than 1 $\mu$m is required. Roller bearings do not achieve this because of their Stick-slip phenomenon and “a tight drawer” effect. In general, productions of air bearings are performed in clean rooms, and presence of dirt and particles may cause defects and costs. Within the electronic production, cleanliness requirements increase with the implementation of small components. Other than oil, air is the perfect lubricant, and no costly sealing of the bearing is necessary with lubricant. Moreover, due to elimination of oil it is also environmental friendly.

### 2.4.2 Disadvantages

The most important issues is the high geometrical accuracy required during manufacturing process. Another issue is the supplied air which has to be clean and dry. Fundamentally, air bearings require some form of power consumption during operation to supply the high pressure air, unlike mechanical systems which may operate without any power input (except mechanical forces). In addition, low stiffness and damping in comparison to contact bearings is another noticeable defect. To increase the stiffness and load capacity of the air pads, active and passive compensation can be adopted to enhance these properties [17]. Active compensation methods require feedback, such as the air gap height or the pressure inside the air gap from the pad during the working process, which is performed by piezoelectric and it is costly.

### 2.4.3 Hazzards: The phenomenon of instability

An important problem in the design of pneumatic bearings is related to their stability specially for journal bearings. Generally in fixed geometry journal bearings there is a speed limit beyond which the shaft precession becomes unstable with consequent failure. Consider a rigid rotor mounted on fixed bearings, symmetrically rotating and symmetrical with respect to the rotor's center of gravity. Both the precession of the rotor axis can be expressed through only two degrees of freedom (cylindrical motion). The mass of the rotor and the supply pressure of the bearings are given. Suppose further that the static imbalance is null so as to discern the phenomenon of the instability of the bearing from instability due to an excessive imbalance. If you move the rotor axis by a certain amount from the center, at low speeds it is noted that the precession of the axis is a spiral that tends to the origin. By accelerating the rotor, a velocity range is reached in which a circular orbit, also known as the limit cycle, is obtained, for which there is a balance between the radial force (with zero attitude angle) and the centrifugal force. At speeds above a certain limit, this orbit becomes a divergent spiral and the so called whirl fractional frequency is completely developed. It is a self-excited phenomenon produced by the bearing itself. The speed at which this phenomenon occurs is called "threshold speed" and its value depends on the mass of the shaft. When the rotating shaft is in coaxial position with its bearing moved by an external force, due to the created eccentricity, there is a variation in the geometry of the gap which is no longer of a constant height along the entire circumference of the bearing. This involves a variation in the pressure range which gives rise to a reaction force which opposes the movement of the shaft. In Figure 2.5 the position of the center of the bearing is indicated with O and A is the position of the shaft axis subjected to an external load W, the reaction force $F_P$ is given by the air pressure inside the gap because of the rotation of the shaft $\omega$, which generally is not parallel to the straight line passing through OA but is inclined by an angle of $\beta$ called angle of attitude. The tangential component $F_{Pt}$ is responsible for increasing the rotor momentum and thus provides energy to the system. When the rotation speed of the shaft reaches the value of the threshold speed instability is established with a vibration frequency equal to half of the shaft rotation frequency and with an uncontrolled increase in the amplitude of the spiral orbits until the contact of the shaft with the bearing is occurred, resulting. Instability can therefore occur with cylindrical or conical vibrations of the shaft axis with respect to the bearing axis.

## 2.5 Classification of gas bearings

Gas lubricated bearings mostly use air, resulting in the prefix aero-, while other kind of gasses are used for specific applications. In addition, another distinction is the method of pressure generation which is either generated by relative movement of bearing surfaces, with suffix -dynamic, or is inserted externally, with suffix -static, therefore air bearings can be divided into three categories:

- Externally pressurised or aerostatic bearings

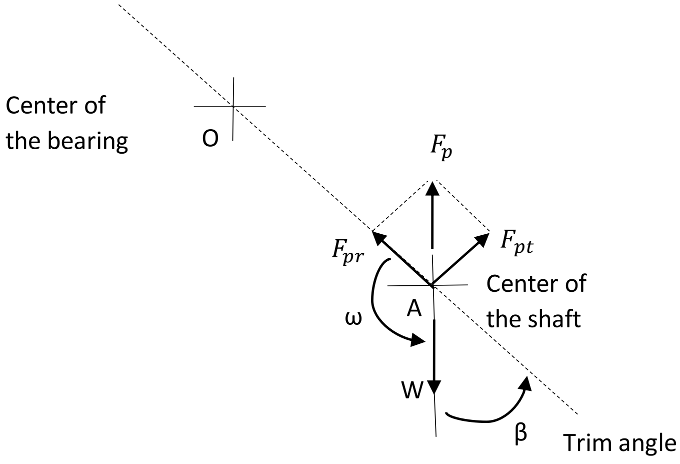

Figure 2.5: Position of the shaft moving inside the journal bearing.

- Self-acting or aerodynamic bearings
- Hybrid bearings, which are combinations of aerostatic and aerodynamic bearings

Externally pressurised gas bearings are used most frequently. In such bearings, a compressed gas (normally air) is used to generate the force which is needed in bearing to prevent contact between the surfaces. In aero dynamic bearings, this force is generated because the bearing surfaces suck the gas into a converging gap and meanwhile compress it. In hybrid bearings, such as radial face seals, a groove profile is put on the bearing surfaces to increase, for example, the stiffness of the bearing. Normally, the compressed air is supplied by use of a compressor. A key goal for designing the air pads is that the stiffness and damping of the air pad reaches the highest possible level. In addition, air consumption and uniformity of air supply into the gap are crucial characteristics which can affect the behaviours of air bearings. The fields in which gas bearings are used can be classified into two groups: high speed applications and high precision positioning systems. There are five basic types of aerostatic bearing geometries [18]:

- Radial bearings
- Vacuum preloaded bearings
- Slider bearings
- Flat bearings
- Air bushings

- Spindles

### 2.5.1 Radial bearings

Radial air bearings are widely used in rotary machinery as they provide frictionless rotary motion. In this sense, they are comparable to flat bearings, though the surface is curved. In addition, all the advantage of regular air bearings such as no friction, no wear, no need for lubrication, excellent velocity control, no noise, high speed and high precision are preserved in this type of bearings. These characteristics make them suitable for various range of rotary applications and they are available in concave and convex configurations.

Figure 2.6: Radial air bearing

### 2.5.2 Vacuum preloaded bearings

Vacuum Preloaded air Bearings (VPLs) are like flat air bearings. The only difference is that vacuum is employed to generate preloading of the bearing against the guide surface. When Appling preload is challenging or not possible, vacuum preload could be used as a viable solution. Since the vacuum and air pressures could be adjusted separately, various combination of fly height and stiffness are achievable. As a result, VPLs could be used in numerous industries with different applications.

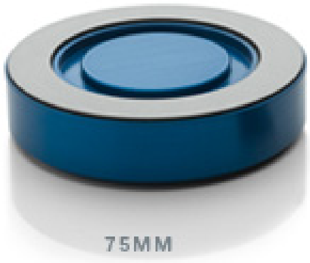

Figure 2.7: Vacuum preloaded air bearing.

### 2.5.3 Slider bearings

This kind of bearings are complete slide assemblies with the technology of flat pad integrated into a package of compact air bearing slide.

There are various configuration of the Slider bearings. In comparison with other types these bearings are more expensive according to the fact that they are fully assembled, with air bearings integrated into their surfaces. Slider bearing are generally supported with different methods including supports at the ends, or fully supported according to the required range of stiffness.

Figure 2.8: Slider air bearing.

### 2.5.4 Flat bearings

Flat Bearings are available in different shapes, e.g. round and rectangular. They are comparable with usual rolling element bearings in every aspect. One of the main advantages of flat bearings is that they can be quickly replaced; therefore, they are suitable choices to be utilized in prototype designs. Also, as their assembly is easy, they are a reliable option when complex assemblies and precision machined guide ways are needed. Besides being inexpensive, they have high stiffness; consequently, an optimal choice for highly-loaded applications.

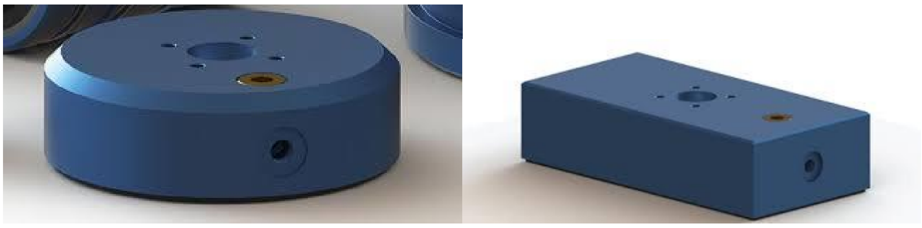

Figure 2.9: Flat air bearings.

### 2.5.5 Air bushings

Air bushings could be considered as an affordable alternative to conventional rolling element bearings. When precision motion is needed for linear or rotating movement of shafts, air bushings are an ideal choice as guide ways. These bushes are advantageous as they are readily available in different sizes that fit standard shafts. The air is distributed through the face of the bushing and there is no content between surfaces; therefore, high rotational speed is achievable.

Figure 2.10: Air bushings.

### 2.5.6 Spindles

Usual spindle designs include lubrication to separate the two components in relative motion. But air bearings spindles provide frictionless motion as there is an air gap between the moving parts. Air spindles provides high stiffness and minimize the wear as there is no contact. Therefore, it is widely used in rotary equipment and due to their excellent rotational accuracy, they are a good choice for high speed precision applications.

Figure 2.11: Spindles.

## 2.6 Restrictors

The type of the restrictors deeply affects the air pad performance. There are different types of restriction which are explained in more details in following [19]:

- Discrete orifice feeding
- Porous surface
- Partial Porous surface
- Slot feeding
- Groove feeding

It is noteworthy to mention that the choice of the restrictor highly depends on the type of the desired application.

### 2.6.1 Discrete orifice feeding

Discrete orifice feeding is the simplest type of air feeding for the thrust bearings that results in low manufacturing costs. In this type one or more small holes are featured at the face of the air bearing which restrict air flow to the film. This method can provide very small flying height variations from bearing to bearing. Flat air bearings utilizing orifice may have tilts of less than 0.1 microns. Although they are not as robust as the porous carbon type, orifice air bearings can be made to have fewer than five 0.1 micron particle emissions per minute.

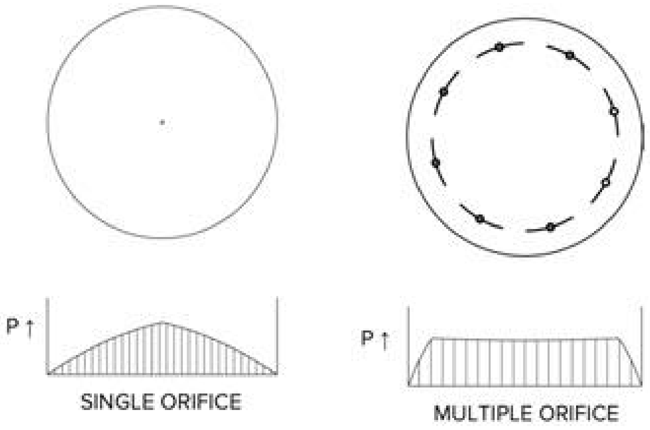

Figure 2.12: Pressure distribution over two air bearings with discrete orifice feeding.

### 2.6.2 Porous surface

In case of conventional orifice compensation method there is always the need to balance the bearing size with the right number, size, and distribution of supply holes to maintain the practical stability of the pad. In some cases grooves might be added in order to distribute the pressurized air evenly across the bearing surface. The disadvantages of adding a groove can be mentioned as the presences of scratched surface near to an orifice might cause some drastic changes in the balance of the bearing, which in turn can lead to fail even with a normal feed pressure. The technology of a porous media provides the compensation using the millions of sub-micron-sized holes which make it possible to have much greater control of the air-flow through the gap. In this type of bearing, the air flows to the gap and is restricted by a porous material such as carbon, bronze, or other material. This type of bearing provides the best pressure distribution and therefore has a slightly higher load capacity and stiffness. In the case of porous carbon, accidental contact of the mating surfaces during relative motion will not cause a large degree of performance loss of the bearing. However, due to the manufacturing process of the porous material, this type of bearing may emit very small particles during operation. This may not be desirable in cleanroom environments like those used in semiconductor wafer fabrication. Figure 2.13 provides a schematic comparison of the pressure distribution of different types of grooves and supply methods versus a porous surface bearing.

### 2.6.3 Partial porous surface

While in orifice type air pads the pressurized air is fed through one or a number of precise orifices, in this particular type a portion of the air bearing surface has a porous material allowing air to flow. The surface contains microscopic holes, which are inherent in the bearing material. This combination of a solid and porous surface can provide higher damping during dynamic conditions. The inlet ring shown here provides an even source of air distribution. Properly controlling the permeability of the porous material over the proportionally small area is difficult and often requires a valve or other restrictor integrated within the housing to adjust the flow rate. This type of bearing provides the best pressure distribution and therefore has a slightly higher stability, load capacity and stiffness. In the case of porous carbon, accidental contact of the mating surfaces during relative motion will not cause a large degree of performance loss of the bearing. However, due to the manufacturing process of the porous material, this type of bearing may emit very small particles during operation. This may not be desirable in cleanroom environments like those used in semiconductor wafer fabrication. The damping can be negative under high supply pressures. Belforte et. al.[20] performed theoretical and experimental investigations of porous resistances to calculate permeability and

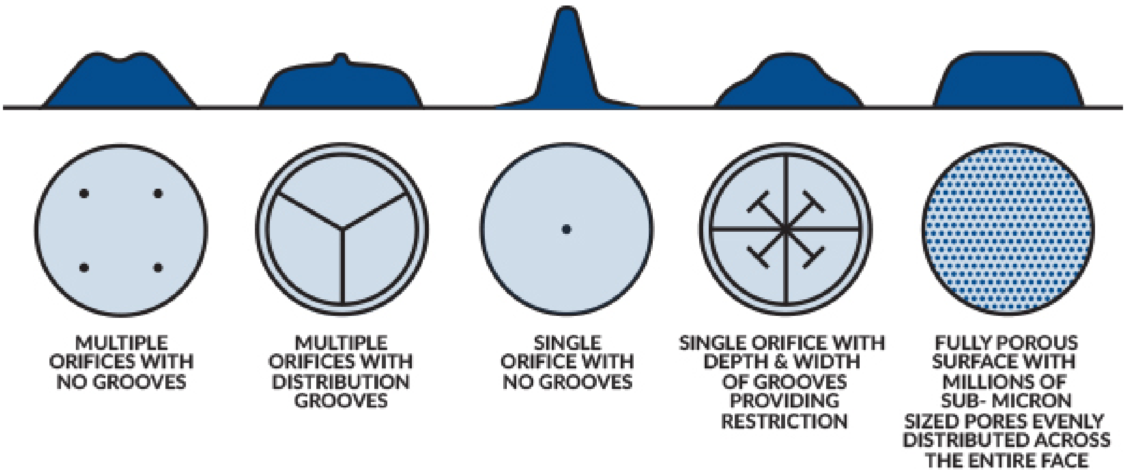

Figure 2.13: Pressure distribution comparison among different types of orifice bearings vs a porous surface.

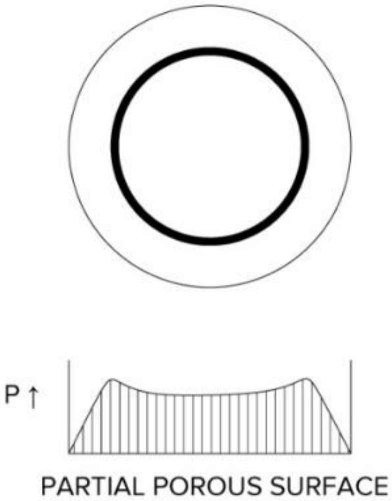

Figure 2.14: Pressure distribution over a partial porous surface air bearing.

the inertial coefficients. The results validated use of Forchheimer's law for porous resistances used in gas bearings and thrust pads supply systems.

### 2.6.4 Slot feeding

This type of air inlet is similar to orifice air bearings but in place of a small hole is a rectangular slot. Often used in cylindrical journal air bearings, this type of air distribution is more uniform and more calculable than orifice bearings. Slot feed air bearings have higher stiffness at high eccentricity positions of the journal shaft. They tend to be more costly to manufacture in small quantities.

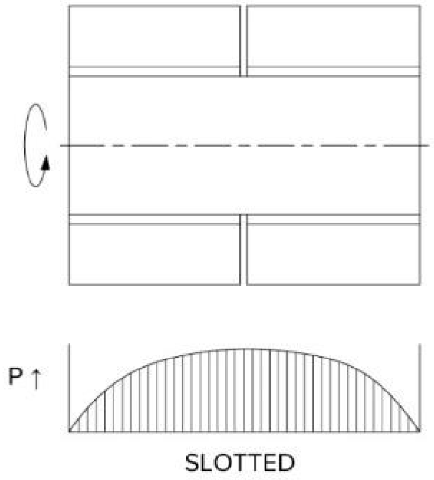

Figure 2.15: Pressure distribution over an air bearing with slot feeding.

### 2.6.5 Groove Feeding

Also utilized in cylindrical journal air bearings, multiple small grooves are manufactured axially into the bearing surface leading from an air source volume near the center of the journal. This method can result in very high stiffness and symmetrical air flow distribution within the film but it can be more costly than orifice or slot feeding air bearings. It is interesting to notice that presence of groove cause a continuous increase of the pad's load carrying capacity at different air gaps without presenting a local maximum which is always present for the pads without grooves. This study also shows that the air flow consumption for a pad with grooves is higher, but it is not much higher which means that an increase in the air flow is less evident than the increase of the load carrying capacity or the stiffness. It should be taken into account that the grooves with too large width or depth may cause pneumatic hammer.

## 2.7 Compensation methods

Compensation methods are the alternative solutions to overcome the main drawbacks of air pads such as low stiffness and damping. To raise the limits of air bearing performance, the first compensation strategies were developed with the aim to improve the bearing performance by suitably modifying their feeding system and structure. These methodologies include three main categories: passive, active and semi-active compensations. Passive compensation strategies make it possible to improve the bearing performance by using only passive devices, such as valves, elastic orifices, which exploit only the energy resulting from the bearing supply air. Due to their simplicity and ease of integration, these were the first adopted compensation strategies. Conversely, active compensation is achieved by employing active elements for example actuators, sensors and controllers that require external sources of energy for their performances which provides satisfying results, for both static and dynamic situations but they are generally very expensive. Pure pneumatic control is an interesting alternative solution in terms of performance and cost. Because of the lack of the electronic feedback system in this method it is called semi-active controlled system.

### 2.7.1 Passive compensation methods

Most of the passive compensation methods employ movable orifices, compliant elements, diaphragm valves and disk-spring damper compensators to compensate for load variations. They mainly modify the pads behavior by changing the shape of the bearing or adding different types of pockets or grooves with various depth and widths to the bearing. Using elastic orifices was one of the first passive compensation strategies, employed by Newgard et al. [21] in 1966. Elastic orifices can suitably adjust the exhausted air flow from the bearing, and compensate the load variations. Figure 2.16 (a) illustrates the arrangement of an elastic orifice working

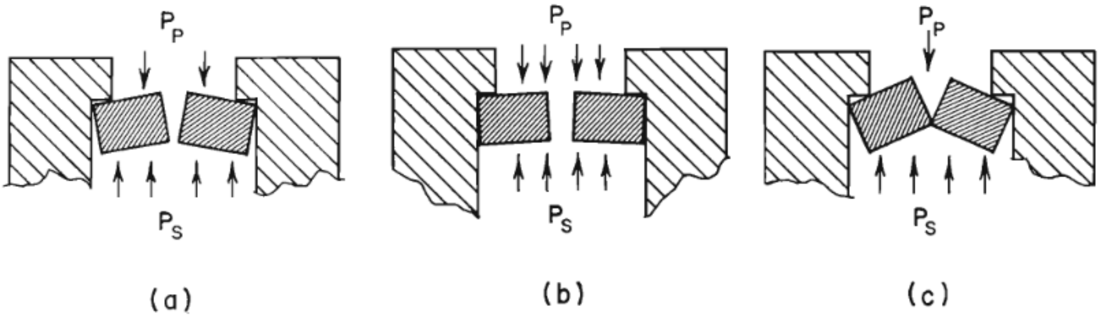

Figure 2.16: Working principle of an elastic orifice. (a) Nominal operating conditions (b) Higher loads (c) Lower loads [21].

under standard operating conditions. The orifice is embedded into the bearing in such a way that its diameter can enlarge up to its maximum dimension when the air gap pressure increases (Figure 2.16 (b)). On the other hand, when the external load decreases, the initial air gap height is restored because the lower air gap pressure deforms the orifice producing reductions of the air flow exhausted from the bearing.

Many other authors were inspired by this operating principle to exploit the deformation of elastic members for developing further compensation strategies. During the following International Gas Bearing Symposiums (the fifth, sixth and seventh), Kilmister [22], Rowe et al. [23] along with Lowe [24] proposed the first bearings with compliant surfaces, whereas Blondeel et al. [25] provided a procedure for their design calculations.

In 1974, Cusano [26] proposed an externally pressurized journal bearing that employed elastic membranes to vary bearing exhausting flow, and compensating load variations.

Chen et al. [27] designed an X-shaped grooved bearing with an embedded disk spring damper compensator. As illustrated in Figure 2.17, the bearing consists of two parts that are connected via a spring damper compensator. The presented numerical and experimental studies that were carried out demonstrated that the compensator provided significant performance improvements especially in the presence of the compensator, the bearing exhibited shorter transient and lower amplitude of oscillation as in Figure 2.17 (b). In a study performed by Belforte et al. [28] the performance of the circular grooved and plane aerostatic thrust bearings were compared and it was found that the pad with groove (Pad 2) has larger load carrying capacity than the pad with groove (pad 1) especially at low air gaps mainly less than 10 $\mu$m where stiffness is also much higher. In addition, the air flow consumption of the pad with grooves is increased but not much which shows that the increase in air flow is less evident than the load capacity or the stiffness. It is noteworthy that in high clearances the difference of the load capacity and stiffness between pad 1 and 2 decreases.

The influence of adding pocket Figure 2.19 to the pad orifices and the effects of pocket diameter and depth on load carrying capacity of aerostatic thrust bearings was investigated by Long and Bao [29] using finite volume method. In addition, pressure distribution is an important parameter in design of aerostatic bearings which is also dependent on the shape of the air gap. Different studies investigated the influence of conical shape which can significantly increase the stiffness. In addition, damping and load carrying capacity of the pad also increases with this modification of the air gap shape but pneumatic hammer is very frequent in his type of bearings. Figure 2.20 compares different shapes of the bearings and the air gap.

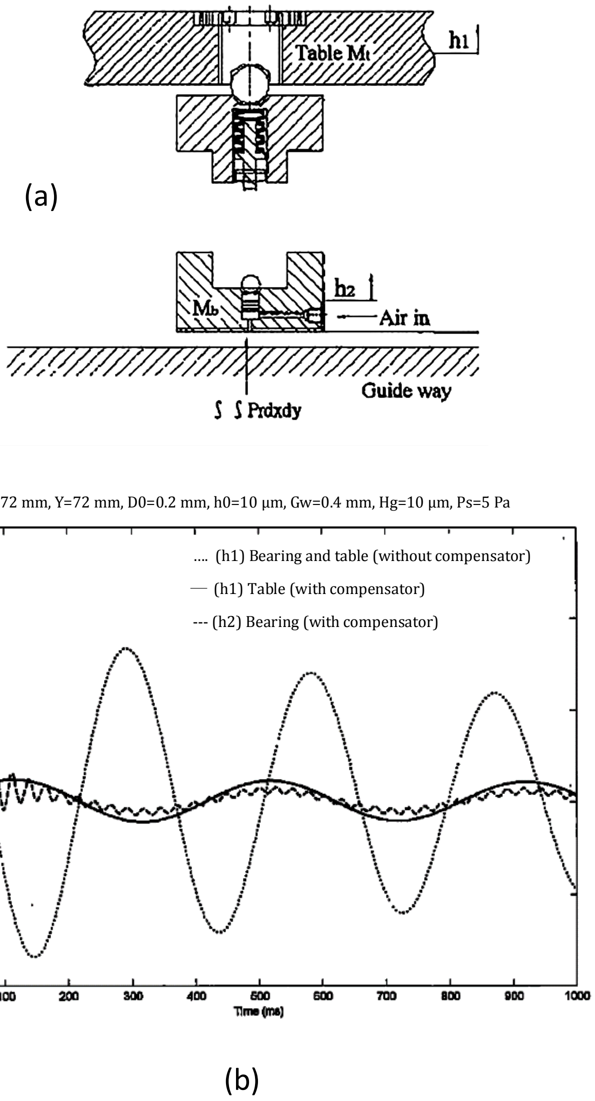

Figure 2.17: The aerostatic thrust bearing with a disk spring damper designed by Chen et al. (a) Functional scheme and (b) Experimental results [27].

### 2.7.2 Active compensation methods

Although passive compensation methods are cheap and simple, their performances are limited therefore active compensation methods were introduced. As discussed before, these methods consist of using active devices as actuators, sensors and controllers to obtain actively compensated systems.

Most of these solutions exploit piezo-actuators because of their higher dynamic, power density and efficiency. However, also magnetostrictive, electromagnetic and pneumatic actuators were successfully adopted. Regarding the sensor employed to

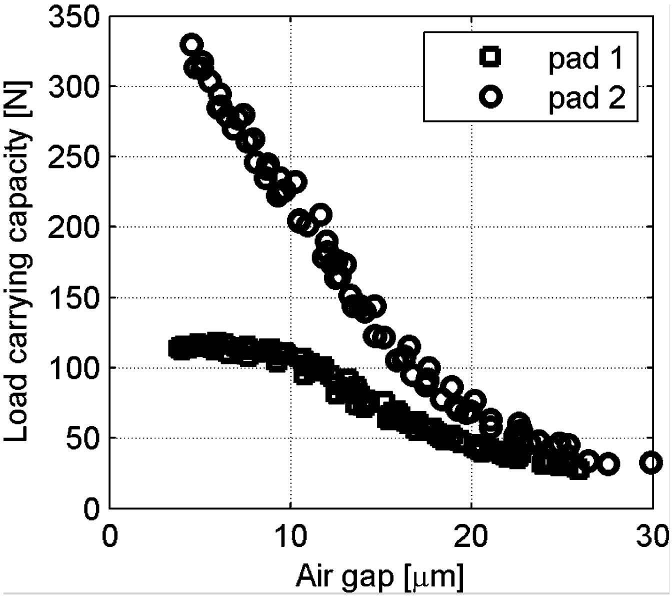

Figure 2.18: Static load capacity versus air gap with the supply pressure of $p_s$= 0.6 MPa comparison for grooved and plane pads [28].

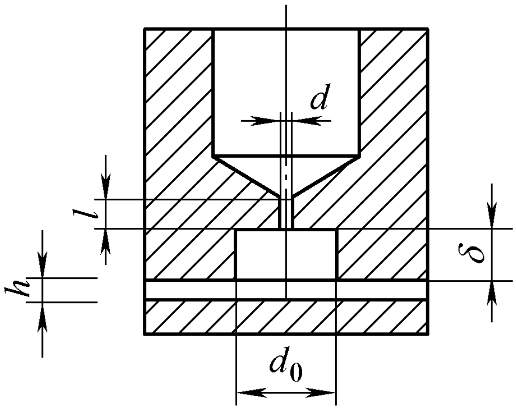

Figure 2.19: Structure of orifice-type system with feeding pocket [29].

obtain feedback on the bearing operating position, capacitive, eddy current and optical sensors are usually integrated.

To control the air flow and change the pressure distribution of the air bearings, generally there are four main methods: 1. Upstream active restrictors 2. Orifices restrictors 3. Exhausting restrictors 4. Active geometrical compensation

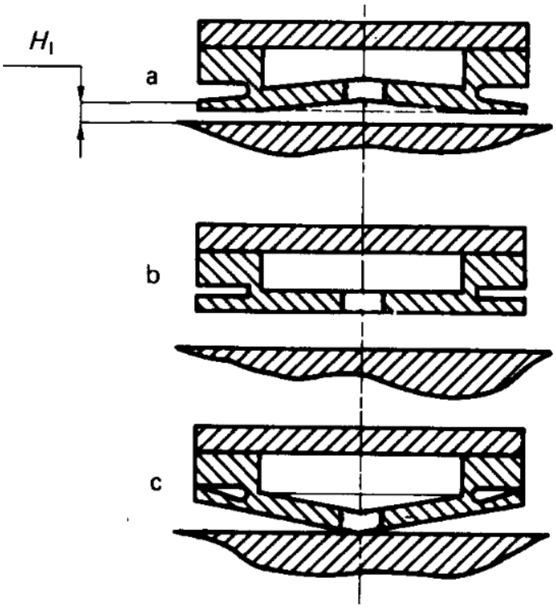

Figure 2.20: Different shapes of air bearings.

### Upstream active restrictors

There are several researches [30, 31], in which the upstream restrictors were used as an active compensation. This type uses the piezoelectric restrictors upstream to each orifice, separately, and the result presents the significantly improvement of the damping of the system and also the range of bearing application. Figure 2.21 presents the injection system used in this study where an O-ring was used to minimize the exhaust of air in the lower surface of the pin. With change of the size of piezoelectric the air gap pressure can be modified without any change of the shaft position.

### Orifices restrictors

This type employs a piezoelectric actuator to change the area of the pad orifices [32]. When the applied load increases, the air gap pressure also increases due to enlargement of the pad orifices area, therefore the system returns to equilibrium without changing the air gap.

### Exhausting restrictors

This type employs a piezoelectric actuator to control the bearing exhausted flow [33]. When the external load increases, the size of exhausted area is reduced by the piezoelectric action. Therefore, the pressure on the bearing surface can be increased without reducing the air gap. The air gap variation is measured by

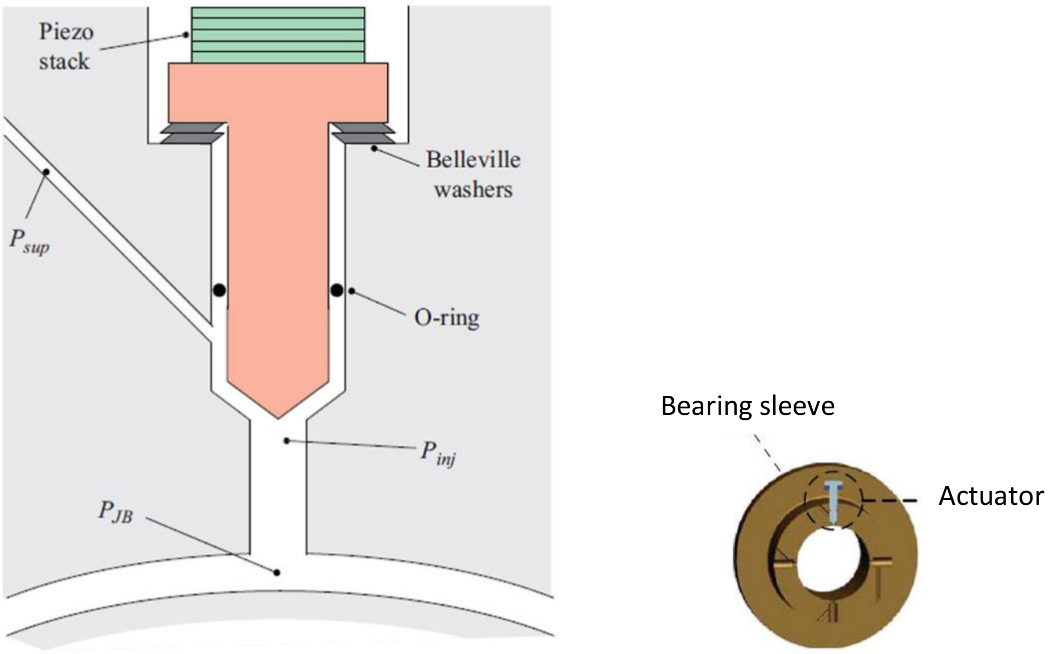

(a) The injection system designed by Morosi

(b) 3D view of the piezoelectric injection system

Figure 2.21: (a) The injection system used to feed the hybrid journal bearing by Morosi et al. and (b) 3D view of the piezoelectric injection system [30].

electrical micrometers, and an appropriate voltage is computed by a microcomputer and supplied to an amplifier which controls the piezoelectric actuator. Chen and Lin [27] also developed an X-shaped groove aerostatic bearing with a semi-active disk-spring compensator and the bearing damping was improved.

### Active geometrical compensation

The main example of this type of compensation is active air bearings designed by Gorka et al. [34]. In this type a thrust air bearing consisting of a thin plate with a central air feed hole is presented. The pressure distribution in this pad changes with the deformation of the bearing surface to a concave shape by use of three piezoelectric actuators. The induced deflection produces a distribution variation in air gap pressure and therefore, a variation in the bearing force which results in an increase of the bearing stiffness. This method provides satisfying results in terms of the stiffness, load carrying capacity and damping. Colombo et. al. [36] studied a new method for active compensation. In this strategy, the system's

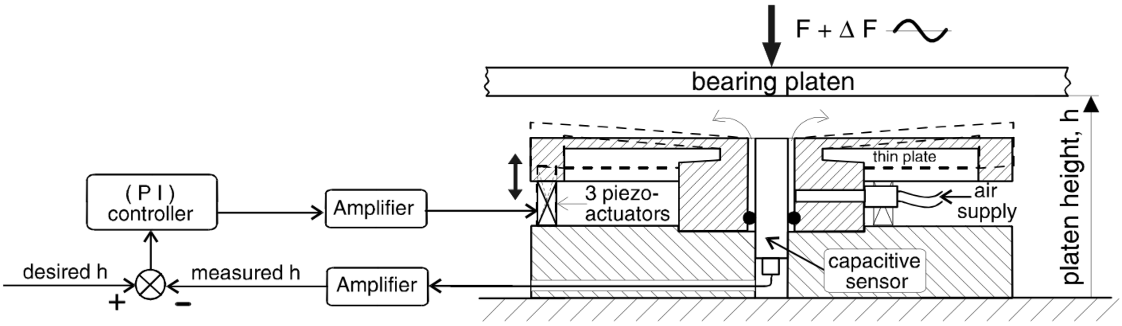

Figure 2.22: Sketch of the active aerostatic bearing with a conicity control [35].

initial working position is restored by compensating the air gap variations through adjustments of the bearing vertical dimension. The described bearing consists a conventional thrust bearing which is integrated with a multilayer piezoelectric actuator, a compliant mechanism and a digital controller. In this method, When the force F increases (decreases) by dF, with a constant supply pressure P , H also decreases (increases) by dH as a result of the air gap reduction and structural deformations. The initial value of the controlled height H is restored through the PZT stretching/shrinking action which depends on the driving voltage applied at its terminals as presented in Figure 2.23. The system presents promising results in both static and dynamic behavior. Hybrid active compensation methods are a combination of the two previously discussed methods. The main contributors in designing such a hybrid systems were Al-Bender et. al. [35, 34, 37]. They developed a convergent gap thrust bearing where air gap conicity and supply pressure can be simultaneously modified via piezo actuators, displacement capacitive sensors and a PID controller. Figure 21 illustrates a sketch of this active solution and the related block diagram Figure 2.22.

### Semi-active compensation

Active methods require electronic devices such as sensors, piezoelectric actuators and controllers that are efficient but also economically costly. Semi-active control is an interesting alternative solution in terms of performance and cost and can be successfully adopted to create an overall cheaper systems. These systems are defined as semi-active ones since they do not use any external energy (i.e., electrical energy). In these systems normally, something is added to the air bearing which helps to control the air flow similar to the performance of pneumatic valves. Ghodsiyeh et al. [38] developed a pure pneumatic control valve designed to increase the stiffness of the thrust aerostatic bearing. In this system as the force on the pad increases, the air gap decreases and pressures $P_m$ and $P_V$ increase. Consequently,

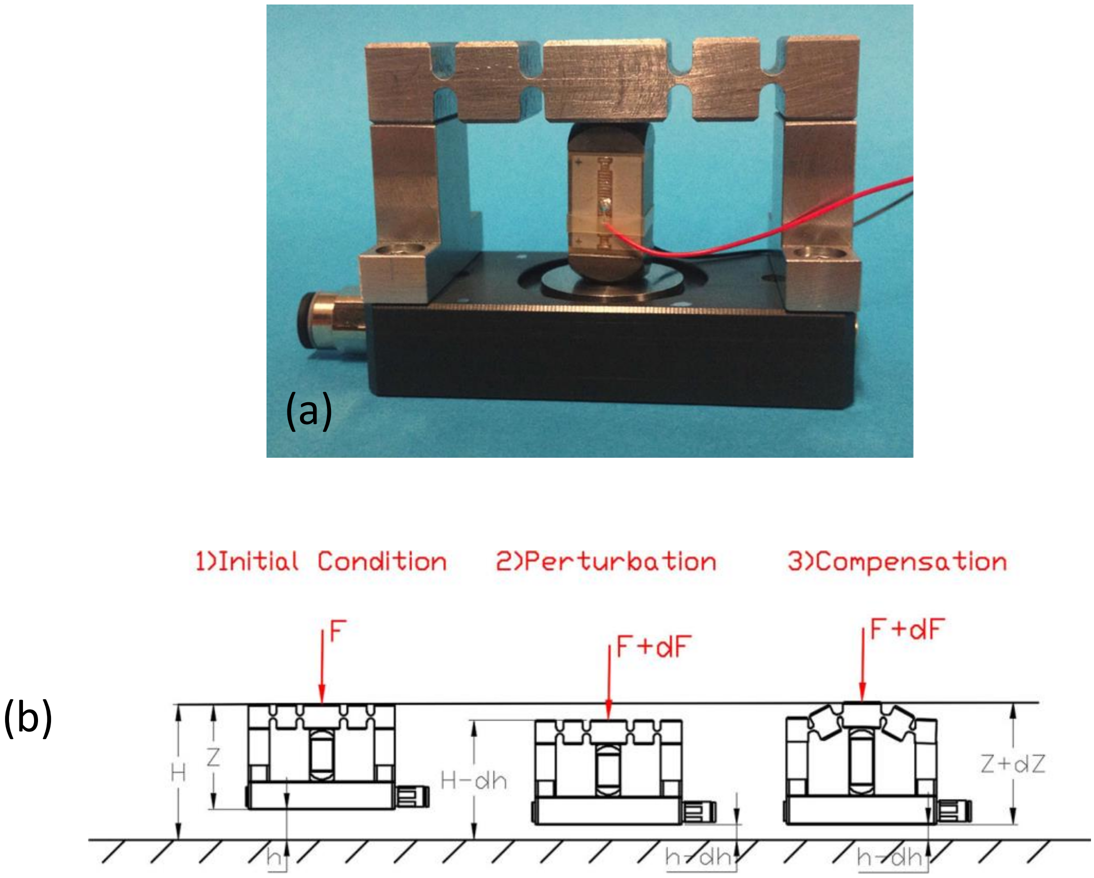

Figure 2.23: The actively compensated air pad used by Colombo et al. [36].

the diaphragm deforms more until the pad reaches a new equilibrium position. The main variables of this system are the nozzle diameter ($d_v$), membrane thickness ($S$) and initial position of the nozzle ($X_0$) Figure 2.24. It was found that the experimental static stiffness of the controlled pad is approximately 40% higher than those of the commercial pad.

### 2.7.3 Future perspective

The accuracy of current numerical models along with the integration of active compensation systems represent a solid base to improve further air bearing performance and try to extend their use to many others micro and nano-applications. Indeed, air bearings are an efficient and environmentally friendly solution regarding positioning systems. Air bearings can be adopted in harsh environments providing zero loss, friction and wear. Nowadays, the major obstacle in developing these

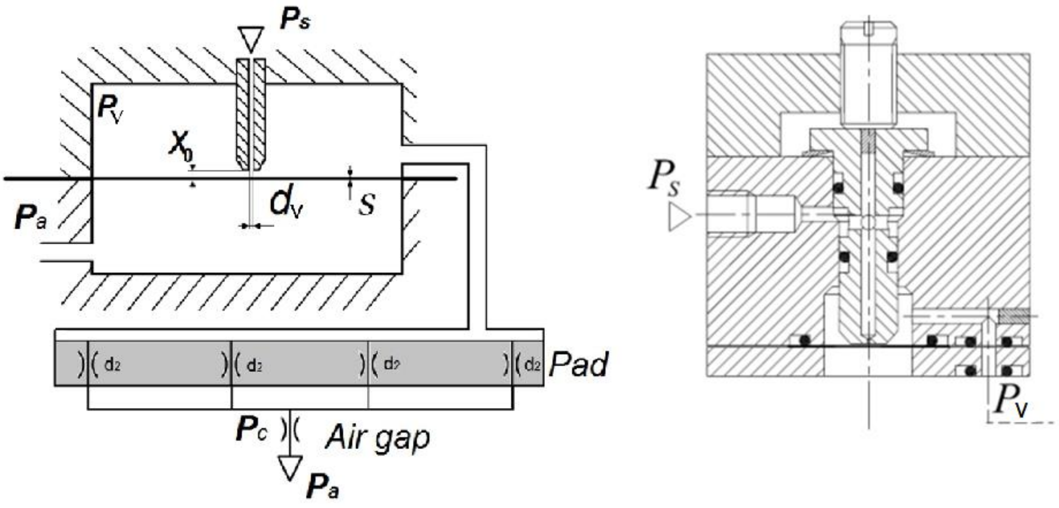

(a) (b)

Figure 2.24: Sketch of the control valve semi-active compensation used by Ghodsiyeh et al. [38].

tribotronic systems is the cost of these complex systems. However, technological progress and its continuous upgrade offer the hope that these costs may be significantly reduced in the future. Despite this, air bearing technology is anyway moving forward. One of the most recent idea is by the New-Way company, which is trying to use gas bearings as alternative turbochargers for auto-vehicles. This kind of application is promising to remarkable future advantages. The use of air in place of oil may minimize costs, emissions and maintenance time and simultaneously increase vehicle performance.

## 2.8 Conclusion

Friction and wear are tribological phenomena that have produced significant economic damage and environmental issues throughout our history. Because of their remarkable performance, using gas-lubricated systems represents a worthy and eco-friendly solution to reduce losses, wear and friction within machine elements.

This chapter has presented a historical review of gas lubrication from its accidental discovery until today. The review first has considered the milestones of fluid mechanics, i.e., mass conservation and momentum equations, which made possible the birth and development of gas lubrication technology. The chapter has concluded by analysing the newest methodologies that are currently employed for enhancing the performance of gas lubricated systems. Because of their features, these solutions may be considered as potential applications in a new field, which is called Tribotronics. The aim of this branch of Tribology is to integrate mechatronic devices with conventional tribological systems for controlling their behaviour, thus achieving higher performance and accuracy. It is hoped that this new insight, combining knowledge of the fields of tribology and mechatronics, will push the boundaries of current technology and will be a significant step towards the reduction of the costs and the alleviation of the environmental issues associated with tribological phenomena.

# Chapter 3

# The Lumped parameters model [1]

## 3.1 Introduction

Thanks to their very low friction, aerostatic bearings are widely employed in precise positioning systems as coordinate measuring machines (CMM) and linear guides in machine tools. In the sixties, CMM and metrology applications were revolutionized by the presence of air bearings. Some example of using this kind of bearings in the industry can be mentioned as optical spectrometry and grinding, large format digital printing, automotive suspension testing and frictionless high performance positioning.

As air bearings suffer from relatively low stiffness and damping, numerous works were conducted in the last decades to analyze static and dynamic behavior versus different type of feeding systems to improve the performance. This latter changes occurred significantly with the selected type of feeding systems, e.g., simple [40] and pocketed orifice [41], grooved thrust surfaces [42, 43], porous resistances with sintered powders and woven metal wire [44, 45].

Although experimental study represents the most reliable tool for investigation of the air bearings design, numerical models are also an advantageous tool for the static and dynamic study of air bearings characteristics such as load capacity, air flow consumption, stiffness and damping [46, 47, 48, 49, 50].

In Distributed Parameters (DP) models the solution of the fluid problem is based on the integration of Reynolds equations with finite elements [51, 52], finite differences [49, 53] or finite volumes method; alternatively, computational fluid dynamic (CFD) methods [54, 55, 56, 57, 58] are employed. The results obtained with these methods are accurate, but the models require a relatively long time of the process due to the discretization of the air gap in small elements. The computation time can be drastically reduced by means of lumped parameters models (LP). In

---

[1] “Part of the work described in this chapter has been previously published in Ref. [39]”

LP models, the Reynolds equation is integrated on a few numbers of volumes with proper shapes, depending on the particular study case. This yields to design and optimization processes which are faster and simpler with respect to DP models, even if less accurate.

To solve the problem of accuracy, LP model can be endowed with corrective coefficients derived from a needed identification process with experimental or numerical results. In this way, it is possible to reduce the equations to only a few units in order to obtain a very rapid computation with acceptable accuracy.

For instance, in [59] an LP model was developed to describe the nonlinearities effect of a bearing, and in [60] an LP model was used to investigate the behavior of a porous gas thrust bearing; the results were compared and validated with the experimental ones. Concerning a fast and accurate method for the design of a pneumatic control system, an LP model was introduced in [61]. Moreover, in [62] a static LP model was used to investigate the best design configuration of an externally pressurized gas bearing. In [63, 64], lumped models for rectangular grooved air pads were used for static and dynamic studies. To investigate the dynamic stiffness and damping of a grooved rectangular pad, in [65] a simple LP model was adopted.

In all these LP models, reduction of the number of the discretization elements allows to simply describe the system calculating few unknown parameters. Consequently, the sensitivity analysis with respect to some geometrical parameters becomes very simple to be performed. In [65] an LP model was developed to investigate a rectangular air pad with multiple inherent orifice restrictors in steady-state conditions. In that model, the supply holes were positioned on a rectangular perimeter at the same distance $l$ from edges of the pad. Distance $w$ between two consecutive supply holes were constant. The influence of the number of holes, diameter, and the ratio $\frac{w}{l}$ on the static behavior of the air pad was analyzed. In the adopted model the viscous resistance of the air gap was considered only outside of the supply holes rectangular area, this approximation did not affect the static behavior of the air pad, but made it possible to underestimate the correct stiffness and damping in dynamic performance.

The aim of this chapter is to analyze the dynamic behavior of the rectangular air pad studied in [65] in steady-state conditions. In addition, this developed lumped model also takes into account the air gap resistance inside the rectangular area of the supply holes. The volume of the air gap under the pad is divided into two zones: inside and outside areas. A piecewise linear pressure distribution is supposed to act under the pad.

The perturbation method has been applied by linearizing the mass conservation equations. Afterward, the transfer function between the air gap height and the pad load capacity is obtained in order to relate stiffness and damping coefficients to the geometrical input parameters. Successively, an identification procedure was adopted to improve the accuracy of the model by comparing it with a previously verified dynamic DP model [66], and experimental tests. A sensitivity analysis of the dynamic performance of the pad respect to some geometrical parameters was then carried out. The novelty of this paper respect to the studies found in literature up to now, can be represented by the definition of the transfer function between the air gap $h$ and the load capacity $F$ in closed form. The coefficients of this transfer function are expressed as a function of the geometrical parameters.

## 3.2 The model

A rectangular pad with dimensions of $Lx$ and $Ly$ and multiple supply holes is considered, see Figure 3.1. The supply holes are assumed to be distributed on a rectangular perimeter situated at distance $l$ from the borders of the pad. $w_x$ and $w_y$ are the distances between the supply holes in horizontal and vertical directions respectively.

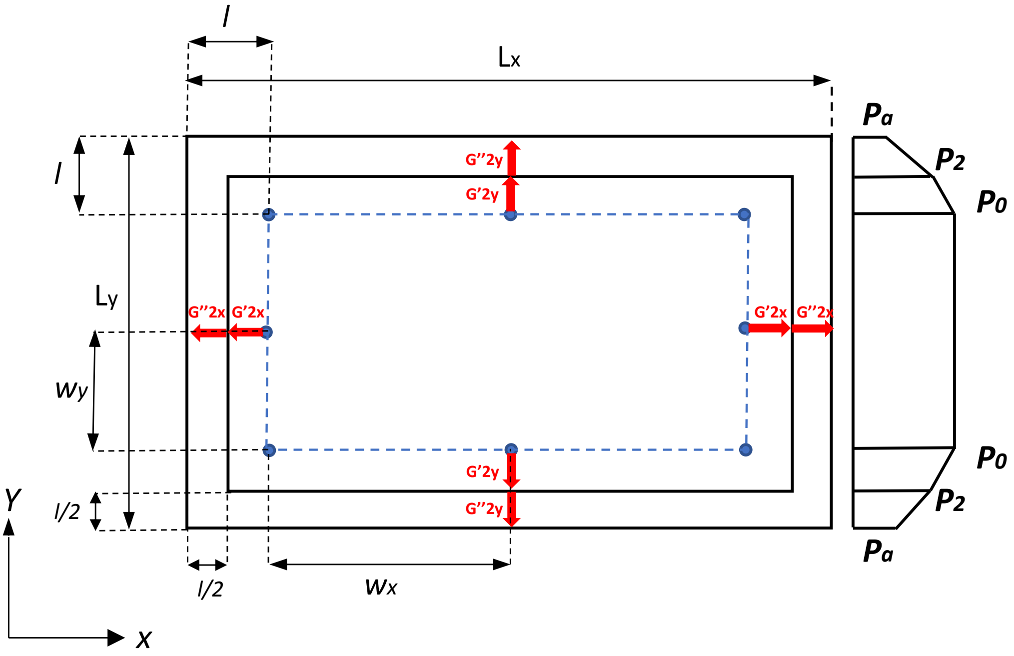

Figure 3.1: Sketch of the pad with static pressure distribution.

The geometry of the pad can be defined by three dimensionless parameters $\alpha, \beta$

and $\gamma$:

$$\begin{aligned} \alpha &= \frac{l}{L_x} \\ \beta &= \frac{L_y}{L_x} \\ \gamma &= \frac{w_{average}}{l} \end{aligned} \tag{3.1}$$

where $w_{average}$ is the average of $w_x$ and $w_y$ which are the distance between supply holes respectively in x and y directions. The aspect ratio $\beta$ is defined in the range $0 < \beta \leq 1$, while $\alpha$ should be in the range $0 < \alpha < \frac{\beta}{2}$. Moreover, the number of supply holes in $x$ and $y$ directions are given by:

$$\begin{aligned} N_x &= \frac{L_x - 2l}{w_x} + 1 \\ N_y &= \frac{L_y - 2l}{w_y} + 1 \end{aligned} \tag{3.2}$$

Therefore the total number of supply holes of the pad is

$$N_{tot} = 2N_x + 2N_y - 4 \tag{3.3}$$

### 3.2.1 Static condition

In the static condition, the pressure distribution under the pad is assumed according to Figure 3.1. Inside the indicated rectangular supply perimeter, the pressure is supposed to be uniform and equal to $p_0$, while outside it decreases to ambient pressure $p_a$. At distance $l/2$ from the edges of the pad pressure $p_2$ is defined. The output resistance is divided into two terms in series; the first resistance is crossed by flow $G'_{2x} + G'_{2y}$, the second one by $G''_{2x} + G''_{2y}$ as depicted in Figure 3.1. The input air flow through the supply orifices is obtained by multiplying the isentropic expansion flow by the discharge coefficient $c_d$, as in [67]. When the supply hole downstream pressure $p_c$ is less than $b \times p_s$, where $b = 0.528$ is the critical ratio, the flow is sonic:

$$G_{in} = c_1 k_T c_d p_s \tag{3.4}$$

where $k_T$ is the temperature ratio defined as $k_T = \sqrt{\frac{T_0}{T}}$, $ds$ is the supply hole diameter, $c_1$ is the conductance, given by

$$c_1 = N_{tot} \frac{\psi \pi d_s^2}{4} \tag{3.5}$$

where

$$\psi = \frac{0.685}{\sqrt{RT}} \tag{3.6}$$

and $R$ is the gas constant equal to 287 $\frac{\text{J}}{\text{kgK}}$. The standard condition is defined as $T_0 = 293.5$ K and $p_0 = 100$ kPa. In subsonic conditions ($p_c > p_s b$) the flow is

$$G_{in} = c_1 k_T c_d p_s \sqrt{1 - \phi^2} \tag{3.7}$$

where pressure ratio $\phi$ is

$$\phi = \frac{\frac{p_c}{p_s} - b}{1 - b} \tag{3.8}$$

$p_c$ is the supply holes downstream pressure and $b$ is the critical pressure ratio equal to 0.528. As discussed in [68], the mean pressure $p_0$ defined inside the rectangular supply area is related to the supply holes downstream pressure $p_c$ by:

$$\frac{p_0}{p_c} = 1 - 0.148\gamma \tag{3.9}$$

Discharge coefficient $c_d$ is defined using an experimentally obtained formula by Belforte et al. [69]. From this formula, the discharge coefficient depends only on the ratio between the air gap and the supply hole diameter and does not depend on the geometry of the pad, assuming that the holes are enough far from each other. This assumption should be valid when the distance between the holes is at least 5 to 10 times the holes diameter. In this study, the effect of Reynolds number on discharge coefficient is not considered, as in most of the cases it is negligible. This allows a simplification of the linearization process performed in further steps. Therefore, the following simplified formula is used to calculate the discharge coefficient:

$$c_d = 0.85(1 - e^{-8.2\frac{h}{d_s}}) \tag{3.10}$$

where h is the air gap under the pad. The formula for isothermal viscous flow in rectangular channels is used [70] to calculate the flow rates per unit of the width:

$$g = \frac{h^3}{24\mu RT}(\frac{p_{in}^2 - p_{out}^2}{l}) \tag{3.11}$$

where $\mu$ is air viscosity and $l$ is the length of the channel. Consequently, according to Figure 3.1 the air flow exhausting from the supply rectangle in steady-state condition is:

$$\begin{gathered} G_{out} = G_2' = G_2'' \\ G_2' = 2(G_{2x}' + G_{2y}') = \frac{h_0^3}{6\mu RT}\left(p_0^2 - \frac{p_0^2 + p_a^2}{2}\right)\frac{L_x + L_y - 4l}{l} = c_2 h_0^3 (p_0^2 - p_a^2) \end{gathered} \tag{3.12}$$

where

$$c_2 = \frac{1}{12\mu RT}\frac{L_x + L_y - 4l}{l} \tag{3.13}$$

as it is

$$p_2^2 = (p_0^2 + p_a^2)/2 \tag{3.14}$$

### 3.2.2 Steady-state continuity equation

The continuity equation is written for the air volume inside the rectangle:

$$G_{in} - G_{out} = 0 \tag{3.15}$$

Substituting the corresponding terms, pressure $p_0$ can be obtained for each imposed air gap, as presented in [65]:

$$c_1 k_T c_d p_s \sqrt{1 - \left(\frac{\frac{p_0}{(1-0.148\gamma)p_s} - b}{1-b}\right)^2} - c_2 h_0^3 (p_0^2 - p_a^2) = 0 \tag{3.16}$$

### 3.2.3 Dynamic condition

In dynamic conditions, three pressure levels are considered according to Figure 3.2. Pressure $p_1'$ is defined in the center of volume $V_1$, while pressure $p_0'$ is the mean pressure on the supply rectangle perimeter. $p_2'$ is the mean pressure along the perimeter of a rectangle at distance $l/2$ from the edges of the pad. Outside volume $V_1$, volume $V_2$ is defined where the pressure distribution is assumed to be piecewise linear. The dynamic values $p_0'$, $p_1'$ and $p_2'$ are different from the steady-state values due to capacitance and resistance effects. In static conditions, flow $G_1$ is null and pressures $p_0'$ and $p_1'$ coincide with pressure $p_0$, while pressure $p_2'$ converges to the value:

$$p_2'(0) = \sqrt{\frac{p_0^2 + p_a^2}{2}} \tag{3.17}$$

Figure 3.3 depicts the equivalent pneumatic circuit of the air pad in the dynamic condition.

### 3.2.4 Dynamic continuity equations

The continuity equations for volumes $V_1$ and $V_2$ are written in order to obtain a system of equations and calculate the unknown pressure values in the dynamic conditions:

$$\begin{cases} G_1 = \dot{m}_1 \\ G_{in} = G_1 + G_2' \\ G_2' - G_2'' = \dot{m}_2 \end{cases} \tag{3.18}$$

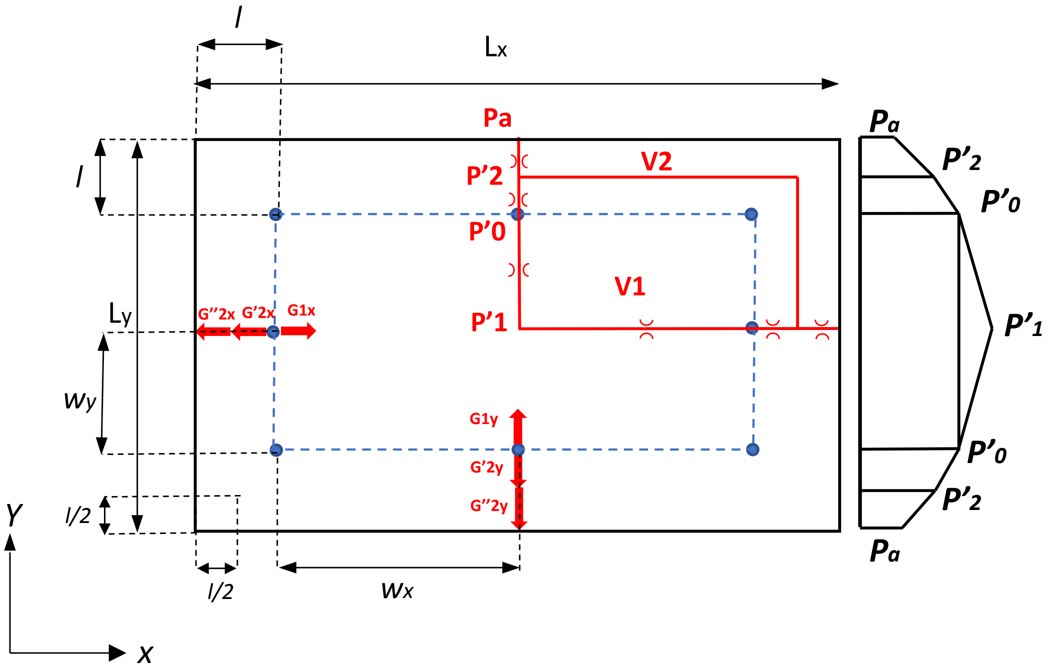

Figure 3.2: Sketch of the air pad with dynamic pressure distribution.

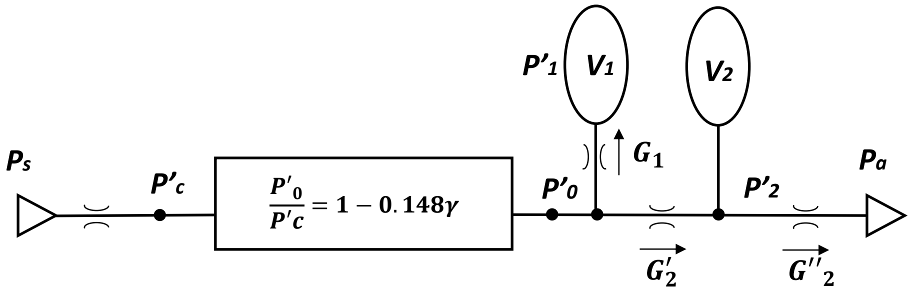

Figure 3.3: Equivalent pneumatic circuit of the air pad in the dynamic condition.

$m_1$ and $m_2$ are the air masses inside volumes $V_1$ and $V_2$ respectively. $G_{in}$ is defined in Equation 3.7 and according to Figure 3.2 the flow rate $G_1$ entering control volume

$V_1$, and exhaust flows $G'_2$ and $G''_2$ are:

$$\begin{aligned} G_1 = 2(G_{1x} + G_{1y}) &= \frac{\Omega h'^3}{6\mu RT}(\frac{L_y - 2l}{L_x - 2l} + \frac{L_x - 2l}{L_y - 2l})({p'_0}^2 - {p'_1}^2) \\ G'_2 = 2(G'_{2x} + G'_{2y}) &= \frac{h'^3}{6\mu RT}(\frac{L_y - 2l}{l} + \frac{L_x - 2l}{l})({p'_0}^2 - {p'_2}^2) \\ G''_2 = 2(G''_{2x} + G''_{2y}) &= \frac{h'^3}{6\mu RT}(\frac{L_y - 2l}{l} + \frac{L_x - 2l}{l})({p'_2}^2 - p_a^2) \end{aligned} \tag{3.19}$$

Using coefficients yields to a simple format:

$$\begin{aligned} G_1 &= c_3 h'^3 ({p'_0}^2 - {p'_1}^2) \\ G'_2 &= 2c_2 h'^3 ({p'_0}^2 - {p'_2}^2) \\ G''_2 &= 2c_2 h'^3 ({p'_2}^2 - p_a^2) \end{aligned} \tag{3.20}$$

where

$$c_3 = \frac{\Omega}{6\mu RT}(\frac{L_y - 2l}{L_x - 2l} + \frac{L_x - 2l}{L_y - 2l}) \tag{3.21}$$

As the air flow inside volume $V_1$ is bidimensional, the unidimensional flow formula (Equation 3.21) needs a correction indicated as $\Omega$. This coefficient is applied to increase the accuracy of LP model particularly for low air gaps (less than 10 $\mu$m). The influence of this correction coefficient on the accuracy of the LP model is discussed afterward, see Figure 6.5 and Figure 6.6.

Other terms of Equation 3.18 are masses $m_1$ and $m_2$ which can be calculated by integrating the air density over volumes $V_1$ and $V_2$. According to Figure 3.4, $V_2$ is partitioned into smaller parts to simplify the integration.

these are simplified into

$$\begin{aligned} m_1 &= c_4 h'(2p'_0 + p'_1) \\ m_2 &= h'(c_5 p'_0 + c_6 p'_2 + c_7 p_a) \end{aligned} \tag{3.22}$$

where

$$\begin{aligned} c_4 &= \frac{(L_x - 2l)(L_y - 2l)}{3RT} \\ c_5 &= \frac{1}{RT}\Big[(L_x + L_y)\frac{l}{2} - \frac{5}{3}l^2\Big] \\ c_6 &= \frac{l}{RT}(L_x + L_y - 2l)l \\ c_7 &= \frac{1}{RT}\Big[(L_x + L_y)\frac{l}{2} - \frac{l^2}{3}\Big] \end{aligned} \tag{3.23}$$

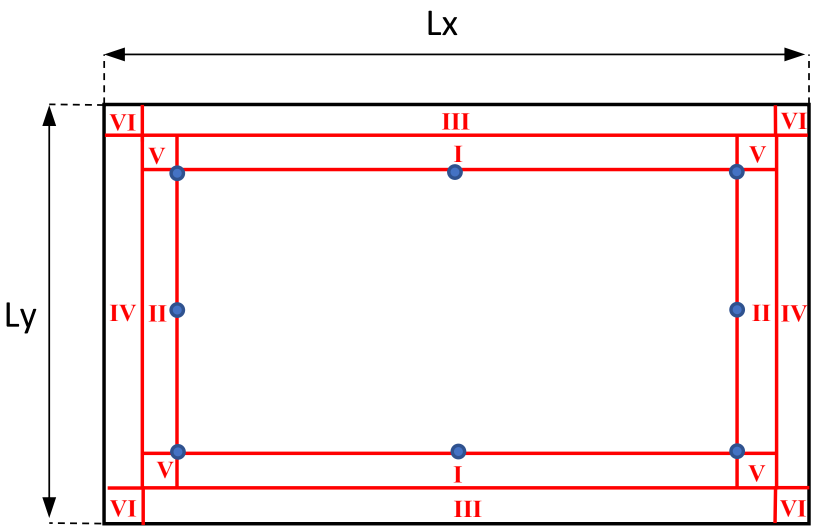

Figure 3.4: Partition of volumes $V_1$ and $V_2$ in subvolumes.

Substituting the mass derivatives and flow rates in Equation 3.18 one obtains:

$$\begin{cases} c_3 h'^3 ({p'_0}^2 - {p'_1}^2) = c_4 \Big( \dot{h}' (2p'_0 + p'_1) + h' (2\dot{p}'_0 + \dot{p}'_1) \Big) \\ c_1 k_T c_d p_s \sqrt{1-\phi^2} - c_3 h'^3 ({p'_0}^2 - {p'_1}^2) - 2c_2 h'^3 ({p'_0}^2 - {p'_2}^2) = 0 \\ 2c_2 h'^3 ({p'_0}^2 - {p'_2}^2) - 2c_2 h'^3 ({p'_2}^2 - p_a^2) = \dot{h}' (c_5 p'_0 + c_6 p'_2 + c_7 p_a) + h' (c_5 \dot{p}'_0 + c_6 \dot{p}'_2) \end{cases} \tag{3.24}$$

The steady solution coincides with the solution of Equation 3.15, as in this case pressures $p'_0$ and $p'_1$ are equal to $p_0$. Finally, the matrix form of Equation 3.24 is

$$h' \begin{bmatrix} 2c_4 & c_4 & 0 \\ 0 & 0 & 0 \\ c_5 & 0 & c_6 \end{bmatrix} \begin{bmatrix} \dot{p}'_0 \\ \dot{p}'_1 \\ \dot{p}'_2 \end{bmatrix} = \begin{bmatrix} c_3 h'^3 & -c_3 h'^3 & 0 \\ -(c_3 + 2c_2) h'^3 & c_3 h'^3 & 2c_2 h'^3 \\ 2c_2 h'^3 & 0 & -4c_2 h'^3 \end{bmatrix} \begin{bmatrix} p_0'^2 \\ p_1'^2 \\ p_2'^2 \end{bmatrix} +$$
$$\dot{h}' \begin{bmatrix} -2c_4 & -c_4 & 0 \\ 0 & 0 & 0 \\ -c_5 & 0 & -c_6 \end{bmatrix} \begin{bmatrix} p'_0 \\ p'_1 \\ p'_2 \end{bmatrix} + \begin{bmatrix} 0 \\ c_1 k_T c_d p_s \sqrt{1-\phi^2} \\ 2c_2 h'^3 p_a^2 - \dot{h}' c_7 p_a \end{bmatrix}$$

### 3.2.5 Linearization

All terms are linearized around their static point by use of first-order Taylor expansion formula. Below the dynamic quantities are defined as the sum of the static value and the perturbation value:

$$\begin{aligned} \bar{p}'_0 &= p_0 + \Delta p_0 \\ \bar{p}'_1 &= p_0 + \Delta p_1 \\ \bar{p}'_2 &= p_0 + \Delta p_2 \\ \bar{h}' &= h_0 + \Delta h \end{aligned} \tag{3.25}$$

Substituting the linearized terms in Equation 3.22, the time derivatives of linearized masses in volumes $V_1$ and $V_2$ can be obtained:

$$\begin{aligned} \dot{\bar{m}}_1 &= 3c_4p_0\Delta\dot{h} + c_4h_0(2\Delta\dot{p}_0 + \Delta\dot{p}_1) \\ \dot{\bar{m}}_2 &= \Big(c_5p_0 + c_6\sqrt{\frac{p_0^2 + p_a^2}{2}} + c_7p_a\Big)\Delta\dot{h} + h_0(c_5\Delta\dot{p}_0 + c_6\Delta\dot{p}_2) \end{aligned} \tag{3.26}$$

Using Taylor expansion, also the linearized flow rates are calculated:

$$\begin{aligned} \bar{G}_1 = G_{1,0} + \Delta G_1 &= G_{1,0} + \frac{\partial G_1}{\partial h'}\Delta h + \frac{\partial G_1}{\partial p'_0}\Delta p'_0 + \frac{\partial G_1}{\partial p'_1}\Delta p_1 \\ \bar{G}'_2 = G'_{2,0} + \Delta G_2 &= G'_{2,0} + \frac{\partial G'_2}{\partial h'}\Delta h + \frac{\partial G'_2}{\partial p'_0}\Delta p_0 + \frac{\partial G'_2}{\partial p'_2}\Delta p_2 \\ \bar{G}''_2 = G''_{2,0} + \Delta G''_2 &= G''_{2,0} + \frac{\partial G''_2}{\partial h'}\Delta h + \frac{\partial G''_2}{\partial p'_2}\Delta p_2 \\ \bar{G}_{in} = G_{in,0} + \Delta G_{in,0} &= G_{in,0} + \frac{\partial G_{in}}{\partial h'}\Delta h + \frac{\partial G_{in}}{\partial p'_0}\Delta p_0 \end{aligned} \tag{3.27}$$

where the dynamic variations of these flow rates are:

$$\begin{aligned} \Delta G_1 &= 2c_3h_0^3p_0(\Delta p_0 - \Delta p_1) \\ \Delta G'_2 &= 6c_2h_0^2(p_0^2 - \frac{p_0^2 + p_a^2}{2})\Delta h + 4c_2h_0^3\left(p_0\Delta p_0 - \sqrt{\frac{p_0^2 + p_a^2}{2}}\Delta p_2\right) \\ \Delta G''_2 &= 6c_2h_0^2\Big(\frac{p_0^2 + p_a^2}{2} - p_a^2\Big)\Delta h + 4c_2h_0^3\sqrt{\frac{p_0^2 + p_a^2}{2}}\Delta p_2 \\ \Delta G_{in} &= c_8\Delta p_0 + c_9\Delta h \end{aligned} \tag{3.28}$$

and

$$\begin{aligned} c_8 &= -\frac{c_1k_Tc_d}{(1 - 0.148\gamma)^2(1 - b)^2}\frac{p_0 - b(1 - 0.148\gamma)p_s}{p_s}\sqrt{1 - \left(\frac{\dfrac{p_0}{(1 - 0.148\gamma)p_s} - b}{1 - b}\right)^2} \\ c_9 &= 0.85c_1p_s\sqrt{1 - \left(\frac{\dfrac{p_0}{(1 - 0.148\gamma)p_s} - b}{1 - b}\right)^2}\frac{8.2}{d_s}e^{-8.2\frac{h_0}{d_s}} \end{aligned} \tag{3.29}$$

The effect of Reynolds number in linearizing the inlet flow through supply holes $G_{in}$ is neglected, as it produces complexity in the equation and does not affect much the accuracy of the model. Substituting all these linearized terms in Equation 3.18 yields:

$$\begin{gathered} G_{1,0} + \Delta G_1 = \dot{\bar{m}}_1 \\ G_{in0} + \Delta G_{in} - G_{1,0} - \Delta G_1 - G'_{2,0} - \Delta G'_2 = 0 \\ G'_{2,0} + \Delta G'_2 - G''_{2,0} - \Delta G''_2 = \dot{\bar{m}}_2 \end{gathered} \tag{3.30}$$

After elimination of the static terms, the final linearized continuity equations are:

$$\begin{cases} 2c_3h_0^3p_0(\Delta p_0 - \Delta p_1) = 3c_4p_0\dot{\Delta h} + c_4h_0(2\dot{\Delta p}_0 + \dot{\Delta p}_1) \\ c_8\Delta p_0 + c_9\Delta h - 2c_3h_0^3p_0(\Delta p_0 - \Delta p_1) - 6c_2h_0^2(p_0^2 - \dfrac{p_0^2+p_a^2}{2})\Delta h + \\ - 4c_2h_0^3\left(p_0\Delta p_0 - \sqrt{\dfrac{p_0^2+p_a^2}{2}}\Delta p_2\right) = 0 \\ 6c_2h_0^2(p_0^2 - \dfrac{p_0^2+p_a^2}{2})\Delta h + 4c_2h_0^3\left(p_0\Delta p_0 - \sqrt{\dfrac{p_0^2+p_a^2}{2}}\Delta p_2\right) - 6c_2h_0^2\Big(\dfrac{p_0^2+p_a^2}{2} - p_a^2\Big)\Delta h + \\ - 4c_2h_0^3\sqrt{\dfrac{p_0^2+p_a^2}{2}}\Delta p_2 = \Big(c_5p_0 + c_6\sqrt{\dfrac{p_0^2+p_a^2}{2}} + c_7p_a\Big)\dot{\Delta h} + h_0(c_5\dot{\Delta p}_0 + c_6\dot{\Delta p}_2) \end{cases} \tag{3.31}$$

The load carrying capacity of the pad is here below derived:

$$\begin{aligned} F &= \int p\; dA \\ F &= (L_x - 2l)(L_y - 2l)\left[p'_0 + \frac{(p'_1 - p'_0)}{3}\right] + l(L_x + L_y - 4l)\frac{p'_0 + p'_2}{2} + \\ &\quad + l(L_x + L_y - 2l)\left(p_a + \frac{p'_2 - p_a}{2}\right) + l^2\Big[\frac{p'_0 + 2p'_2}{3}\Big] + l^2\Big[\frac{p'_2 + 2p_a}{3}\Big] - p_aL_xL_y \\ F &= p'_0\left[\frac{2}{3}L_xL_y - \frac{5}{6}l(L_x + L_y) + l^2\right] + p'_1\left[\frac{1}{3}(L_x - 2l)(L_y - 2l)\right] + \\ &\quad + p'_2\Big[(L_x + L_y)l - 2l^2\Big] + p_a\left[\frac{1}{2}(L_x + L_y)l - \frac{1}{3}l^2 - L_xL_y\right] \end{aligned} \tag{3.32}$$

The perturbation value of the carrying capacity is:

$$\Delta F = \Delta p_0\left[\frac{2}{3}L_xL_y - \frac{5}{6}l(L_x + L_y) + l^2\right] + \Delta p_1\left[\frac{1}{3}(L_x - 2l)(L_y - 2l)\right] + \Delta p_2\Big[l(L_x + L_y) - 2l^2\Big] \tag{3.33}$$

Writing the equation with Laplace transform and again simplifying it by use of some coefficients results in

$$\Delta F(s) = c_{10}\Delta p_0(s) + c_4 RT\Delta p_1(s) + c_6 RT\Delta p_2(s) \tag{3.34}$$

where

$$c_{10} = \frac{2}{3}L_x L_y - \frac{5}{6}l(L_x + L_y) + l^2 \tag{3.35}$$

Finally, the transfer function between the air gap under the pad and the load capacity is:

$$-\frac{\Delta F(s)}{\Delta h(s)} = k(s) + c(s)s = RT\frac{n_0 + n_1 s + n_2 s^2}{d_0 + d_1 s + d_2 s^2} \tag{3.36}$$

where

$$\begin{aligned}
n_0 =& -16c_2c_3h_0^5RTp_0\Big(\sqrt{2}\,(c_{10}+c_4)\,\sqrt{p_a^2+p_0^2}+c_6p_0\Big)\Big(3c_2h_0^2\left(p_a^2-p_0^2\right)+c_9\Big)\\
n_1 =& 2h_0^2RT\Bigg[8c_2c_3c_7c_{12}h_0^3p_ap_0^2+6c_2c_3c_5c_6h_0^3p_a^2p_0+4\sqrt{2}c_2c_3c_5c_{10}h_0^3p_0^2\sqrt{p_a^2+p_0^2}+4\sqrt{2}\\
&c_2c_3c_5c_4h_0^3p_0^2\sqrt{p_a^2+p_0^2}+4\sqrt{2}c_2c_3c_7c_{10}h_0^3p_ap_0\sqrt{p_a^2+p_0^2}+4\sqrt{2}c_2c_3c_7c_4h_0^3p_ap_0\sqrt{p_a^2+p_0^2}-\\
&c_3c_6p_0\Bigg(2c_2h_0^3\Big(-2\sqrt{2}c_6p_0\sqrt{p_a^2+p_0^2}+c_{10}(p_a^2-5p_0^2)+c_4(p_a^2-5p_0^2)+\sqrt{2}c_8c_6\sqrt{p_a^2+p_0^2}+\\
&2c_9(c_{10}+c_4)h_0\Big)+4c_2c_4\Bigg[3c_2h_0^3\Bigg(c_6(p_0^3-p_a^2p_0)+\sqrt{2}\sqrt{p_a^2+p_0^2}\Big(c_{10}(p_0^2-p_a^2)+2c_4p_a^2\Big)\Bigg)+\\
&3p_0\Bigg(2c_3h_0^3p_0\Big(\sqrt{2}(c_{10}+c_4)\sqrt{p_a^2+p_0^2}+c_6p_0\Big)-\sqrt{2}c_8c_4\sqrt{p_a^2+p_0^2}\Bigg)-\\
&c_9h_0\Big(\sqrt{2}(c_{10}-2c_4)\sqrt{p_a^2+p_0^2}+c_6p_0\Big)\Bigg]-2c_3c_7c_8c_6p_ap_0+2c_2c_3c_5c_6h_0^3p_0^3+\\
&2c_3c_5c_9c_6h_0p_0-2c_3c_5c_8c_6p_0^2\Bigg]
\end{aligned} \tag{3.37}$$

In the case of perturbating the air gap with a sinusoidal function at frequency $f$,

$$h' = h_0 + \Delta h sin(2\pi f t) \tag{3.38}$$

the frequency response can be calculated and the stiffness and damping coefficients can be obtained as the imaginary and real parts of the formed transfer function of Equation 3.36.

## 3.3 Conclusion

Development of a lumped parameters model for aerostatic pads with multiple supply holes in both static and dynamic conditions is the main concern of this chapter. The results obtained by the LP model for simulation of a sample air pad can be then used to be compared with those obtained by the distributed parameters (DP) model , and also with experimental results. Also the influence of the correction factor $\Omega$ on the accuracy of the model can be investigated. It has been verified that the LP model with the correction factor $\Omega$ is adequately accurate and precise with less effort in terms of time and complexity. The model is geometry dependent and it can be used for sensitivity analysis to investigate the effect of geometrical parameters on the pad performances and achieving the best design. An interesting feature of the LP model is that the transfer function between the air gap and the load capacity is expressed in closed form as a function of the geometrical parameters.

# Chapter 4

# Distributed parameters (DP) model

## 4.1 Introduction

Reynolds equation can be obtained with different methods such as physical and mathematical derivation. In derivation of Reynolds equation there are some assumptions to be considered. The discretization is achieved by substituting the derivatives of expressions obtained based on first-order Taylor expansion series. Finite difference method has been widely utilized to solve the Reynolds equation numerically, because of its simplicity. The solution of Reynolds equation base on discretization and finite difference method is base of the so called Distributed Parameter (DP) model which later on is used for validation of the developed LP model.

## 4.2 Reynolds Equation

Reynolds presented a second order differential equation, obtained from Navier-Stokes equations in association with the continuity equations, to obtain the pressure distribution inside narrow gaps. This pressure provides the possibility to completely separate the interacting surfaces and achieving low friction motions. This lubrication regimes was called Hydrodynamic Lubrication regime (HL) and it is generally characterised by conformal surfaces and pressures which are not large enough to induce their elastic deformations.

## 4.3 Assumptions

The Reynolds equation assumes that:

- The continuum description is valid.
- The film is thin (the length is much greater than thickness).
- Body forces can be neglected: there are no outside fields of force acting on the lubricant, e.g. gravitational or magnetic forces. This assumption can be reasonably considered valid for all non-conducting fluids.
- The effect of inertia can be neglected. For a Reynolds number of 1000, the pressures are only modified by about 5 %.
- lubricant flow is laminar (low Reynolds numbers).
- fluid is considered to be Newtonian.
- Viscosity is considered constant across the fluid film thickness.
- Pressure variation along the $z$ direction can be neglected. The pressure can not vary significantly across the film thickness because it is very thin $P = P(x, y)$.
- Sliding surfaces of the bearing can be approximated flat, because their curvatures are very large compared to the fluid film thickness.
- There is no slip at boundaries, which means that the velocity of the surfaces is the same as the the adjacent fluid film layer velocity.
- Velocity gradients ( $\frac{\partial u}{\partial y}, \frac{\partial w}{\partial x}, \frac{\partial w}{\partial y}, \frac{\partial v}{\partial x} << 1$) along the $x$ and $y$ directions are small (the velocity variations are smooth compared to those along the $z$ direction). For this reason the related shear stresses:
  $\tau_{xy} = \tau_{yx} = \mu\Big(\cancel{\frac{\partial v}{\partial x}} + \cancel{\frac{\partial u}{\partial y}}\Big)$,
  $\tau_{xz} = \tau_{zx} = \mu\Big(\frac{\partial u}{\partial z} + \cancel{\frac{\partial w}{\partial x}}\Big)$
  $\tau_{yz} = \tau_{zy} = \mu\Big(\frac{\partial v}{\partial z} + \cancel{\frac{\partial w}{\partial y}}\Big)$.

## 4.4 Derivation of Reynolds Equation

In this section the Reynolds equation is derived in Cartesian coordinates directly by two different ways from the equilibrium, constitutive and continuity equations and directly obtained from the mass conservation principle.

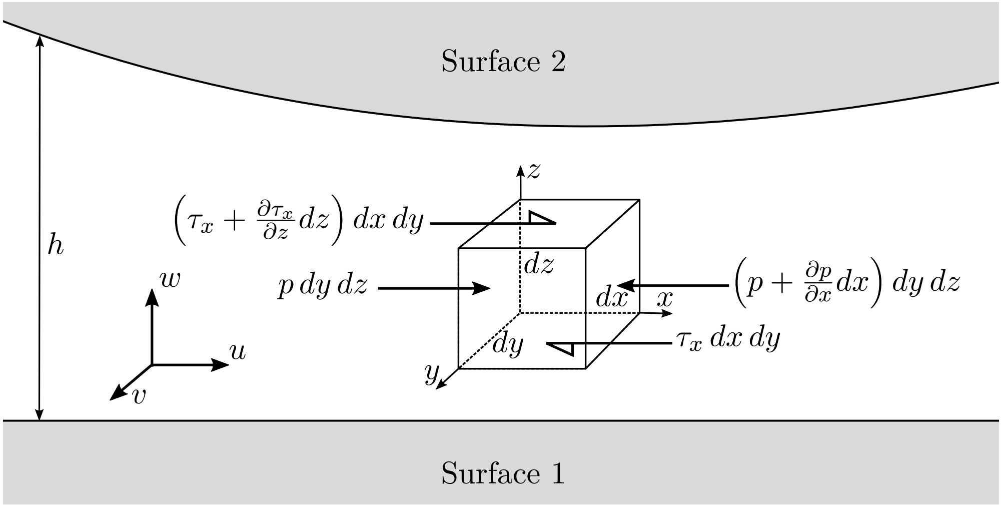

Figure 4.1: Forces equilibrium of a thin film fluid element.

Equilibrium of forces in $x$ and $y$ directions of a thin film fluid element between two surfaces (see Figure 4.1) under the assumptions stated above could be written as

$$\begin{cases} (x): \quad pdydz - \left(p + \dfrac{\partial p}{\partial x}dx\right)dydz - \tau_{zx}dxdy + \left(\tau_{zx} + \dfrac{\partial \tau_{zx}}{\partial z}dx\right)dxdy = 0 \\ \\ (y): \quad pdxdz - \left(p + \dfrac{\partial p}{\partial y}dy\right)dxdz - \tau_{zy}dxdy + \left(\tau_{zy} + \dfrac{\partial \tau_{zy}}{\partial z}dz\right)dxdy = 0 \end{cases} \tag{4.1}$$

$$\begin{cases} (x): \quad \dfrac{\partial p}{\partial x} = \dfrac{\partial \tau_{zx}}{\partial z} \\ \\ (y): \quad \dfrac{\partial p}{\partial y} = \dfrac{\partial \tau_{zy}}{\partial z} \end{cases} \tag{4.2}$$

The relation between the velocity component of the fluid can be achieved by considering the constitutive equations of Newtonian fluids:

$$\tau_{i,j} = \mu\left(\frac{\partial u_i}{\partial x_j} + \frac{\partial u_j}{\partial x_i}\right) \quad i, j = x, y, z \tag{4.3}$$

where $u$ and $x$ are the velocity components of the fluid ($u_x = u$, $u_y = v$ and $u_z = w$) and the Cartesian reference coordinates ($x_x = x$, $x_y = y$ and $x_z = z$) respectively. By considering Equation 4.2 and Equation 4.3 and the assumptions discussed in section 4.3, it is possible to obtain:

$$\begin{cases} (x): \quad \dfrac{\partial p}{\partial x} = \dfrac{\partial}{\partial z}\left(\mu \dfrac{\partial u}{\partial z}\right) \\ \\ (y): \quad \dfrac{\partial p}{\partial y} = \dfrac{\partial}{\partial z}\left(\mu \dfrac{\partial v}{\partial z}\right) \end{cases} \tag{4.4}$$

The fluid film velocity profiles along $x$ and $y$ directions can be achieved by integrating Equation 4.4 along $z$.

$$\begin{cases} (x): \quad \dfrac{\partial p}{\partial x} z = \mu \dfrac{\partial u}{\partial z} + X_1 \\ \\ (y): \quad \dfrac{\partial p}{\partial y} z = \mu \dfrac{\partial v}{\partial z} + Y_1 \end{cases} \tag{4.5}$$

Integrating once more along $z$

$$\begin{cases} (x): \quad u(z) = \dfrac{\partial p}{\partial x} \dfrac{z^2}{2\mu} - X_1 \dfrac{z}{\mu} - X_2 \\ \\ (y): \quad v(z) = \dfrac{\partial p}{\partial y} \dfrac{z^2}{2\mu} - Y_1 \dfrac{z}{\mu} - Y_2 \end{cases} \tag{4.6}$$

where $X$ and $Y$ are constants which can be computed by applying the surface velocity component $u$ and $v$ as boundary conditions, by assumption of no slip between the surface and the fluid.

$$\begin{cases} u(0) = u_a \\ u(h) = u_b \\ v(0) = v_a \\ v(h) = v_b \end{cases} \tag{4.7}$$

from which it can be obtained as:

$$\begin{cases} X_2 = -u_a \\ X_1 = \dfrac{\mu}{h}(u_a - u_b) + \dfrac{h}{2}\dfrac{\partial p}{\partial x} \\ Y_2 = -v_a \\ Y_1 = \dfrac{\mu}{h}(v_a - v_b) + \dfrac{h}{2}\dfrac{\partial p}{\partial x} \end{cases} \tag{4.8}$$

$$\begin{cases} (x): \quad u(z) = \dfrac{\partial p}{\partial x}\dfrac{z^2}{2\mu} - \dfrac{z}{\mu}\left[\dfrac{\mu}{h}(u_a - u_b) + \dfrac{h}{2}\dfrac{\partial p}{\partial x}\right] + u_a \\ \\ (y): \quad v(z) = \dfrac{\partial p}{\partial y}\dfrac{z^2}{2\mu} - \dfrac{z}{\mu}\left[\dfrac{\mu}{h}(v_a - v_b) + \dfrac{h}{2}\dfrac{\partial p}{\partial y}\right] + v_a \end{cases} \tag{4.9}$$

The flow rate along the $x$ and $y$ directions can be computed by integrating Equation 4.9 through the gap height $h$.

$$\begin{cases} (x): \quad q_x = \int_0^h u(z)dz = -\dfrac{h^3}{12\mu}\dfrac{\partial p}{\partial x} + (u_a + u_b)\dfrac{h}{2} \\ \\ (y): \quad q_y = \int_0^h v(z)dz = -\dfrac{h^3}{12\mu}\dfrac{\partial p}{\partial y} + (v_a + v_b)\dfrac{h}{2} \end{cases} \tag{4.10}$$

### 4.4.1 Physical Derivation

The Reynolds equation can be derived directly by considering the rate of mass flow through a rectangular cross section control of $dx$ and $dy$ sides illustrated in Figure 4.2 and Figure 4.3. In this case, one of the surfaces is the plane $z = 0$, whereas the other one is a curved moving surfaces so that the film thickness at any instant is a function of $x$ and $y$ only. It is worth noting the implications of the last statement:

$$h = h(x(t), y(t), t) \tag{4.11}$$

Consequently, in non stationary conditions, air gap variations generate several effects inside the fluid film pressure:

$$\begin{aligned} \frac{Dh}{Dt} =& \frac{\partial h}{\partial x}\cdot\frac{\partial x}{\partial t} + \frac{\partial h}{\partial y}\cdot\frac{\partial y}{\partial t} + \frac{\partial h}{\partial t} = \\ & \frac{\partial h}{\partial x}\cdot(u_b - u_a) + \frac{\partial h}{\partial y}\cdot(v_b - v_a) + (w_b - w_a) \end{aligned} \tag{4.12}$$

The principle of mass conservation demands that the rate at which mass is accumulating in the control volume must be equal to the difference between the rates at which mass enters and leaves. The mass of lubricant in the control volume at any instant is $\rho h dx dy$. The rate of change within the control volume arises from the change in the difference between the rate of mass flowing into the control volume and the rate leaving the control volume.

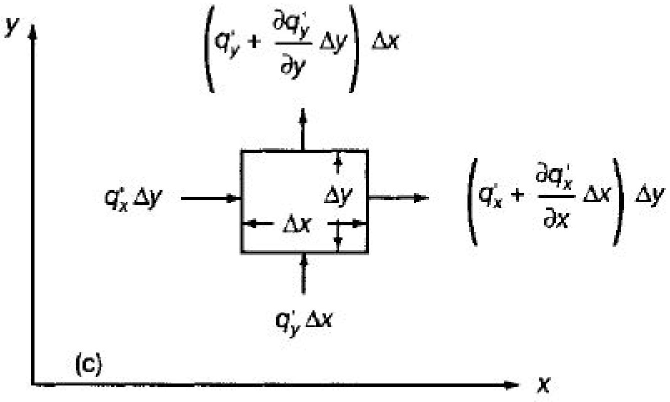

Figure 4.2: Continuity of flow in an element

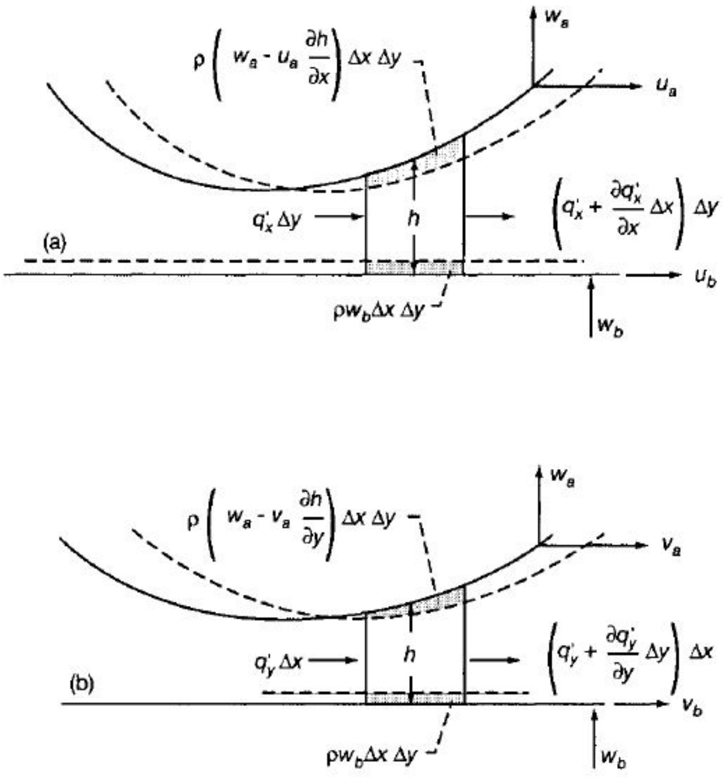

Figure 4.3: Mass flow through rectangular cross section control volume

As it is shown in Figure 4.3 the mass conservation principle can be written as following:

$$\begin{gathered}\rho q_x dy - \left(q_x + \frac{\partial(\rho q_x)}{\partial x}dxdy\right) + \rho q_y dx - \left(\rho q_y + \frac{\partial(\rho q_y)}{\partial y}dydx\right)\right] = \\ \frac{\partial(\rho h)}{\partial t}dxdy - \frac{\partial(\rho q_x)}{\partial x} - \frac{\partial(\rho q_y)}{\partial y} = \frac{\partial(\rho h)}{\partial t}\end{gathered} \tag{4.13}$$

Substituting Equation 4.10 into Equation 4.13 gives:

$$-\frac{\partial}{\partial x}\left(-\frac{\rho h^3}{12\mu}\frac{\partial p}{\partial x} + (u_a+u_b)\frac{\rho h}{2}\right) - \frac{\partial}{\partial y}\left(-\frac{\rho h^3}{12\mu}\frac{\partial p}{\partial y} + (v_a+v_b)\frac{\rho h}{2}\right) = \frac{\partial(\rho h)}{\partial t} \tag{4.14}$$

Rearranging and rewriting the previous equation

$$\frac{\partial}{\partial x}\left(\frac{\rho h^3}{12\mu}\frac{\partial p}{\partial x}\right) + \frac{\partial}{\partial y}\left(\frac{\rho h^3}{12\mu}\frac{\partial p}{\partial y}\right) = \frac{\partial}{\partial x}\left[(u_a+u_b)\frac{\rho h}{2}\right] + \frac{\partial}{\partial y}\left[(v_a+v_b)\frac{\rho h}{2}\right] + \underbrace{\frac{\partial(\rho h)}{\partial t}}_{I} \tag{4.15}$$

The term $I$ can be developed as follows:

$$\begin{gathered}\frac{\partial(\rho h)}{\partial t} = \rho\left(\frac{\partial h}{\partial x}\frac{\partial x}{\partial t} + \frac{\partial h}{\partial y}\frac{\partial y}{\partial t} + \frac{\partial h}{\partial t}\right) + h\frac{\partial \rho}{\partial t} = \\ \rho\left[\frac{\partial h}{\partial x}(u_b-u_a) + \frac{\partial h}{\partial y}(v_b-v_a) + (w_b-w_a)\right] + h\frac{\partial \rho}{\partial t}\end{gathered} \tag{4.16}$$

Therefore, Equation 4.15 becomes:

$$\begin{gathered}\underbrace{\frac{\partial}{\partial x}\left(\frac{\rho h^3}{12\mu}\frac{\partial p}{\partial x}\right) + \frac{\partial}{\partial y}\left(\frac{\rho h^3}{12\mu}\frac{\partial p}{\partial y}\right)}_{Poiseulle} = \underbrace{\frac{\partial}{\partial x}\left[\frac{\rho h}{2}(u_a+u_b)\right] + \frac{\partial}{\partial y}\left[\frac{\rho h}{2}(v_a+v_b)\right]}_{Couette} + \\ + \underbrace{\rho(w_b-w_a) - \rho u_b\frac{\partial h}{\partial x} - \rho v_b\frac{\partial h}{\partial y}}_{Squeeze} + \underbrace{h\frac{\partial \rho}{\partial t}}_{Local Expansion}\end{gathered} \tag{4.17}$$

This equation is known as the Reynolds equation.

### 4.4.2 Mathematical derivation

The Reynolds equation can be finally achieved by substituting Equation 4.10 in the principle of flow mass conservation:

$$\int_V \frac{\partial \rho}{\partial t} + \bar{\nabla}(\rho \cdot \bar{u}) dV = 0 \tag{4.18}$$

$$\int_0^h \left[ \frac{\partial \rho}{\partial t} + \frac{\partial(\rho u)}{\partial x} + \frac{\partial(\rho v)}{\partial y} + \frac{\partial(\rho w)}{\partial z} \right] dz = 0 \tag{4.19}$$

$$\int_0^h \frac{\partial \rho}{\partial t} dz = h \frac{\partial \rho}{\partial t} \tag{4.20}$$

$$\begin{aligned} \int_0^h \frac{\partial(\rho u)}{\partial x} dz = -(\rho u)_{z=h} + \frac{\partial}{\partial x} \left\{ \rho \left[ -\frac{h^3}{12} \frac{\partial p}{\partial x} + (u_a + u_b) \frac{h}{2} \right] \right\} = \\ -\rho u_b \frac{\partial h}{\partial x} + \frac{\partial}{\partial x} \left[ -\frac{\rho h^3}{12\mu} \frac{\partial p}{\partial x} \right] + \frac{\partial}{\partial x} \left[ \frac{\rho h}{2} (u_a + u_b) \right] \end{aligned} \tag{4.21}$$

$$\begin{aligned} \int_0^h \frac{\partial(\rho v)}{\partial y} dz = -(\rho v)_{z=h} + \frac{\partial}{\partial y} \left\{ \rho \left[ -\frac{h^3}{12} \frac{\partial p}{\partial y} + (v_a + v_b) \frac{h}{2} \right] \right\} = \\ -\rho v_b \frac{\partial h}{\partial y} + \frac{\partial}{\partial y} \left[ -\frac{\rho h^3}{12\mu} \frac{\partial p}{\partial y} \right] + \frac{\partial}{\partial y} \left[ \frac{\rho h}{2} (v_a + v_b) \right] \end{aligned} \tag{4.22}$$

$$\int_0^h \frac{\partial(\rho w)}{\partial z} dz = \rho(w_b - w_a) \tag{4.23}$$

It is worth noting that:

- in this case the density $\rho$ is considered constant along the z direction ($\rho = \rho(x, y)$) as a consequence of the initial assumptions in section 4.3.
- the integration and differentiation of the terms $\rho u$ and $\rho v$ can not be arbitrarily exchanged since h is a function of the Cartesian coordinates x and y: h=h(x,y).

The general formulation of the Reynolds equation is obtained by using these equations:

$$\underbrace{\frac{\partial}{\partial x}\left(\frac{\rho h^3}{12\mu}\frac{\partial p}{\partial x}\right)+\frac{\partial}{\partial y}\left(\frac{\rho h^3}{12\mu}\frac{\partial p}{\partial y}\right)}_{Poiseulle}=$$

$$=\underbrace{\frac{\partial}{\partial x}\left[\frac{\rho h}{2}(u_a+u_b)\right]+\frac{\partial}{\partial y}\left[\frac{\rho h}{2}(v_a+v_b)\right]}_{Couette}+\quad\underbrace{\rho(w_b-w_a)-\rho u_b\frac{\partial h}{\partial x}-\rho v_b\frac{\partial h}{\partial y}}_{Squeeze}+\quad\underbrace{h\frac{\partial \rho}{\partial t}}_{LocalExpansion} \tag{4.24}$$

## 4.5 Discretization

The expression of the Reynolds equation in Equation 4.17 is employed to calculate the pressure distribution of thin viscous fluid films for the thrust bearings.

In these instance the following hypothesis are taken into account in order to achieve the expression of the Reynolds equation:

- ambient pressure at the edges of the pad
- input flow through the supply holes

The generalized Reynolds equation is simplified based on the above assumption as follows:

$$\frac{\partial}{\partial x}\left(\frac{\rho h^3}{12\mu}\cdot\frac{\partial p}{\partial x}\right)+\frac{\partial}{\partial y}\left(\frac{\rho h^3}{12\mu}\cdot\frac{\partial p}{\partial y}\right)+\rho w_a=h\frac{\partial \rho}{\partial t} \tag{4.25}$$

where $\rho w_a$ is the flow rate per unit which enters in the air gap through supply holes and it is assumed that $\rho = p/RT$.

Rectangular pad in Figure 4.5 with sides $L_x$ and $L_y$ is considered. Multiple supply holes are positioned on the sides of a supply rectangle at distance $l$ from the edges of the pad. This distance is the same along $x$ and $y$ directions. The holes are equispaced at a distance $W$, which is also assumed to be equal along the two directions. The hole diameter is $d_s$.

From computational point of view, it is always suitable to use non-dimensional variables.

The air pad surface shown in Figure 4.4 is meshed by employing a grid with $n$ nodes along the $x$ direction and $m$ nodes along the $y$ direction. Therefore, the mesh is a grid consisting in quadratic elements whose dimensions are:

$$\Delta x=\frac{L_x}{n-1} \tag{4.26}$$

$$\Delta y=\frac{L_y}{m-1} \tag{4.27}$$

The model considers a constant pressure $p_0$ inside the supply rectangle of sides $L_x - 2l$ and $L_y - 2l$. This pressure is related to the pressure at the supply hole downstream $p_c$ through the following relation according to Equation 3.1.

The mass flow rate entering in the air gap by nozzles is computed with the aid of an empirical formula described in Equation 3.7

where $Re$ is the Reynolds number related to the supply hole cross section:

$$Re=\frac{4G}{\pi\mu d_s} \tag{4.28}$$

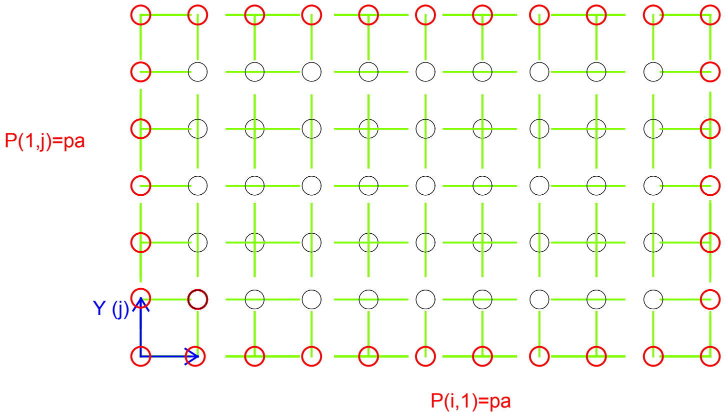

Figure 4.4: A meshed surface of a rectangular pad

The expression shown in inlet mass flow rate can assume different forms based on the condition in which the nozzles operates. It is possible to have sonic or subsonic flows which flow under the following operating conditions:

1. Isoentropic conditions/transformations
2. Isothermal conditions/transformations
3. Polythropic conditions/transformations

The exhaust flow from the air gap (see Figure 4.5) is the sum of the flow calculated for rectangular channels along directions $x$ and $y$:

$$G_{out} = 2(G_x + G_y) \tag{4.29}$$

$$G_x = \frac{h^3}{24\mu RT}(p_0^2 - p_a^2)\frac{L_y - 2l}{l} \tag{4.30}$$

$$G_y = \frac{h^3}{24\mu RT}(p_0^2 - p_a^2)\frac{L_x - 2l}{l} \tag{4.31}$$

$$G_{out} = \frac{h^3}{12\mu RT}(p_0^2 - p_a^2)\left(\frac{Ly - 2l}{l} + \frac{Lx - 2l}{l}\right) \tag{4.32}$$

By introducing the dimensionless parameters $\alpha$ and $\beta$:

$$G_{out} = \frac{h^3}{12\mu RT}(p_0^2 - p_a^2)\left(\frac{\beta}{\alpha} + \frac{1}{\alpha} - 4\right) \tag{4.33}$$

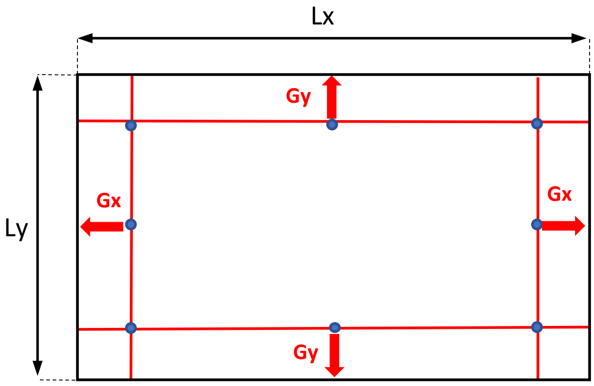

Figure 4.5: The mass conservation principle applied to a rectangular pad

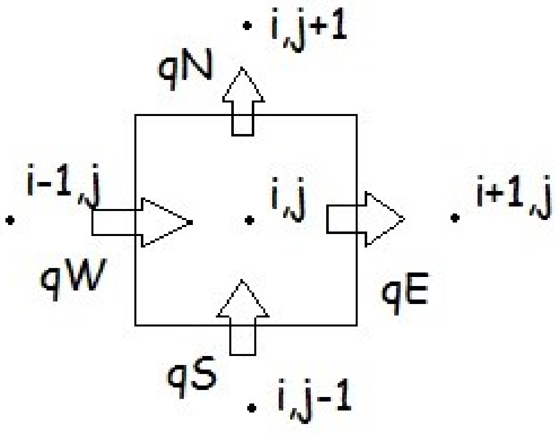

Figure 4.6: The mass conservation applied at the node $(i, j)$

### 4.5.1 Finite difference method

Discretization by finite difference method is achieved by substituting the derivatives in an equation that needs to be solved with appropriate expressions obtained based on Taylor series expansion, commonly limited to the first order. Finite difference method has been widely utilized to solve the Reynolds equation numerically, because of its simplicity. The following derivatives is used to discretize the Reynolds equation:

$$\begin{aligned}\frac{\partial^2 p^2}{\partial x^2} &= \frac{p^2(i+1,j) - 2p^2(i,j) + p^2(i-1,j) + p^2(i-1,j)}{\Delta x^2} \\ \frac{\partial^2 p^2}{\partial y^2} &= \frac{p^2(i,j+1) - 2p^2(i,j) + p^2(i-1,j) + p^2(i,j-1)}{\Delta y^2}\end{aligned} \tag{4.34}$$

Substituting Equation 4.34 in Equation 4.25, the Reynolds equation could be solved for each point to find the air pressure using the discretized equations. The pressure of the node $(i, j)$ in Figure 4.6 is given in Equation 4.35 according to the quantities at the previous time step in the surrounding nodes. Starting from the initial condition of ambient pressure in all nodes, by successive iterations the condition of the regime can be reached. If initial values are selected properly the number of iterations is decreased drastically and solution can be more stable.

$$\begin{aligned}p_{i,j}^{t+1} = p_{i,j}^{t} + \frac{\Delta t}{24\mu h_0}\Bigg[&\frac{h_0^3}{\Delta x^2}\left(p_{i+1,j}^2 - p_{i,j}^2\right) - \frac{h_0^3}{\Delta x^2}\left(p_{i,j}^2 - p_{i-1,j}^2\right) + \\ &\frac{h_0^3}{\Delta y^2}\left(p_{i,j+1}^2 - p_{i,j}^2\right) - \frac{h_0^3}{\Delta y^2}\left(p_{i,j}^2 - p_{i,j-1}^2\right) + \frac{24\mu RTG_{i,j}}{\Delta x \Delta y}\Bigg]\end{aligned} \tag{4.35}$$

The bearing load capacity is computed by integrating the air gap pressure distribution on the pad surface. Iterations continue until a defined threshold of the error regarding the convergence of the bearing load capacity, expressed as a percentage, is attained.

## 4.6 Conclusion

A solution for Reynolds equation based on finite difference method can be a proper alternative for developing a distributed parameter model to later on be used for simulation of the same rectangular pad analyzed by developed lumped parameter model to validate the LP model.

# Chapter 5

# Experimental validation

## 5.1 Introduction

This section is dedicated to the description of the experimental process. Two test benches have been used in order to perform the experimental tests. The first test rig has been used in order to obtain the static characterization of the proposed aerostatic bearing, while the second one has been used including a shaker to impose the dynamic condition to the pad. Both results obtained in the static and dynamic experimental tests are used to verify the proposed lumped model in the next chapters.

## 5.2 The static test

A test bench was used which made it possible to measure the static load capacity, pressure distribution and air consumption of flat aerostatic pad B with supply hole diameter of 0.3 mm which is presented in Figure 5.1.

The test bench used in static measurements is shown in Figure 5.2. The test bench consists of a base which are directly connected to three columns and a cross member. The air gap is established between the pad under test and the stationary bearing member. The vertical movement of the pad determines the air gap which is measured by micrometric transducers. A screw that is under the control of a hand wheel produces the movement of the air bearing. A push-rod for applying the force coming by means of the hand wheel is placed upon the pad by use of a ball in the center of the pad. A load cell is used to measure the applied force on the pad. Two screws adjusted the pad angle.

The stationary bearing member makes it possible to determine pressure distribution along the air gap below the pad under test. The stationary member face is provided with two 0.2 mm diameter holes connected to the associated stationary member outlet ports, which are connected to pressure transducers. The stationary

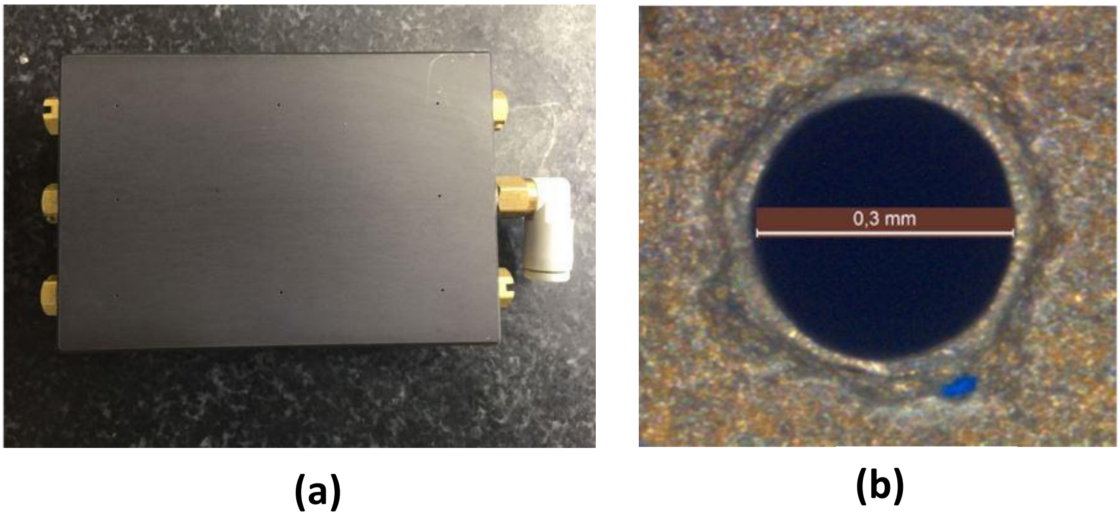

Figure 5.1: (a) Pad B used in experimental tests (b) measured inherent hole diameter.

member can be moved radially with respect to the pad under test by means of a guide (15) secured to platform (16). In order to perform measurements in different radial directions, the platform can be rotated around the pad axis.

## 5.3 The dynamic test

To verify the developed LP model, a 50 × 75 mm rectangular pad with 8 supply holes of diameter 0.3 mm was tested experimentally. Figure 5.3 illustrates the test bench able to investigate dynamic stiffness and damping of the air pad. On the air pad 1, laid on a metal basement 2, a static vertical preload was applied, by means of a pneumatic chamber, in order to establish a given static air gap.

A sinusoidal force was superimposed to the static one exerted by means of a pre-forcing element 3 through the serial connection of an electro-dynamic shaker 4, a stinger 5 and a loading tip 6. The force transmitted to the pad was measured by a load cell 7 (38 kHz bandpass) placed between the cylinder rod and the loading tip. Four capacitive displacement sensors 8 (10 kHz bandpass) detected the pad vertical displacement and measured the air gap height. An eventual tilting of the pad can be detected by the sensors. When the air is supplied, the pad lifts and locates parallel to the basement (in case its geometry is symmetrical respect to the central pin). The air gap under the pad is assumed to be equal to the pad displacement when the air is supplied. This procedure supposes that the pad deformations can be neglected. Sinusoidal excitation F($\omega$) was applied as the input to the pad. Signals were acquired at 10 kHz. Tests were repeated at different frequencies, in the range

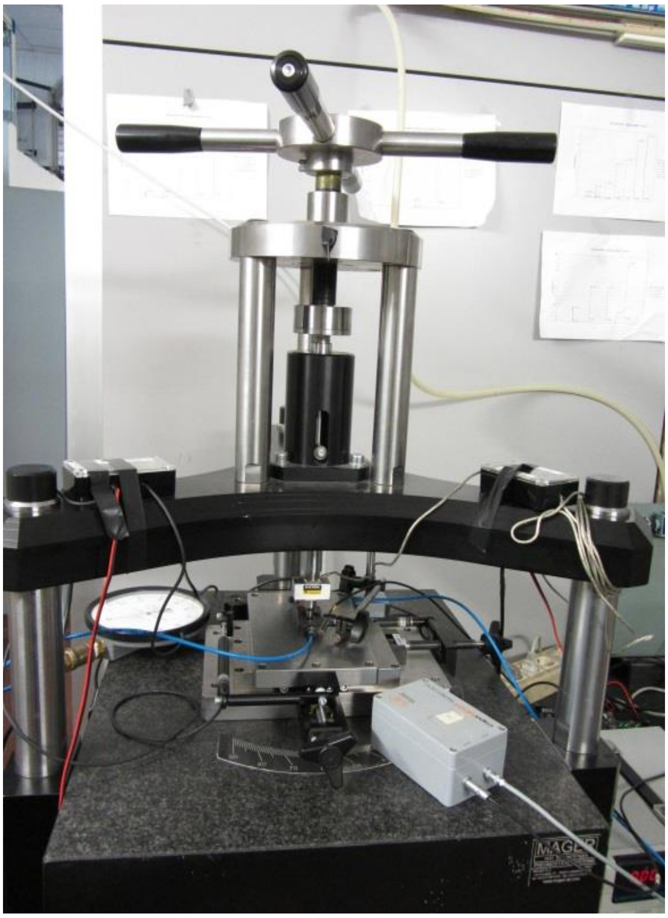

Figure 5.2: Static test bench.

from 0 to 200 Hz. Experimental dynamic stiffness $k$ and damping $c$ were computed from the real and imaginary parts of the frequency transfer function $\dfrac{F(s)}{h(s)}$ which has been experimentally obtained.

## 5.4 Experimental equipment

As illustrated in Figure 5.2, the static test bench consists of various equipment and devices in order to measure the static characteristics of the air pad including load carrying capacity, air gap height and flow rate which are explained in details as follows.

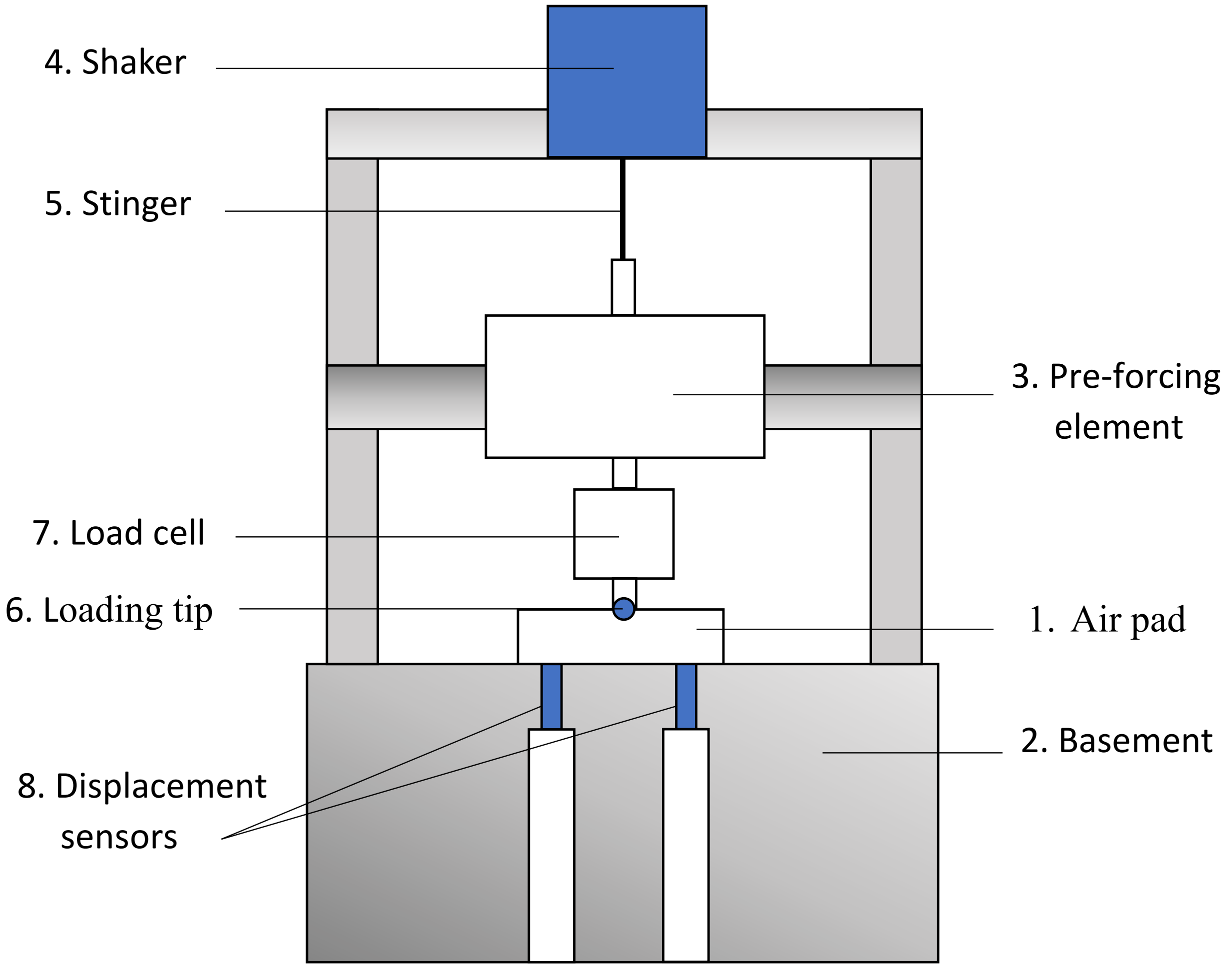

Figure 5.3: Schematic of the test bench.

### 5.4.1 Displacement sensors

The aim of a displacement sensor, also called displacement gauge, is to measure the distance between a reference position (sensor) and the object. A displacement sensor is also able to measure a body's dimensions such as the height, thickness and width. Non-contact and contact measurements are two categories of displacement sensors which utilize light or magnetic fields/sound waves or direct contact with the intended object respectively.

In our experiments two different types of displacement sensors are used to measure the height of air gaps. A LVDT Dial Gauge MAHR 1318 is used in the static test set up and a Microsense 8810 displacement capacitive sensor is used in the dynamic test bench.

### 5.4.2 LVDT Dial Gauge: MAHR 1318

This sensor was used in static test bench to measure the air gap height. A linear transducer is a device that provides voltage as an output which is associated to the parameters being measured. A linear variable differential transformer (LVDT) is an electromechanical sensor that transform mechanical motion to electrical voltage. A schematic of LVDT could be seen in Figure 5.4.

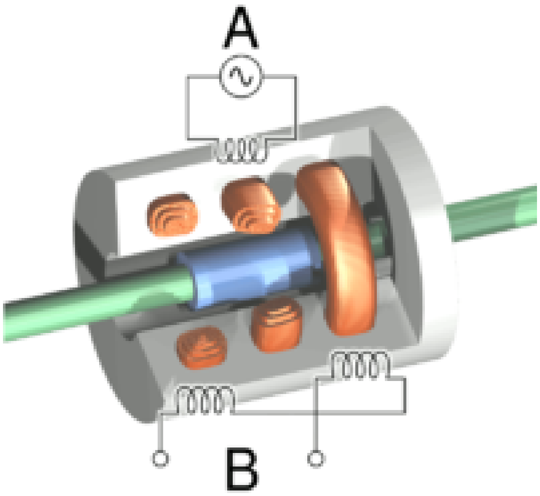

Figure 5.4: LVDT operating principle.

The core slides along the cylinder's long axis and the goal is to measure the position of the movable object (core). A standard LVDT includes three coils which are lined end-to-end. Two secondary coils are positions at the two ends of the tube (hollow metallic cylinder) and the primary coil is in the middle. The displacement of the core induces voltage in secondary coils in the annular body of the device for an alternating current (AC) which derives the primary coil. The output voltage is a sinusoidal waveform whose amplitude is proportional to the position of the core. LVDT is considered as a reliable device since small movements in other directions do not change the accuracy. In addition, there is no contact between the core and the cylinder which makes it possible to seal the sensor completely.

In our static test a LVDT Dial Gauge MAHR 1318 was used, due to its flexibility and appropriate size, to measure the gap height under the bearing. It should be mentioned that despite higher accuracy of our capacitive sensors, they were not employed because of their larger size. The schematic of the MAHR 1318 sensor is displayed in Figure 5.5.

The operating range and sensitivity of this sensor is about 1.5 mm and 0.1 $\mu$m respectively. In addition, displacement values could be visualized on a digital screen of the dial gauge signal conditioner/visualizer, Millimar C1208.

Figure 5.5: LVDT Dial Gauge MAHR 1318.

Micrometer probes is connected to the Millimar c1240 compact amplifier which has a measuring range of ±200 $\mu$m with the resolution of 0.01 $\mu$m. this type of amplifier has 3 digital inputs for measuring start, master measurement, send measurement value and 3 digital outputs for good, reject, rework, measuring time. Figure 5.6 presents the amplifier and the position of the displacement detecting probes on the air pad.

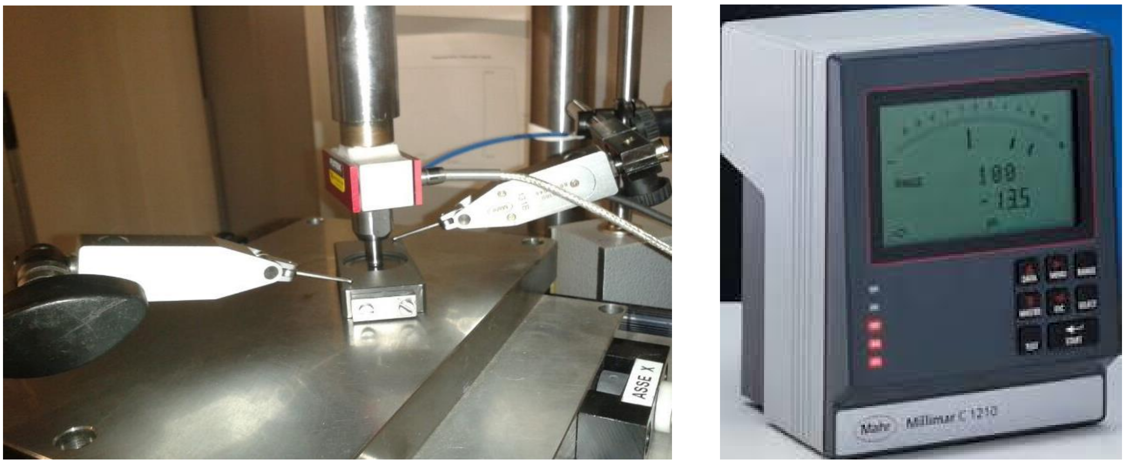

**(a)** **(b)**

Figure 5.6: (a) position of the MAHR 1318 LVDT dial gauge probe on the pad, and (b) Millimar c1240 compact amplifier.

### 5.4.3 Displacement Capacitive Sensors: Microsense 8810

This sensor was used in dynamic set up for measuring the height position of the pad which indicates the air gap. Capacitance sensors (capacitive linear displacement sensors) are extensively used through a variety of industries. These sensors offer highly stable and accurate displacement, vibration and position measurements. Capacitive sensors work based on an electrical property which is called “capacitance”. Capacitance exists between any two conductive surfaces located within reasonable proximity. Figure 5.7 shows the schematic of a capacitive sensor. Any change in distance between two surfaces will change the capacitance value. Capacitance is also directly proportional to the sizes of the sensor and the target and properties of the material between them. Assuming constant values for the mentioned properties, as the size of the gap between the sensing surface and the target is inversely proportional to the quantity of capacitance, any change in position of the target could be accurately detected by these types of sensors.

A Microsense 8810 displacement capacitive sensors are employed in our step force test bench to measure the displacements (see Figure 5.3). As this sensor take advantage of a DAQ system, signals with high dynamic range could be accurately measured, i.e. bandwidth up to 10 kHz and high resolution of 10 nm are reachable.

Figure 5.7: Microsense 8810 displacement capacitive sensor.

The diameter of the sensor defines the range of a capacitance sensor. The relationship is so that the larger area concludes in the greater measurement range. When the probe touches the target the measurement range is specified as the output from the amplifier is zero volts at this point. The amplifier output indicates 10 volts in the case when the gap is as high as the full scale measurement range of the capacitive system. To operate below 10 percent of the gap is not recommended, although in theory the probe can operate everywhere between these two extremes. The ideal standoff distance is to be mentioned somewhere between 5Vdc to 7Vdc where the target is allowed to move closer to or further away from the probe without going out of range. A simplified diagram showing range, output voltage and recommended standoff for a capacitance sensor is illustrated in Figure 5.8.

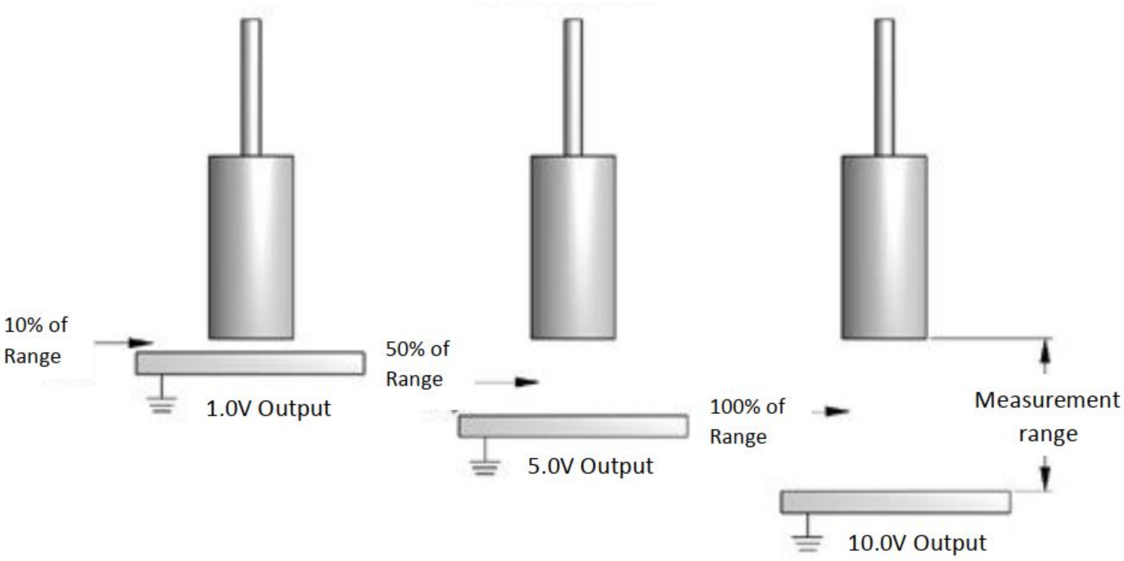

Figure 5.8: Recommended standoff for the displacement capacitive sensor.

### 5.4.4 Load cell

A sensor which converts input mechanical force to an electrical output signal is called Load Cell. A Futek LRF300 which is a piezoelectric load cell is used in the static test bench to measure the force. The assembled load cell into the test rig is shown in Figure 5.9. The sensor is located between the loading tip and the movable link. This sensor is a small size transducer and with sensibility of 2 mV/V is able to measure the load with the highest load limit of 4450 N. The load cell is attached to the loading tip on one side and it is connected to movable link on the other side. A voltage is produced by the piezoelectric material. This voltage is proportional to the deformation of the load cell and is acquired and transformed to the load with a Mecostrain signal Conditioner by MECO. The acquisition system uses a Wheatstone bridge technology with a permissible voltage range of 9.5 to 25 V DC. By adjusting the internal jumper connection and supply voltage the signal conditioner gain of 2mV/V to 20mV/V is achievable.

### 5.4.5 Rotameter

A rotameter of type Rota Yokogawa L742-ALGN-11501 is used as an industrial tool to measure the flow rate of liquids or gases. Simplicity of installation, linear

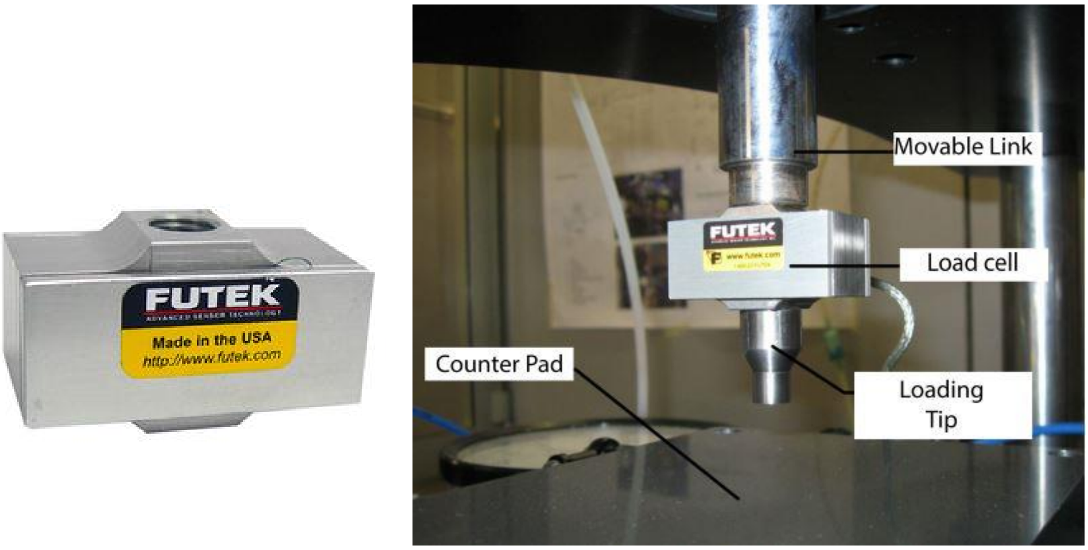

Figure 5.9: Futek LRF300 and the measuing position on the set up.

scale, relatively long measurement range and low-pressure drop have made rotameters a popular and widely used instrument for flow rate quantification. A rotameter includes a glass tube and a float. Floats with different shapes offer rotameters with different operational ranges and characteristics. The float movement is almost linear and independent of viscosity and it moves inside a cone. The position of the float can be used as an indicator of flow rate. The weight of the float is an important parameter in rotameters; therefore, it should be installed vertically. The forces applied to the float should satisfy the following force equilibrium equation

$$\sum F = \bar{S} + \bar{A} + \bar{G} = 0 \tag{5.1}$$

where $\bar{G}$, $\bar{S}$ and $\bar{A}$ are weight of the float, buoyancy and drag forces respectively as illustrated in Figure 5.10.

Two flanges are attached to the two ends of the tube which allow the air to flow through the rotameter. The air enters from the bottom and exhausted from the top and the position of the float is directly proportional to the flow rate, i.e. for every invariable flow rate the float reaches a distinct position. The float in the tapered tube can move up or down by increase or decrease in the flow rate respectively. It reaches a stable point when the force applied by the flowing fluid is equal to the gravitational force as result of the float weight.

In the test a Rotameter Rota Yokogawa L742-ALGN-11501 has been chosen with the aim of measuring the bearing air consumptions. This rotameter is able to measure the flow rate in the operating range of 0.3338 to 7.667 Nl/min.

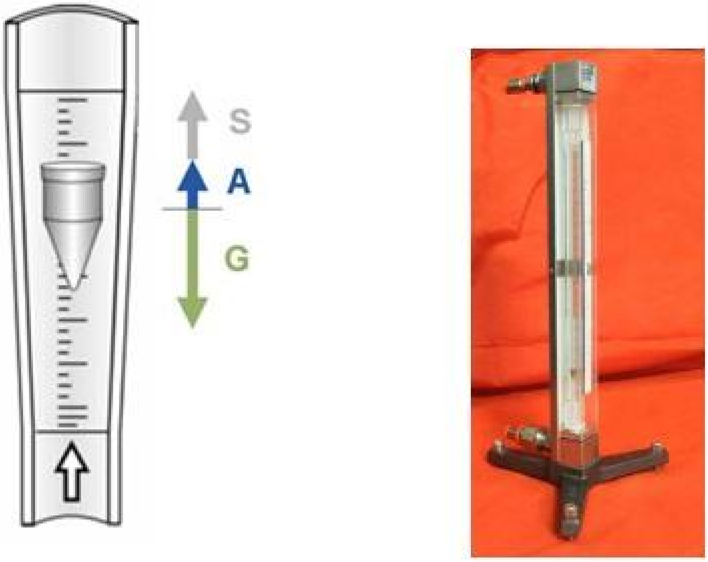

Figure 5.10: The Rota Yokogawa L742-ALGN-11501 rotameter with its operating force equilibrium principle.

### 5.4.6 Pressure gauge

A Brannan 34/655/0 positive analogue pressure gauge with entry of 10bar, and a connection size of BSP 3/839.57 was used to measure the supply air pressure. This pressure gauge has both bar and psi indicators and is dual scale. Analyzing the applied force by a fluid on a surface concludes in the pressure measurement. The Bourdon pressure gauge is a mechanical device whit the concept of the tendency of a flattened pressurized tube to straighten or regain its circular cross section form.

The hollow end is connected to a flattened thin wall with a closed-end tube to the container of the fluid pressure which is aimed to be measured. The closed end of the tube moves in an arc by the increase of the pressure, which then by use of a connecting link is converted into the rotation of an adjustable gear. For further magnification of the motion by a gear ratio, a pinion gear with a small diameter is positioned on a shaft. In order too calibrate the pointer to indicate the variation of the pressure, the initial pointer shaft position, the positioning of the indicator card behind the pointer, the linkage length are all determining parameters.

It should be noted that the measured pressure is absolute pressure that is the gauge pressure relative to ambient pressure. For the case of vacuum, it is considered as a reverse motion. To avoid unnecessary wear on the gears and provide an average reading in the cases when the measured pressure is rapidly pulsing, an orifice restriction in the connecting pipe is used.

Figure 5.11: Brannan analogue positive pressure gauge.

### 5.4.7 Optical microscope: Leica Optical Microscope Z16 APO

The Leica Z16 APO is a microscope with fully apochromatic zoom system. This microscope, in presented in Figure 5.12, provides high contrast, resolution, sharpness, image fidelity and color fidelity images which makes it possible to have a detailed analysis of objects. Leica Z16 APO is a reliable and appropriate equipment for the experiment as it benefits from automated macroscopes, motorized control of the zoom, iris diaphragm and fine focus. A 16:1 zoom with a zoom range of 0.57x to 9.2x is offered by this microscope which delivers magnification level of up to 115x with standard configuration. In addition, a magnification as high as 920x is achievable by using proper optics combination.

This microscope is employed to measure the diameters of the exhaust holes of the aerostatic bearing. The aim is to evaluate and validate the sizes of the holes with their nominal design sizes.

### 5.4.8 Air feeding circuit

The air feeding circuit related to the static and dynamic test benches is depicted in Figure 5.13. The mass air flow provided to bearings is supplied, controlled and measured by this feeding circuit. It is crucial that the supply air does not contain any dust particles larger than specific size. Also, humidity should not go beyond a certain percentage. If these two conditions are not fulfilled the validity of the experiment might be compromised as the performance of opening of bearing exhaust might not be acceptable.

According to the circuit illustrated in Figure 5.13, air with relative pressure up to 10 bar is supplied by the compressor $S$. Then, the gate valve $V1$ intercepts the supply pressure and then directs it through the pressure regulator $R$, which is responsible to set the supply pressure. Dust particles as large as 0.01 $\mu$m and humidity as high as 99% are canceled by the filter $F$. The $V2$ is a manual ON-OFF

Figure 5.12: Optical microscope: Leica Z16 APO.

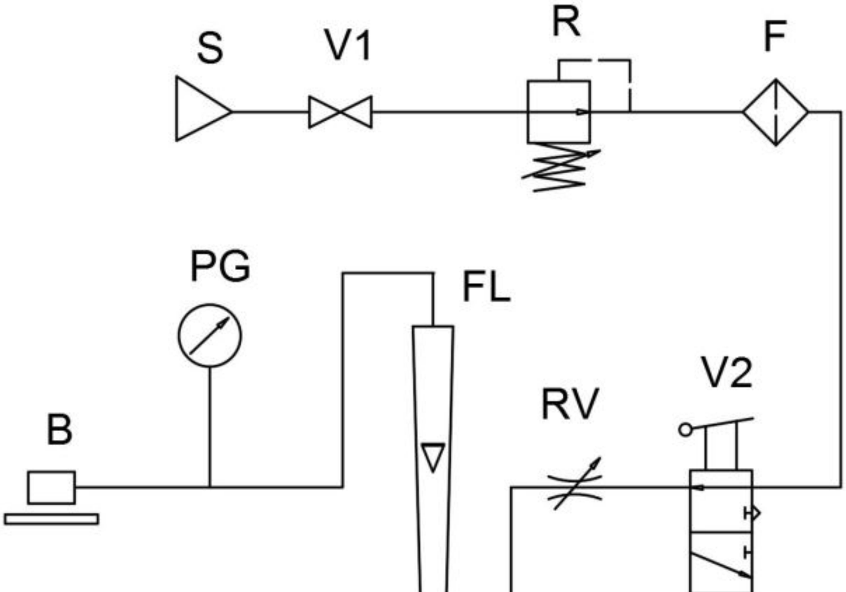

Figure 5.13: The air feeding circuit.

valve which has the responsibility to supply/interrupt and discharge the air mass flow. $RV$, $FL$ and $PG$ are in turn variable flow resistance, flow-meter and pressure gauge which regulates the air flow, measure the up-stream flow rate and pressure respectively.

# Chapter 6

# Results and discussions

## 6.1 Introduction

When it is the matter of development of a new model, always the validation of the model also plays an significant role. Generally, this validation is done by performing some experiments or hiring the other commonly used methods.

This chapter is engaged with obtaining the static and dynamic characteristics of a sample of aerostatic rectangular thrust bearings with the developed lumped model, distributed model and experimental methods. This comparison can be an accurate origin in order to check the accuracy of the developed lumped model and verify it. In static condition the force, air gap and static stiffness are compared, while in dynamic condition the stiffness and damping are the main subjects of the comparison. At the end a applicable coefficient is used to increase the accuracy of the model in the practical range. The effect of geometrical parameters of the pad on its performance and behavior is also discussed in this chapter.

## 6.2 Comparing the results obtained by LP model with those of DP model and experiments

Table 6.1 presents the geometries of pad $A$ which has similar holes distribution that can be simulated by the LP model, and of pad $B$ which was tested experimentally. Indeed, the model has the constraint to consider the same distance $w$ between holes along horizontal and vertical directions.

Pad B is depicted in Figure 6.1. In defining the geometry of pad A, the average distance between the supply holes in $x$ and $y$ directions is considered in order to be simulated with the LP model. In reality, pad A has a non-existing geometry as its numbers of holes in $x$ and $y$ directions are not integer. For example, the number of supply holes along $x$ using Equation 3.2 is $N_x = 2.58$, but the total number of holes is integer and therefore it is possible to simulate this geometry with LP model even though the pad exact geometry does not exist in reality.

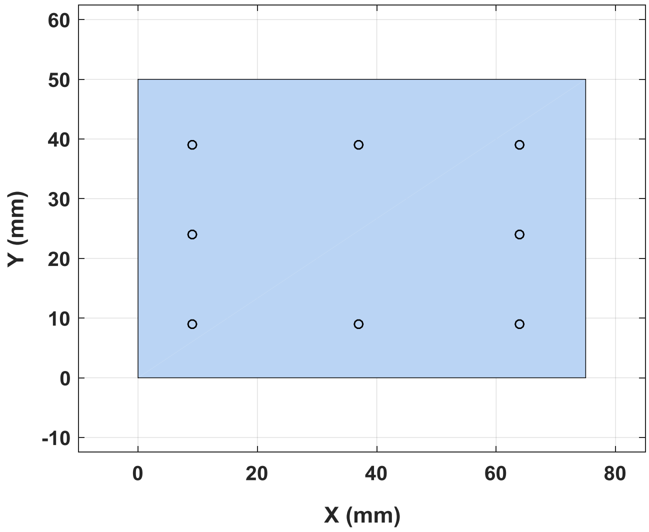

Figure 6.1: Pad B used in the experimental tests.

Table 6.1: Dimensions of pads A and B

| | $N_{tot}$ | $L_x$ (mm) | $L_y$ (mm) | $w_x$ (mm) | $w_y$ (mm) | l (mm) | $d_s$ (mm) |
|---|---|---|---|---|---|---|---|
| Pad A | 8 | 75 | 50 | 21.25 | 21.25 | 10 | 0.3 |
| Pad B | 8 | 75 | 50 | 27.5 | 15 | 10 | 0.3 |

The DP model deals with the solution of Reynolds equation for the thin film flows and the discretization based on finite difference technique under the assumption of isothermal flow expansion:

$$\frac{\partial}{\partial x}(p\frac{h^3}{\mu}\frac{\partial p}{\partial x}) + \frac{\partial}{\partial y}(p\frac{h^3}{\mu}\frac{\partial p}{\partial y}) = 12\frac{\partial(ph)}{\partial t} \tag{6.1}$$

The solution was discussed in details in chapter 4. In addition, Figure 6.2 illustrates the 3D pressure distribution under the pad in static condition obtained by the DP model with absolute supply pressure equal to 5.25 bar and the nominal air gap equal to $h = 10\ \mu m$.

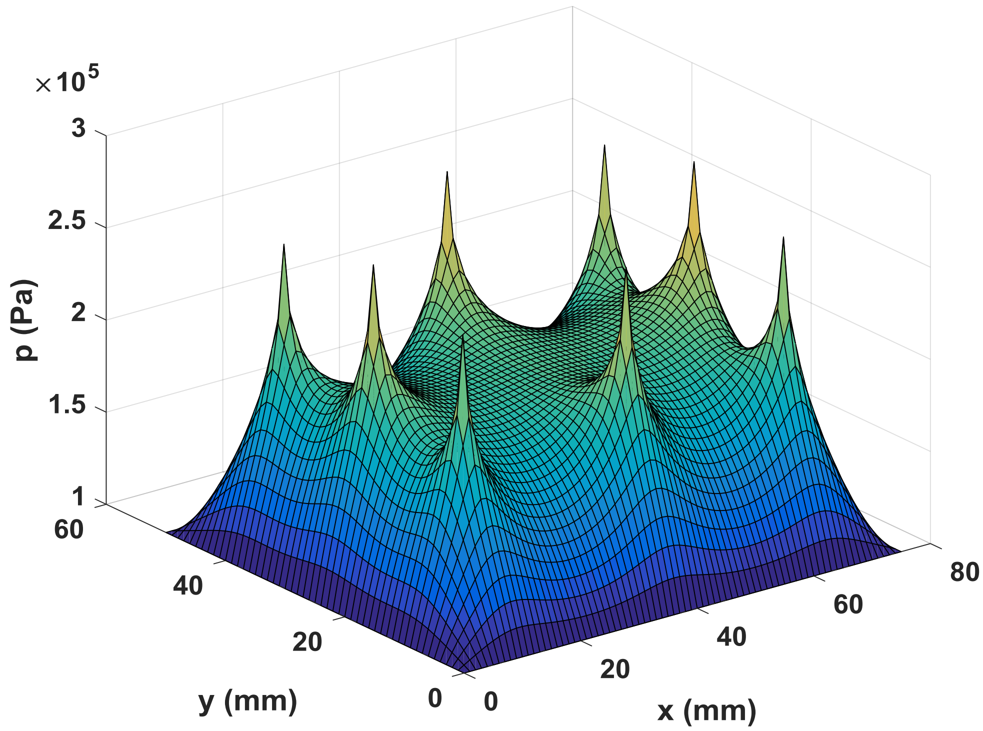

Figure 6.2: Pressure distribution under the pad B with the supply pressure of 5.25 bar and the air gap of 10 $\mu$m, obtained by the DP model.

### 6.2.1 Static case

The static characteristics obtained with the two LP and DP models representing the air consumption, load capacity and static stiffness versus the air gap are compared in Figure 6.3 together with the experimental ones. The comparison is satisfactory and the accuracy of the models is acceptable. It is evident that by increase of the air gap the force is decreased and the air consumption of the pad is increased as expected, and the static stiffness is increased up to the air gap smaller than 15 micrometers and after that for greater air gaps it decreases for all the three graphs.

### 6.2.2 Dynamic case

The dynamic coefficients of stiffness and damping, calculated at the air gaps of 6 $\mu m$ and 14 $\mu$m, with the supply pressure of $p_s = 5.25$ *bar* (absolute), are plotted vs frequency for the two models in Figure 6.4. The LP model with $\Omega$=1 (no correction factor) underestimates the stiffness coefficient especially at low air

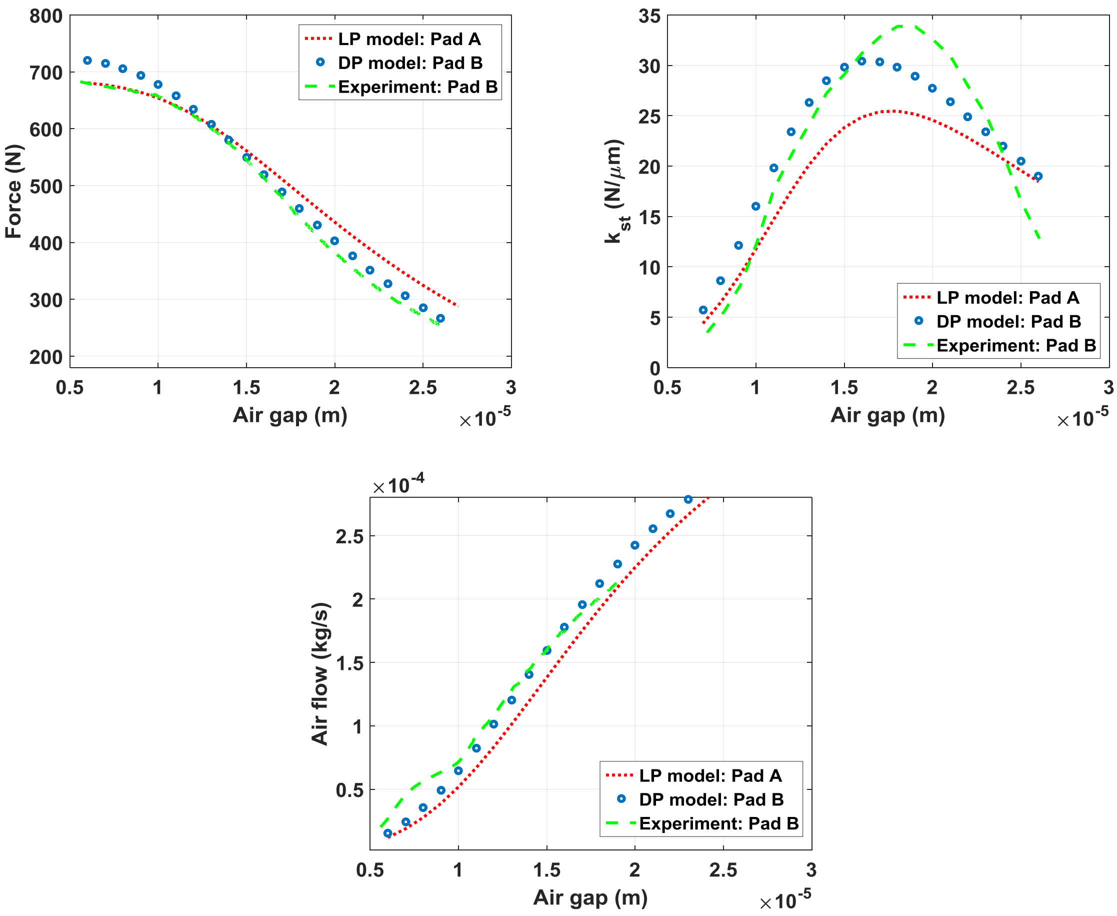

Figure 6.3: Comparison of air flow, force and stiffness in static condition obtained by the LP and DP models and experimental test.

gaps in a frequency range about 100 $Hz$. Moreover, the LP model underestimates the damping coefficient at low frequencies, especially at low air gaps.

The stiffness and damping coefficients obtained at $f = 100$ $Hz$ are plotted vs the air gap.

The experimental results are quite near the numerical results in the range of the air gaps tested in dynamic conditions. About the comparison between the LP and DP models, it is evident that the LP model with $\Omega$=1 (no correction) works properly for estimating the damping, but it underestimates the stiffness, especially at low air gaps. With the correction factor $\Omega$=0.3, the LP model is in a better accordance with the DP model, also at low air gaps. The effect of the correction coefficient is visible also in Figure 6.6, where the stiffness and damping coefficients are shown vs frequency for the air gaps of 6 $\mu m$ and 14 $\mu m$. These values are taken

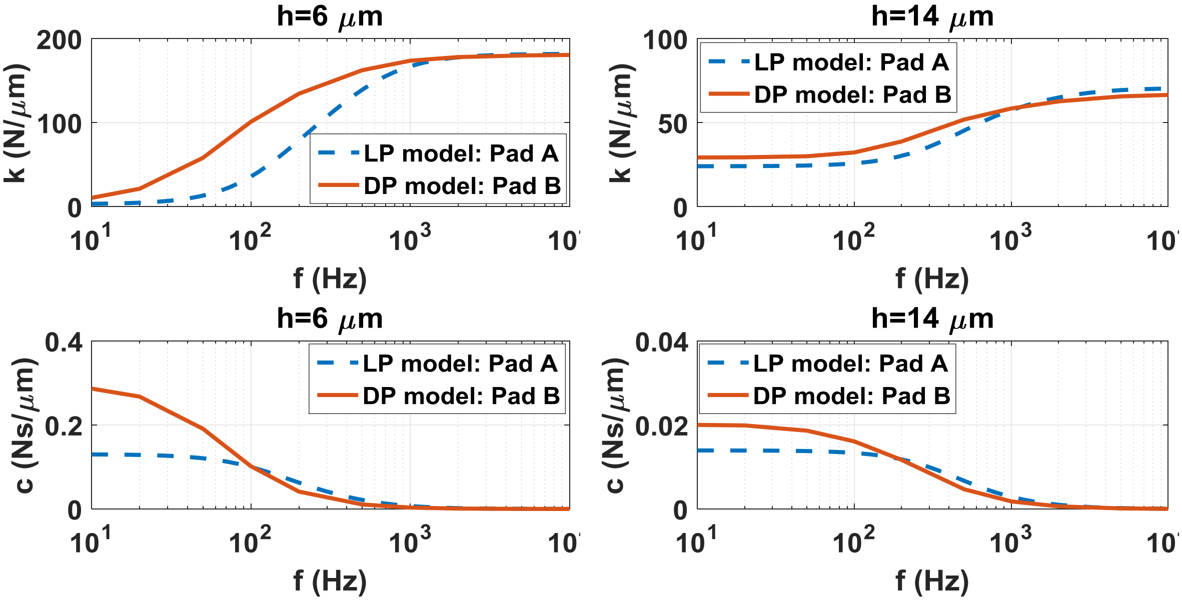

Figure 6.4: Comparison of damping and stiffness in dynamic condition for the air gaps of 6 $\mu$m and 14 $\mu$m, obtained by the LP and DP models.

around the typical working point of the pad. It can be noted that decreasing the coefficient $\Omega$ from 1 (no correction) to 0.3, the accuracy of LP model respect to the DP model improves. This coefficient appears in Equation 3.21 to correct the conductance, calculated with unidimensional formula. As the air flow inside the supply rectangle is bi-dimensional, the unidimensional formula of Equation 3.11 needs a correction factor, otherwise it overestimates the flow.

## 6.3 Computation times

The computation time needed to compute the stiffness and damping coefficients in correspondence of one value of the air gap is compared for the LP and the DP models. About the DP model, two cases are reported: Euler explicit method and linearized perturbation method. Below are the time values obtained with a mesh of $50 \times 75$ nodes:
LP model: 0.01 s
DP model (Euler explicit): 2500 s
DP model (linearized perturbation): 0.1 s
It can be seen that the LP model gives advantages in comparison with the DP models and the perturbation method, which is far more efficient with respect to the Euler explicit method.

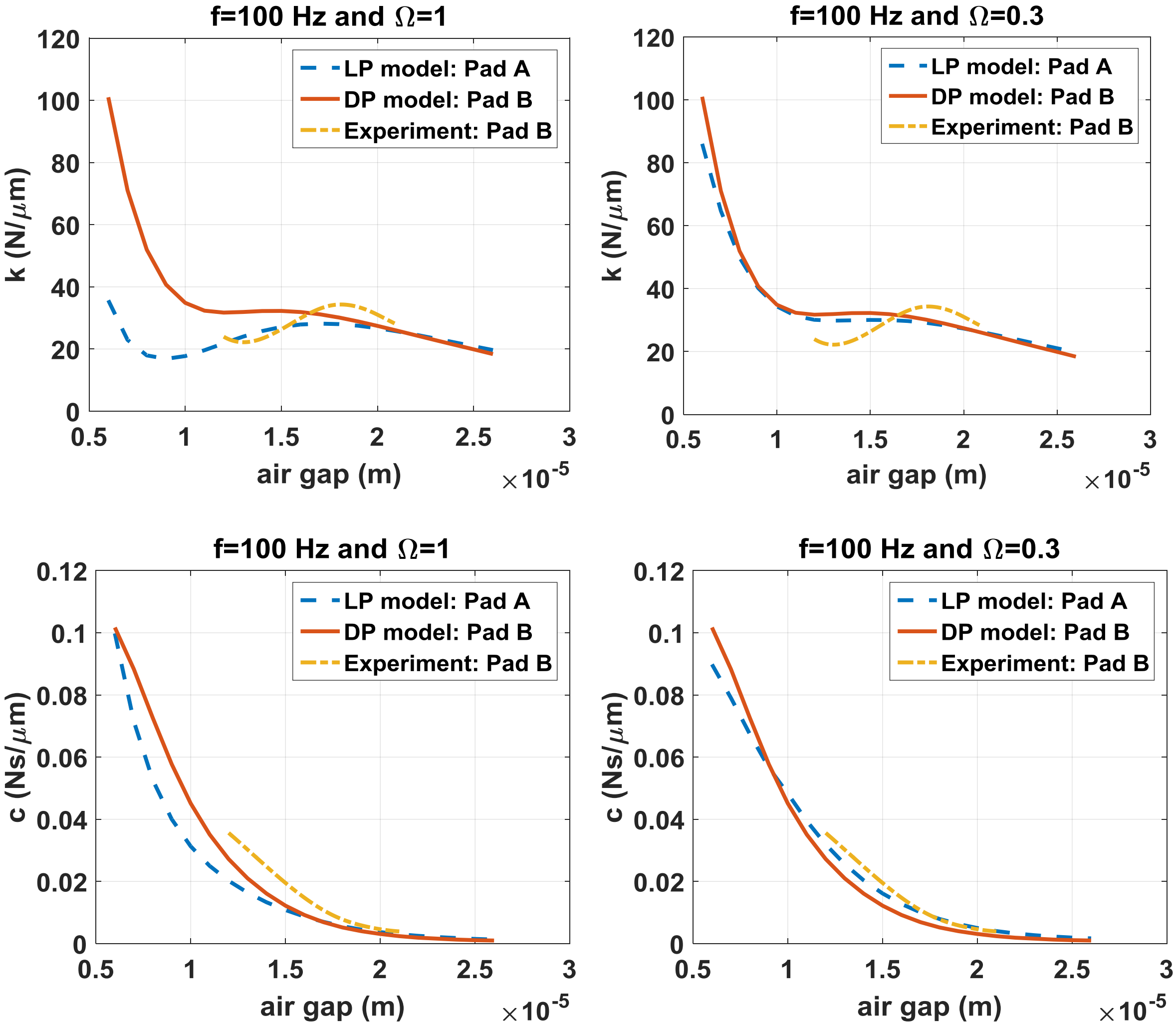

Figure 6.5: Comparison of damping and stiffness in dynamic condition for different air gaps at the frequency of 100 Hz and correction coefficient of 1 and 0.3, obtained by LP and DP models and experiments.

According comparison among the needed computational time, it can be concluded the the use of the LP model can be a handy tool specially for cases of obtaining fast ideas about geometry design of rectangular aerostatic air bearings.

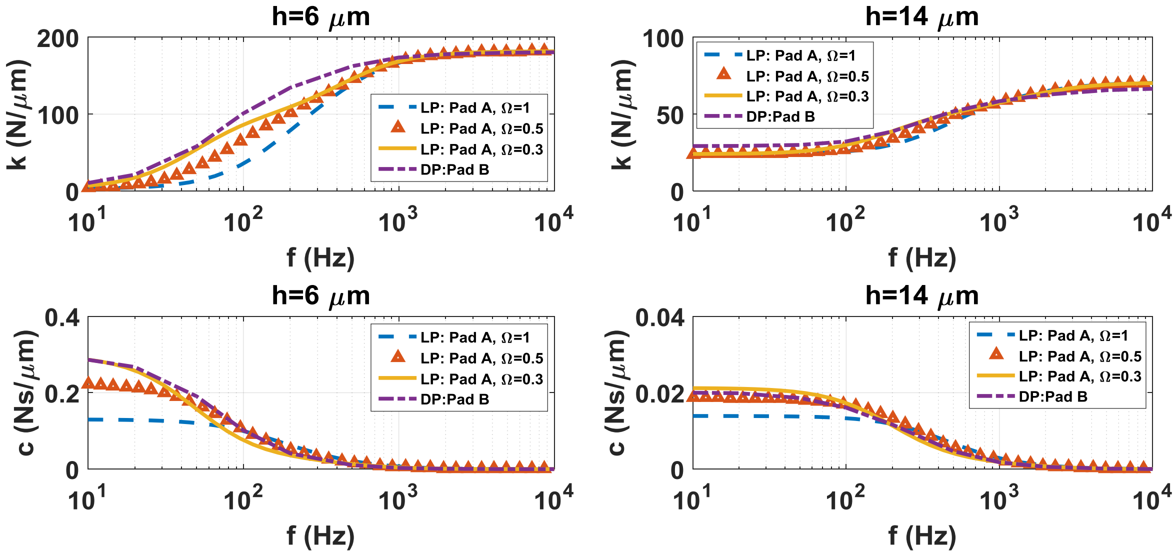

Figure 6.6: The effect of coefficient $\Omega$ on the accuracy of the LP model for the air gaps of 6 $\mu$m and 14 $\mu$m.

## 6.4 Sensitivity study

In this section the effect of some geometrical parameters on static and dynamic characteristics of rectangular air thrust bearings is studied to reach a better design vision. As the LP model is faster and simpler in comparison with the DP model, it is a useful tool for parametric studies and for preliminary design studies of air pads. For this purpose, the effects of changing distance $w$ between holes or distance $l$ between the supply holes and the edges of the pad on the performance of the pad are numerically investigated.

Two study cases with the same total supply holes area are considered. They both analyze three square pads with dimensions 75 × 75 mm supplied at absolute pressure of 5.25 bar. In the first case study, as shown in Table 6.2, the number of supply holes is changed, while keeping the distance $l$ from the pad edges constant. In the second case, the number of supply holes is constant, while the dimensions of the supply rectangle are changed, as indicated in Table 6.3.

According to Figure 6.7, load capacity, air flow and stiffness increase with the increase of the supply holes number. On the other hand, as Figure 6.8 shows, moving the supply holes towards the edges of the pad (second case study) causes a decrease in the load capacity and an increase in the air flow.

Figure 6.9 and Figure 6.10 investigate the dynamic characteristics of the pads in the two case studies. In the first case study, the stiffness increases by increasing the supply holes number, while the effect on damping is very small. In the second case,

Table 6.2: Parameters of the pads in study case 1

| | $N_{tot}$ | $L_x$ (mm) | $L_y$ (mm) | w (mm) | l (mm) | $d_s$ (mm) |
|---|---|---|---|---|---|---|
| Pad 1 | 4 | 75 | 75 | 50 | 12.5 | 0.4243 |
| Pad 2 | 8 | 75 | 75 | 25 | 12.5 | 0.3 |
| Pad 3 | 16 | 75 | 75 | 12.5 | 12.5 | 0.2121 |

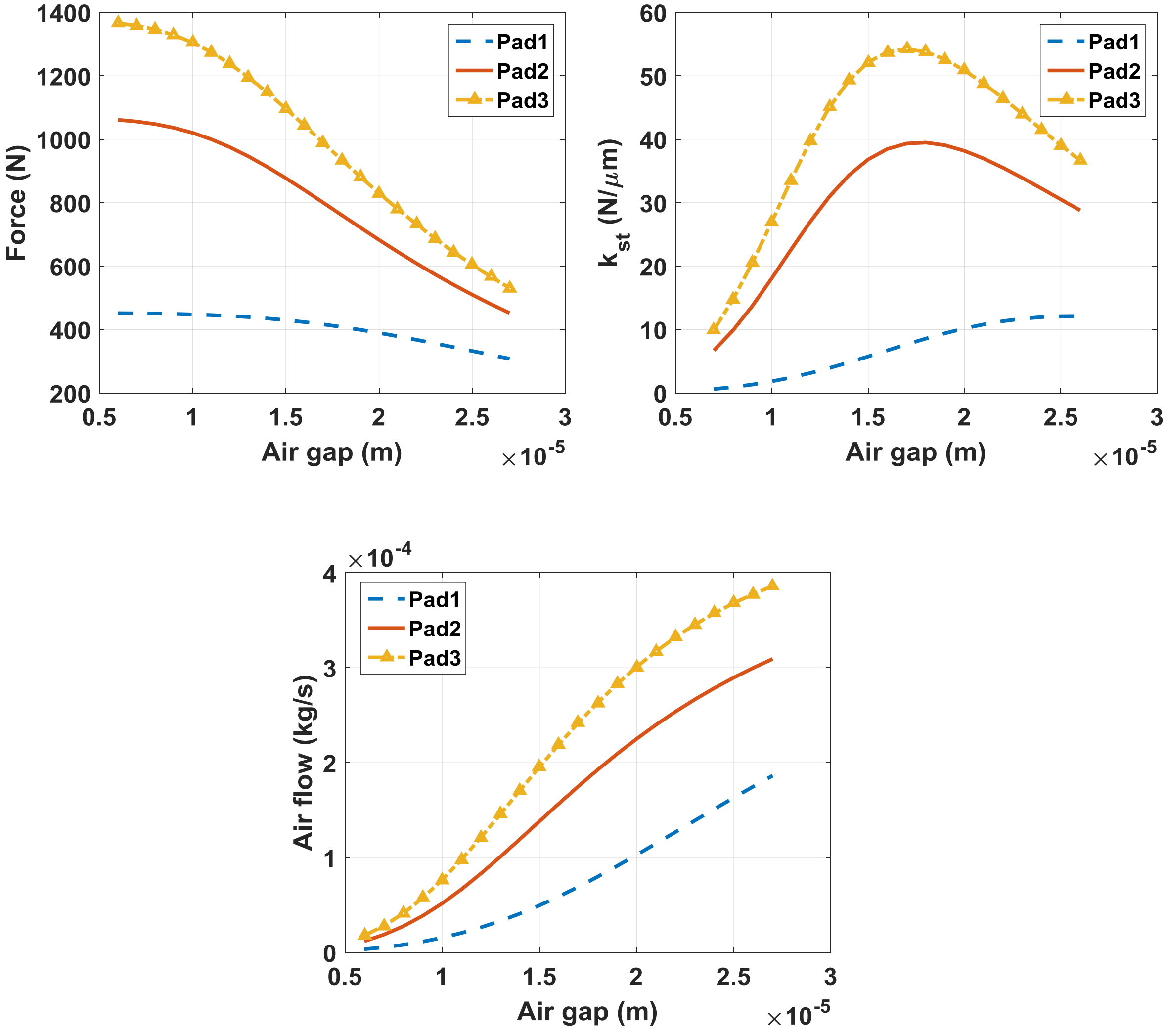

Figure 6.7: Sensitivity study for static characteristics of pads in study case 1

damping coefficient decreases at low air gaps by moving the holes towards the edges

Table 6.3: Parameters of the pads in study case 2

| | $N_{tot}$ | $L_x$ (mm) | $L_y$ (mm) | w (mm) | l (mm) | $d_s$ (mm) |
|---|---|---|---|---|---|---|
| Pad 4 | 8 | 75 | 75 | 20 | 17.5 | 0.3 |
| Pad 5 | 8 | 75 | 75 | 25 | 12.5 | 0.3 |
| Pad 6 | 8 | 75 | 75 | 30 | 7.5 | 0.3 |

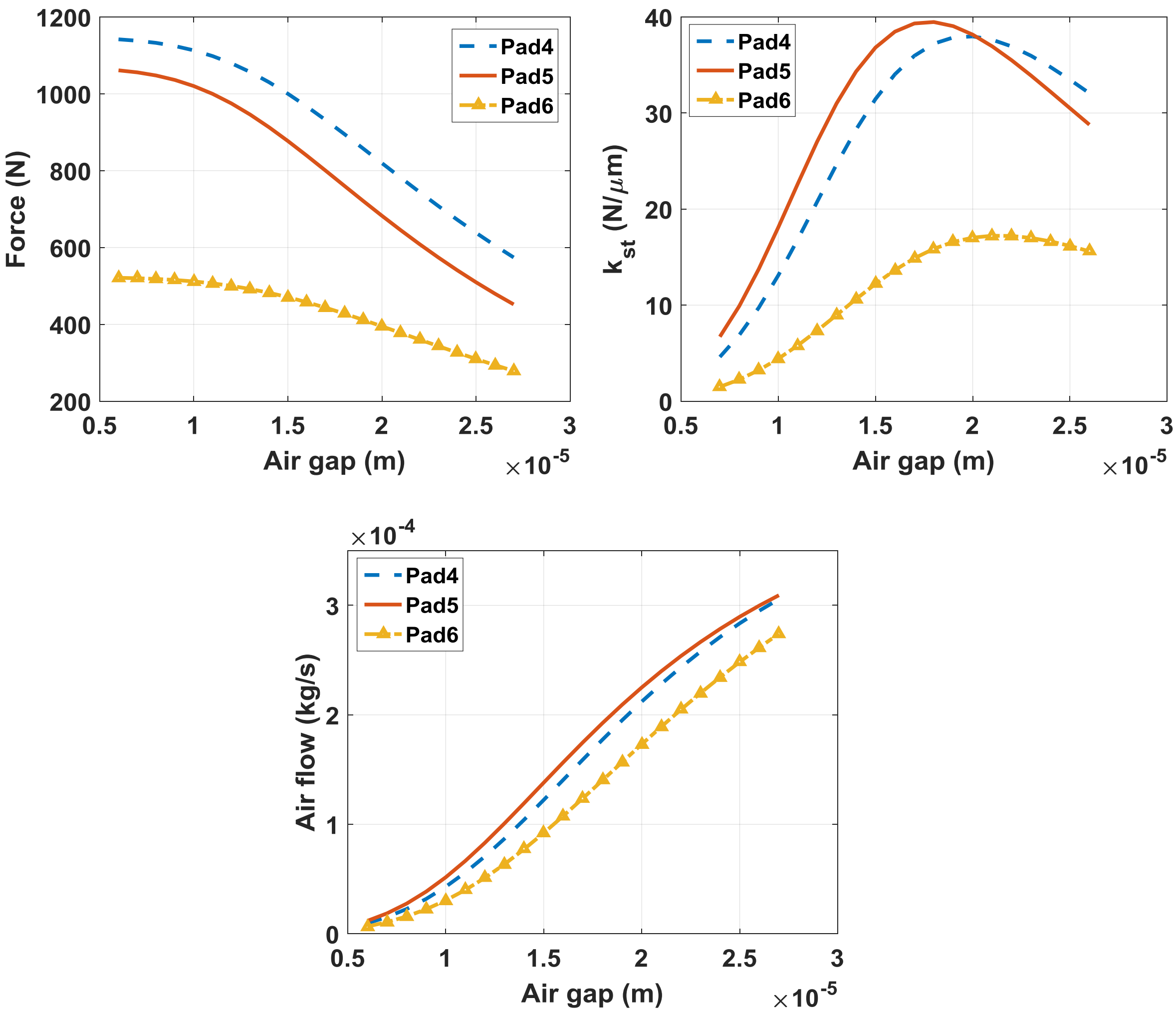

Figure 6.8: Sensitivity study for static characteristics of pads in study case 2

of the pad. About stiffness coefficient, there is an optimal distance of the supply holes from the edges of the pad. In order to design the pad, a compromise between the maximization of the load capacity, stiffness and damping and the minimization

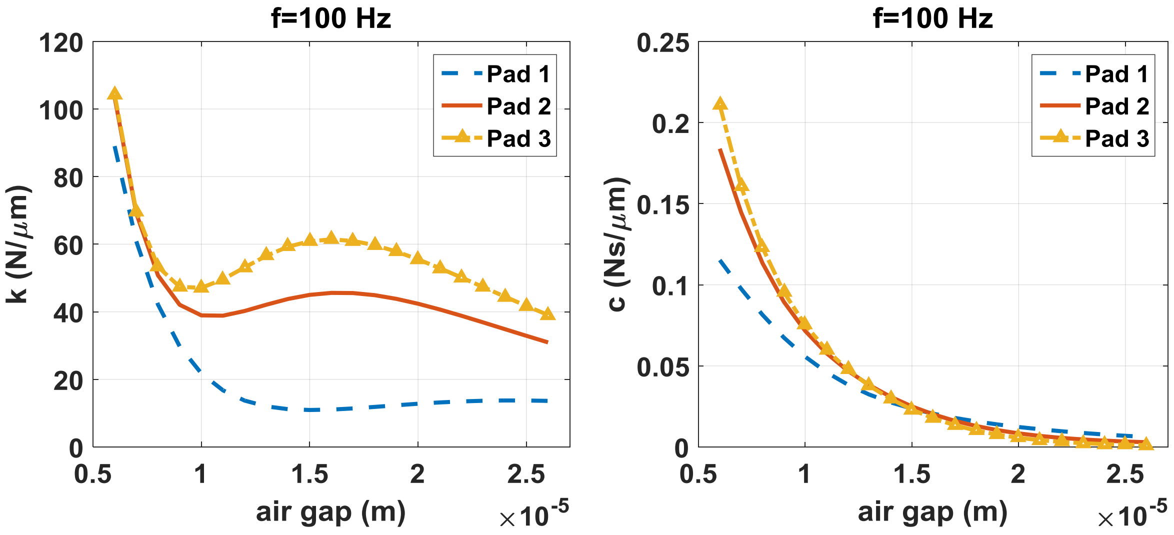

Figure 6.9: Sensitivity study for dynamic stiffness and damping of pads in study case 1

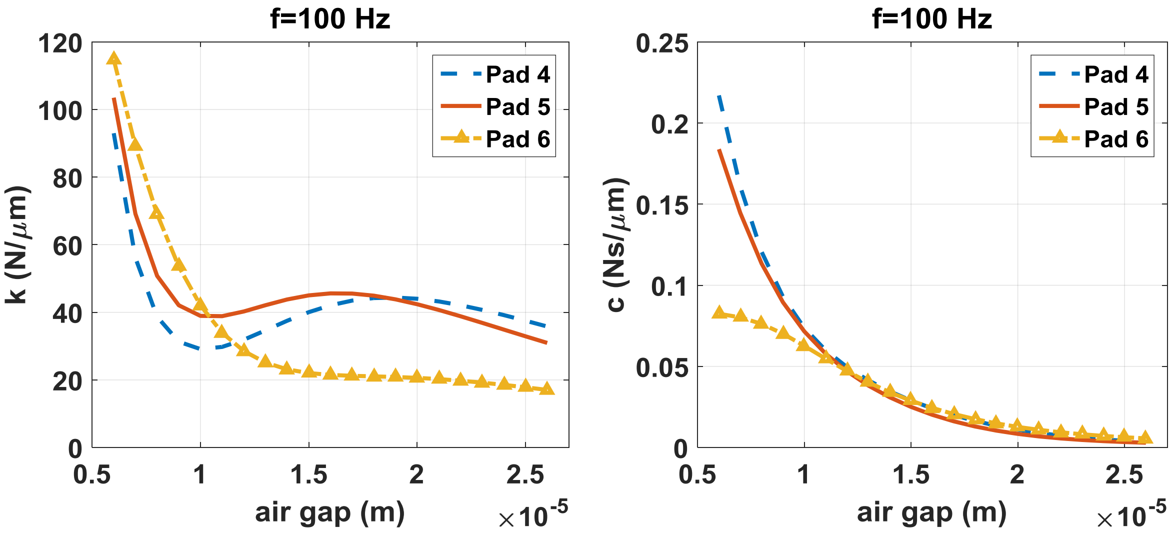

Figure 6.10: Sensitivity study for dynamic stiffness and damping of pads in study case 2

of the air consumption must be found.

## 6.5 Conclusion

The LP model is geometry dependent and it can be used for sensitivity analysis to investigate the effect of geometrical parameters on the pad performances and achieving the best design. An interesting feature of the LP model is that the transfer function between the air gap and the load capacity is expressed in closed form as a function of the geometrical parameters.

From the sensitivity analysis the following conclusions can be listed:

- increasing the number of supply holes and reducing their diameter (in order to keep the total supply holes area constant) with the same distance from the edges of the pad, air flow, load capacity and stiffness increase, while the effect on damping is very small;
- there is an optimal distance for the supply holes from the edges of the pad to maximize stiffness, but the load capacity decreases by reducing this distance.

# Chapter 7

# Squeeze condition [1]

## 7.1 Introduction

The squeeze effect of a gas thrust bearing is calculated using both a distributed parameters (DP) model and a lumped parameters (LP) model. A rectangular thrust bearing with no supply holes is considered in the analysis. In dynamic conditions, pressure values p1 and p2 are calculated. In steady-state conditions these values coincide with ambient pressure pa. The developed LP model was validated with the DP model for a pad shape ratio (length/width) in the range from 0.5 to 2. Both models are validated with literature data in the case of a 1D parallel slider. The LP model has the advantage of faster implementation with respect to the DP model. The LP model is also linearized by using a perturbation method to obtain the analytic expression of the dynamic stiffness. Therefore it is possible to explain the effect of geometrical parameters on stiffness and damping coefficients.

In particular this chapter analyzes theoretically the squeeze film phenomenon of a rectangular pad in absence of the supply inlet holes. The dynamic lumped model is presented; it considers the flow rate due only to the variation of the air gap. The flow rate is linearized to obtain the transfer function of the pressure force respect to the air gap; the dynamic stiffness and damping are calculated at different frequencies. The numerical results are compared with those of a distributed model and are also validated with literature in case of a 1D parallel slider [72].

---

[1] “Part of the work described in this chapter has been previously published in Ref. [71]”

## 7.2 The LP model for squeeze condition

### 7.2.1 Air bearing geometry

A squeeze film rectangular air bearing of size $L_x$ and $L_y$ with uniform air gap is considered. The pad shape ratio is calculated according to Equation 3.2.

In steady-state conditions the pressure under the pad is equal to ambient pressure $p_a$; on the contrary in case the air gap changes with time the pressure is not uniform due to squeeze effect. In the developed LP model two pressure values are considered: pressure $p_2$ is supposed to be constant at distance $l$ from the borders and pressure $p_1$ is supposed to be constant inside volume $V_1$, which is an inner rectangle at distance $2l$ from the borders. Figure 7.1 represents the pad with the supposed pressure distribution. In volume $V_2$, defined outside volume $V_1$, the pressure is supposed linear from the perimeter in which $p = p_2$. Inside volume $V_1$ the pressure is supposed to be constant and equal to $p_1$.

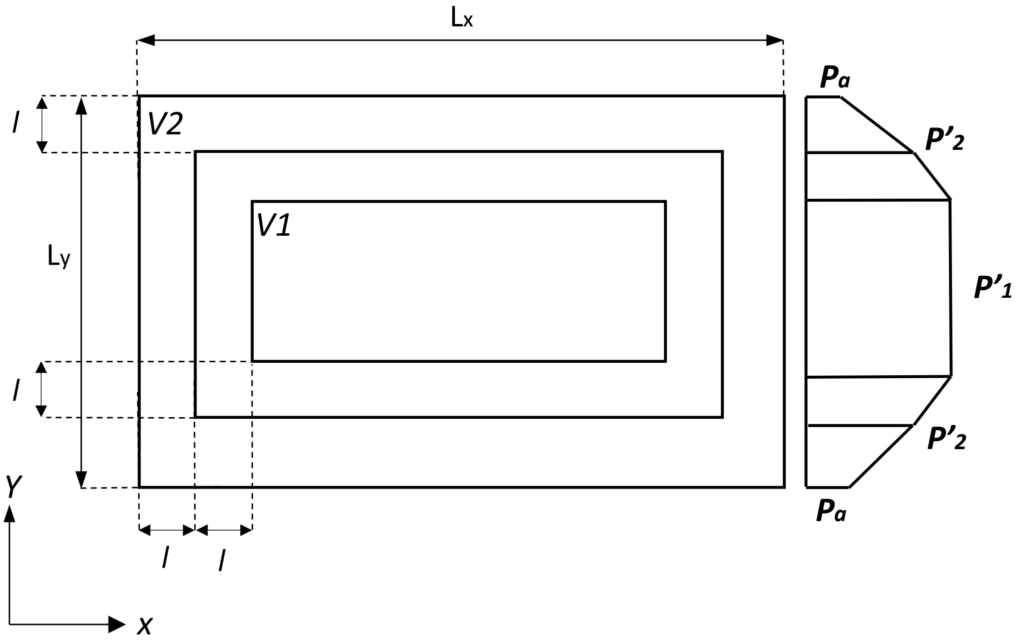

Figure 7.1: Sketch of the pad with dynamic pressure distribution in squeeze condition.

### 7.2.2 Flow balance

According to Equation 7.1 the flow rate $G_1$ entering control volume $V_1$, and the exhaust flow $G_2$ are equal to the following equations and are presented in Figure 7.2:

$$
\begin{aligned}
G_1 &= 2(G_{1x} + G_{1y}) = \frac{h'^3}{6\mu RT}\left(\frac{L_y - 2l}{L_x - 2l} + \frac{L_x - 2l}{L_y - 2l}\right)({p'_1}^2 - {p'_2}^2) \\
G_2 &= 2(G_{2x} + G_{2y}) = \frac{h'^3}{12\mu RT}\left(\frac{L_y - 2l}{l} + \frac{L_x - 2l}{l}\right)({p'_2}^2 - {p_a}^2)
\end{aligned} \tag{7.1}
$$

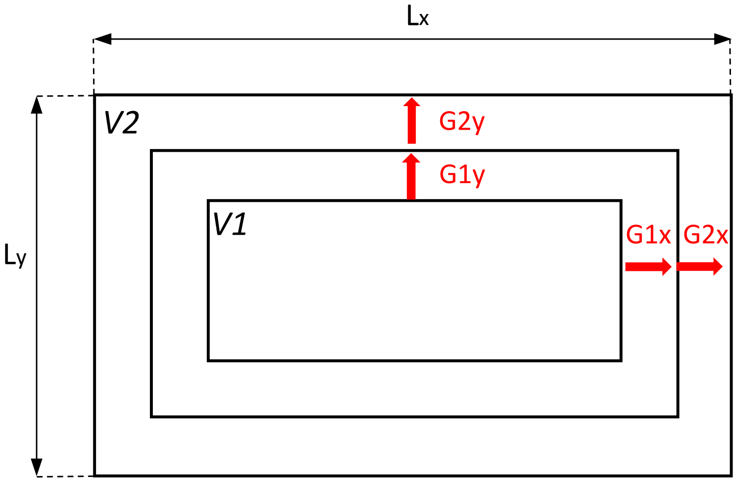

Figure 7.2: Sketch of the pad with mass air flows along x and y directions in squeeze condition.

The mass balance equations for volumes $V_1$ and $V_2$ are:

$$
\begin{cases} -G_1 = \dot{m}_1 \\ G_1 - G_2 = \dot{m}_2 \end{cases} \tag{7.2}
$$

The air masses $m_1$ and $m_2$ in volumes V1 and V2 can be obtained integrating the air density over these volumes under the hypothesis of isothermal expansion:

$$
\begin{aligned}
m_1 &= \int_{A_1} \rho h' dA_1 = \frac{h' p'_1}{4RT}(L_x - 2l)(L_y - 2l) \\
m_2 &= \int_{A_2} \rho h' dA_2 = \frac{h'}{RT}(p'_2[l(L_x + L_y - 4l) + l^2 + \frac{7}{16}(L_x - 2l)(L_y - 2l)] + \\
&\quad + \frac{5p'_1(L_x - 2l)(L_y - 2l)}{16} + lp_a[L_x + L_y - l])
\end{aligned} \tag{7.3}
$$

At this level the resulting continuity equation is non-linear. In the next part these equations have been linearized.

### 7.2.3 Linearization of the squeeze case equation

The obtained equations are linearized exactly using the same method as subsection 3.2.5. The parameters are linearized around the operating point defined by the air gap of $h_0$. By use of the perturbation method to linearize the problem, all parameters in equations are considered as the sum of a constant steady state term and a dynamic term:

$$\begin{aligned} \bar{p'_1} &= p_0 + \Delta p_1 \\ \bar{p'_2} &= p_0 + \Delta p_2 \\ \bar{h'} &= h_0 + \Delta h \end{aligned} \tag{7.4}$$

The steady state values of pressures for a dynamic squeeze film pad are equal to ambient pressure $p_0 = p_a$. The linearized formats of continuity equations in Equation 7.2 are

$$\begin{aligned} -G_{1,0} - \Delta G_1 &= \dot{m}_1 \\ G_{1,0} + \Delta G_1 - G_{2,0} - \Delta G_2 &= \dot{m}_2 \end{aligned} \tag{7.5}$$

The steady state air flows are null so the continuity equations simplify into the following

$$\begin{aligned} -\Delta G_1 &= \dot{m}_1 \\ \Delta G_1 - \Delta G_2 &= \dot{m}_2 \end{aligned} \tag{7.6}$$

where

$$\Delta G_1 = a_6 \Delta p'_1 + a_7 \Delta p'_2 + a_8 \Delta h' = \begin{bmatrix} a_6 & a_7 & 0 \end{bmatrix} \begin{bmatrix} \Delta p'_1 \\ \Delta p'_2 \\ \Delta h' \end{bmatrix} \tag{7.7}$$

$$\Delta G_2 = a_9 \Delta p'_2 + a_1 0 \Delta h' = \begin{bmatrix} 0 & a_9 & a_{10} \end{bmatrix} \begin{bmatrix} \Delta p'_1 \\ \Delta p'_2 \\ \Delta h' \end{bmatrix} \tag{7.8}$$

$$\begin{aligned} a_6 &= \frac{-h_0'^3 p_0'}{3\mu RT}\left(\frac{L_y - 2l}{L_x - 2l} + \frac{L_x - 2l}{L_y - 2l}\right) = -a_7 \\ a_9 &= \frac{h_0'^3 p_0'}{6\mu RT}\left(\frac{L_y - 2l}{l} + \frac{L_x - 2l}{l}\right) \\ a_{10} &= \frac{h_0'^2 (p_0'^2 - p_a^2)}{4\mu RT}\left(\frac{L_y - 2l}{l} + \frac{L_x - 2l}{l}\right) \end{aligned} \tag{7.9}$$

In the Laplace domain the time variation of the masses are

$$\dot{m}_1 = a_1 \dot{\Delta p}'_1 + a_2 \dot{\Delta h}' = \begin{bmatrix} a_1 s & 0 & a_2 s \end{bmatrix} \begin{bmatrix} \Delta p'_1 \\ \Delta p'_2 \\ \Delta h' \end{bmatrix} \tag{7.10}$$

$$\dot{m}_2 = a_3\Delta\dot{p}'_1 + a_4\Delta\dot{p}'_2 + a_5\Delta\dot{h}' = \begin{bmatrix} a_3 s & a_4 s & a_5 s \end{bmatrix} \begin{bmatrix} \Delta p'_1 \\ \Delta p'_2 \\ \Delta h' \end{bmatrix} \tag{7.11}$$

where

$$\begin{aligned} a_1 &= \frac{L_y - 2l}{2}\frac{L_x - 2l}{2RT})h'_0 \\ a_2 &= \frac{L_y - 2l}{2}\frac{L_x - 2l}{2RT})p_a \\ a_3 &= h'_0\frac{5}{16RT}(L_x - 2l)(L_y - 2l) \\ a_4 &= h'_0\frac{1}{RT}[l(L_x + L_y - 4l) + l^2 + \frac{7}{16}(L_x - 2l)(L_y - 2l)] \\ a_5 &= \frac{p_a}{RT}[2l(L_x + L_y - 4l^2) + \frac{3}{4}(L_x - 2l)(L_y - 2l)] \end{aligned} \tag{7.12}$$

Finally the mass balance equations in Laplace domain are written in the compact system

$$\begin{bmatrix} a_1 s - a_6 & -a_7 \\ a_3 s + a_6 & a_4 s + a_7 + a + 9 \end{bmatrix} \begin{bmatrix} \Delta p'_1 \\ \Delta p'_2 \end{bmatrix} = -\begin{bmatrix} a_2 s \\ a_5 s + a_{10} \end{bmatrix} \Delta h' \tag{7.13}$$

from which it is possible to obtain the pressures $p_1$ and $p_2$

$$\begin{bmatrix} \dfrac{\Delta p'_1}{h'} \\ \dfrac{\Delta p'_2}{h'} \end{bmatrix} = -\frac{1}{a_{11}} \begin{bmatrix} a_7 a_9 s^2 + [a_2 a_{10} + a_7(a_2 + a_4)]s + a_2 a_5 \\ (-a_8 a_7 + a_6 a_{10})a^2 + [-a_1 a_7 + a_5 a_6 - a_1 a_{10}]s \end{bmatrix} \tag{7.14}$$

where

$$a_{11} = a_6 a_9 s^2 + [-a_1 a_9 + a_6(a_2 + a_4) + a_2 a_8]s - a_1 a_4 \tag{7.15}$$

### 7.2.4 Transfer function

The pad load carrying capacity $F$ is calculated by integration of the pressure distribution under the pad. Afterwards, an expression of the transfer function in Laplace domain is obtained

$$\frac{\Delta F(s)}{\Delta h'(s)} = M\frac{\Delta p'_1(s)}{\Delta h'(s)} + N\frac{\Delta p'_2(s)}{\Delta h'(s)} \tag{7.16}$$

where M and N are coefficients depending on the geometry of the pad:

$$M = \frac{9(L_x - 2l)(L_y - 2l)}{16} N = l(L_x + L_y - 2l) + \frac{7}{16}(L_x - 2l)(L_y - 2l) \tag{7.17}$$

The coefficients of stiffness and damping of the pad can be obtained from the real and imaginary parts of the transfer function

$$\frac{\Delta F(s)}{\Delta h'(s)} = k(s) + c(s)s = \frac{b_1 s^2 + b_2 s + b_3}{b_4 s^2 + b_5 + b_6} \tag{7.18}$$

where

$$\begin{aligned} b_1 &= -M a_2 a_4 - N(-a_3 a_2 + a_1 a_5) \\ b_2 &= -M[-a_6 a_5 + a_2(-a_6 + a_9)] - N[-a_6 a_2 + a_1 a_{10} - a_6 a_5] \\ b_3 &= (M+N) a_6 a_{10} \\ b_4 &= a_1 a_4 \\ b_5 &= [-a_6 a_4 + a_1(a_7 + a_9) + a_7 a_3] \\ b_6 &= -a_6 a_9 \end{aligned} \tag{7.19}$$

If the frequency $\omega$ is introduced, then it is possible to obtain analytical expressions for stiffness and damping

$$\frac{\Delta F(\omega)}{\Delta h(\omega)} = \frac{((b_3 - b_1\omega^2)(b_6 - b_4\omega^2) + b_2 b_5 \omega^2}{((b_6 - b_4\omega^2)^2 + b_5^2\omega^2)}) + j\omega \frac{(b_2(b_6 - b_4\omega^2) - b_5(b_3 - b_1\omega^2))}{((b_6 - b_4\omega^2)^2 + b_5^2\omega^2)} \tag{7.20}$$

## 7.3 Results and discussions

### 7.3.1 Static condition

In static condition the stiffness coefficient is

$$k(\omega = 0) = \frac{b_3}{b_6} = \frac{-((M+N)a_1 0)}{a_9} = -(M+N)\frac{3(p_0^2 - p_a^2)}{(2h_0 p_0)} = 0 \tag{7.21}$$

as $p_0 = p_a$ The static damping is

$$c(\omega = 0) = \frac{(b_2 b_6 - b_5 b_3)}{b_6^2} \tag{7.22}$$

In this case damping is not zero. This can be explained due to viscosity which creates a shear stress which opposes to the pad vertical movement.

### 7.3.2 Comparison with the distributed model

The pad was simulated in dynamic conditions with a distributed parameters model which integrates Reynolds equation under the pad chapter 4. The air gap was perturbed near $h_0 = 10\mu$m with a sinusoidal function of amplitude $\Delta h = 0.5\mu$m at different frequencies

$$h = h_0 + \Delta h \sin(\omega t) \tag{7.23}$$

Figure 7.4 shows the load carrying capacity $F$ and the air gap $h$ vs angle $\omega t$.

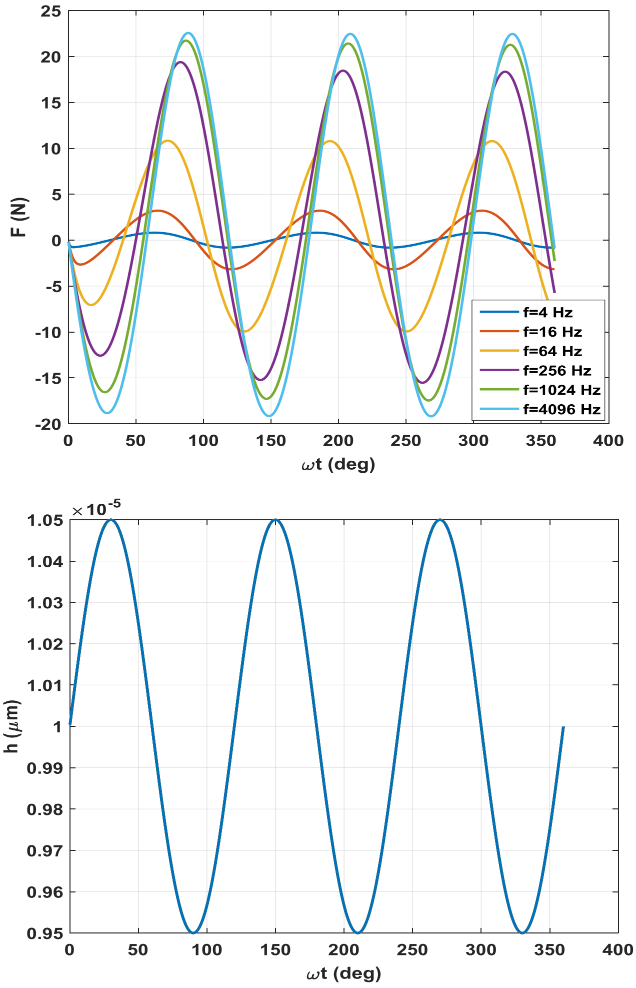

Figure 7.3: Load capacity and air gap vs angle $\omega t$ for different frequencies for the pad under squeeze condition.

From these results the coefficients of stiffness and damping were calculated measuring the phase shift between $F$ and $h$. The results are compared in figures 4 and 5 with those of lumped model for a pad of size 30 × 60 mm. Distance $l = 5$ mm was assumed to define volumes $V_1$ and $V_2$. If compared with the DP model, the LP model is much less expensive in terms of computational time.

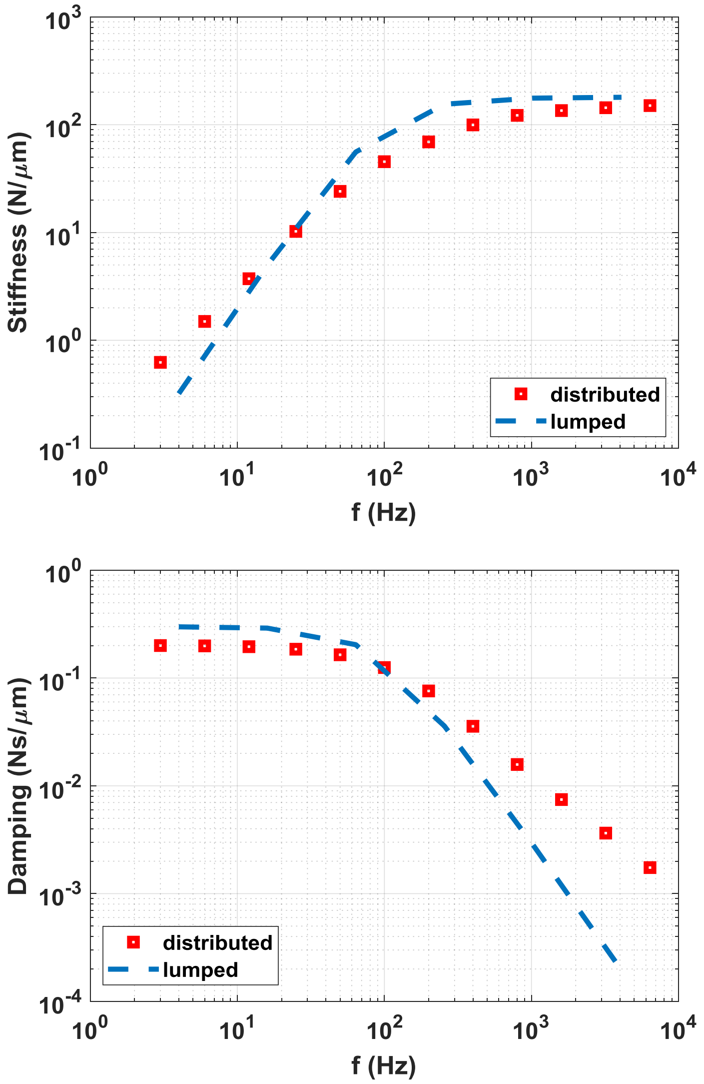

Figure 7.4: Comparison of the stiffness and damping obtained with lumped and distributed parameter models for the pad under squeeze condition.

### 7.3.3 Literature validation

The LP model was compared with literature paper [72] in which a 1D slider is considered and an analytical formulation was given. To approach the pressure distribution of a mono-dimensional slider, a pad with aspect ratio $\beta = 5$ was considered. In this case the length of pad is sufficiently greater than the other side and it is possible to have a good approximation of the mono-dimensional slider. Stiffness

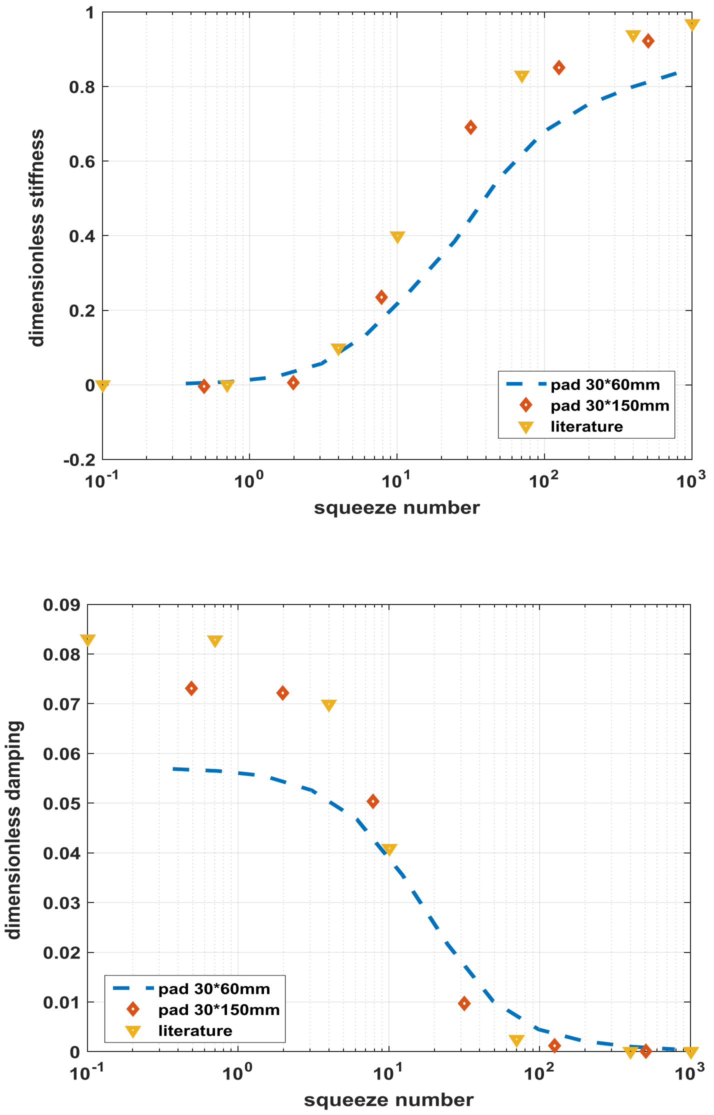

Figure 7.5: Comparison between dimensionless stiffness and damping calculated with LP model and 1D slider for the pad under squeeze condition.

and damping are shown in dimensionless form using the following definition:

$$\begin{aligned} \bar{k} &= \frac{(kh_0)}{(L_x L_y p_a)} \\ \bar{c} &= \frac{(ch_0\omega)}{(L_x L_y p_a)} \end{aligned} \tag{7.24}$$

Dimensionless frequency is defined by the squeeze number

$$squeeze\ number = \frac{(24\mu\pi\omega L_x^2)}{(P_a h_0^2)} \tag{7.25}$$

According to Figure 7.5 it is evident that the pad of aspect ratio $\beta = 5$ has coefficients more similar to that of the mono-dimensional air slider. Moreover the LP model gives a reasonable results in comparison with literature.

## 7.4 Conclusion

The LP model can be used to obtain the stiffness and damping coefficients of a rectangular squeeze film pad. The results were compared with the results of distributed parameters model and yield an enough accurate approximation. The LP model was also validated with literature in case of a mono-dimensional slider [ref]. It is evident that the computational time of LP model is much less than that of distributed model, so LP model can be a practical instrument for design of air bearings also in squeeze performing conditions.

# Chapter 8

# Conclusion and future work

## 8.1 Conclusion

The research presented in this thesis deals mainly with developing a less complicated, fast and enough accurate method for study of aerostatic rectangular air bearings in comparison with current common methods. After presenting a short investigation in thin film history and the progress in solving Reynolds equation the invention of air bearing and use of the very first air bearings in industry is discussed. The chapter continued with explanation of different kind of pads, their applications and various characteristics of these kinds of air pads which makes them different from each other to become appropriate for various kinds of application and fulfill the demands of industry.

After the literature review the thesis deals with obtaining the main goal of this research, which is developing the LP model. This model is mainly developed for dynamic studies as in dynamic condition there are more complexity added to study of air bearings leading to more computing time consumption. The LP models starts with continuity equations for the inlet and outlet air flow through the path and the equivalent electric system of the air pad is introduced, and the resistances through the flow path from the inlet supply holes down to exhausting to ambient pressure at the edges of the pad are presented. All the continuity equations are obtained using the formula for isothermal viscous flow in rectangular channels and afterwards for sake of simplicity they are all linearized around the static point by use of perturbation formula and Taylor expansion method. All the equations are linearized using Mathematica and afterwards being imported in MATLAB. Therefore it should be noted that in this method performing the static analysis at first yields a proper start for the dynamic study to be performed at the next step of the study as the linearization is applied for all the terms of continuity equations around their static values.

At the last step the pressure distribution is calculated for the rectangular air pad which in turn leads to calculation of the load carrying capacity of the pad.

Finally, by forming the transfer function for the specific pad in Laplace domain, that is the ratio between the load carrying capacity of the pad versus the imposed vibrational air gap under the pad, it is possible to obtain separately the imaginary and real parts of this transfer function which are in turn damping and stiffness of the proposed pad.

After developing the LP model the thesis deals with verifying the accuracy of the LP model. The verification process is done by comparing the model with two different methods. The results of LP model were compared by those obtained by DP model and by experimental results. DP model deals with Reynolds equation and its solution using the finite difference method and finite difference solution. The model is later on implemented in MATLAB by use of euler explicit method. The results are obtained for the same rectangular pad used in LP model and the comparison yields an enough accuracy of the developed LP model.

The next part of the research is dedicated to the experimental validation of the model which is performed by hiring two different test setups for the static and dynamic study of the rectangular pad. The static test bench is used to obtain the static characteristics of the pad such as flow rate, the load carrying capacity and the static stiffness of the pad which the comparison of these obtained results with both LP and DP models presents a very satisfying accuracy.

The dynamic test bench is a bit more complicated as it also hires a shaker in order to apply a harmonic imposed vibration to the air gap under the pad. The dynamic stiffness and damping of the pad in a specific range of imposed frequency are obtained and compared with LP model. About the comparison between the LP and DP models, it is evident that the LP model with no correction works properly for estimating the damping, but it underestimates the stiffness, especially at low air gaps. With the correction factor of 0.3, the LP model is in a better accordance with the DP model, also at low air gaps. Therefore, the use of a correction factor seems necessary for improving the accuracy of the LP model specially for the low air gaps. while for the higher air gaps it seems to be enough accurate as expected.

## 8.2 Future work

According to the geometry dependency of the developed lumped model, the model is implemented for the rectangular aerostatic air bearings but in industry of air pads there are variety of shapes and geometry which makes the operation of the LP model limited. Therefore, for the future perspective the most important point to improve the LP model can be mentioned as improvements in order to be used regardless of the geometry. The geometry dependence cannot be removed all at once or it might be difficult, for these cases a proper alternative can be extension of the geometry dependent LP model also for other air pads including for example circular pads which are in a vast use in the current industry.

Another future work is to improve the accuracy of the model by modifying the resistances inside the pad in the path of the air flow, and modifying the equivalent electric circuit of the pad. In fact, during this research there were several modification of the resistances and the equivalent model of the pad which finally leaded to obtaining the current model with the most accuracy in comparison with previous models. The explanation of the primary models are out of scope of this thesis but it should be mentioned that modifying the equivalent resistances may lead to a model with better accuracy even for load air gaps in order to have enough accurate LP model even for low air gaps without a correcting factor $\Omega$.

Another to be done should be mentioned as comparing the developed model with other methods rather than just experimental results and results of the DP model. As an example, CFD models or finite element models implemented in COMSOL can be proper additional for more comprehensive validation of the developed LP model.

# References

[1] GE Willis and JW Deardorff. “A laboratory model of diffusion into the convective planetary boundary layer”. In: *Quarterly Journal of the Royal Meteorological Society* 102.432 (1976), pp. 427–445.

[2] J. McHugh. “Albert Kingsbury – His Life and Times.” In: *SV Sound Vibration* 37.10 (2003), pp. 12–20.

[3] JEL Simmons and SD Advani. “Michell and the development of tilting pad bearing”. In: (1987), pp. 49–56.

[4] H Mizumoto, T Matsubara, N Hata, and M Usuki. “Zero-compliance aerostatic bearing for an ultra-precision machine”. In: *Precision Engineering* 12.2 (1990), pp. 75–80.

[5] Arnold Sommerfeld. “Zur Theorie der Schmiermittelreibung”. In: *Electrical Engineering (Archiv fur Elektrotechnik)* 3.1 (1914), pp. 1–5.

[6] WJ Harrison. “The hydrodynamical theory of lubrication with special reference to air as a lubricant”. In: *Trans. Cambridge Philos. Soc.* 22 (1913), pp. 39–54.

[7] W Stone. “A proposed method for solving some problems in lubrication”. In: *The Commonwealth Engineer* 9 (1921), p. 115.

[8] A Stodola. “Kritische Wellenstörung infolge der Nachgiebigkeit des Oelpolsters im Lager”. In: *Schweizerische Bauzeitung* 85.21 (1925), pp. 265–266.

[9] Herbert Walker Swift. “Fluctuating Loads in Sleeve Bearings.” In: *Journal of the Institution of Civil Engineers* 5.4 (1937), pp. 161–195.

[10] William H Roudebush. “An analysis of the effect of several parameters on the stability of an air-lubricated hydrostatic thrust bearing”. In: (1957).

[11] William A Gross. *Gas film lubrication.* Wiley, 1962.

[12] John W Powell. “Design of aerostatic bearings”. In: (1970).

[13] Donald F Wilcock. “Externally pressurized bearings as servomechanisms. I—The simple thrust bearing”. In: *Journal of Lubrication Technology* 89.4 (1967), pp. 418–424.

[14] Michael R Bryant, Steven A Velinsky, Norman H Beachley, and Frank J Fronczak. “A design methodology for obtaining infinite stiffness in an aerostatic thrust bearing”. In: *Journal of Mechanisms, Transmissions, and Automation in Design* 108.4 (1986), pp. 448–453.

[15] P Plessers and R Snoeys. "Dynamic stability of mechanical structures containing externally pressurized gas-lubricated thrust bearings". In: *Journal of tribology* 110.2 (1988), pp. 271–278.

[16] E Blondeel, R Snoeys, and L Devrieze. "Dynamic stability of externally pressurized gas bearings". In: *Journal of Lubrication Technology* 102.4 (1980), pp. 511–519.

[17] Terenziano Raparelli, Vladimir Viktorov, Federico Colombo, and Luigi Lentini. "Aerostatic thrust bearings active compensation: Critical review". In: *Precision Engineering* 44 (2016), pp. 1–12.

[18] W Brian Rowe. *Hydrostatic, aerostatic, and hybrid bearing design.* Elsevier, 2012.

[19] Donald F Wilcock. "Externally pressurized bearings as servomechanisms. I—The simple thrust bearing". In: *Journal of Lubrication Technology* 89.4 (1967), pp. 418–424.

[20] G Belforte, T Raparelli, V Viktorov, and A Trivella. "Discharge coefficients of orifice-type restrictor for aerostatic bearings". In: *Tribology International* 40.3 (2007), pp. 512–521.

[21] PM Newgard and RL Kiang. "Elastic orifices for pressurized gas bearings". In: *ASLE TRANSACTIONS* 9.3 (1966), pp. 311–317.

[22] GTF KILMISTER. "A self-compensating flow restrictor for externally-pressurised bearings(Stiffness and load capacity control by self compensating flow restrictor for externally pressurized gas lubricated thrust bearing design)". In: (1971).

[23] WB Rowe and GTF Kilmister. "A theoretical and experimental investigation of a self-compensating externally pressurised thrust bearing". In: *International Gas Bearing Symposium, 6 th, Southampton, England.* 1974.

[24] IRG Lowe. "Characteristics of externally pressurised thrust bearings with one compliant surface". In: *International Gas Bearing Symposium, 6 th, Southampton, England.* 1974.

[25] E Blondeel. "Externally Pressurized Bearings with Varizble GapGeometries". In: *7th Gas Bearing Symp., Paper E2.* 1976.

[26] C Cusano Ms. "Characteristics of Externally Pressurized Journal Bearings with Membrane-Type Variable-Flow Restrictors as Compensating Elements". In: *Proceedings of the Institution of Mechanical Engineers* 188.1 (1974), pp. 527–536.

[27] Ming-Fei Chen and Yu-Ting Lin. "Dynamic analysis of the X-shaped groove aerostatic bearings with disk-spring compensator". In: *JSME International Journal Series C Mechanical Systems, Machine Elements and Manufacturing* 45.2 (2002), pp. 492–501.

[28] Guido Belforte, Federico Colombo, Terenziano Raparelli, Andrea Trivella, and Vladimir Viktorov. "Comparison between grooved and plane aerostatic thrust bearings: static performance". In: *Meccanica* 46.3 (2011), pp. 547–555.

[29] Wei Long and Gang Bao. “Entrance effect on load capacity of orifice compensated aerostatic bearing with feeding pocket”. In: *Chinese journal of mechanical engineering* 4 (2010), p. 451.

[30] Stefano Morosi and Ilmar F Santos. “Active lubrication applied to radial gas journal bearings. Part 1: Modeling”. In: *Tribology International* 44 (2011), pp. 1949–1958.

[31] Fabian G Pierart and Ilmar F Santos. “Active lubrication applied to radial gas journal bearings. Part 2: modelling improvement and experimental validation”. In: *Tribology International* 96 (2016), pp. 237–246.

[32] Hiroshi Mizumoto, Shiro Arii, Yoshihiro Kami, Kenji Goto, Tsuyoshi Yamamoto, and Masashi Kawamoto. “Active inherent restrictor for air-bearing spindles”. In: *Precision Engineering* 19.2-3 (1996), pp. 141–147.

[33] H Mizumoto, T Matsubara, H Yamamoto, K Okuno, and M Yabuya. “An infinite-stiffness aerostatic bearing with an exhaust-control restrictor”. In: *Progress in Precision Engineering*. Springer, 1991, pp. 315–316.

[34] Gorka Aguirre, Farid Al-Bender, and Hendrik Van Brussel. “A multiphysics coupled model for active aerostatic thrust bearings”. In: *Advanced Intelligent Mechatronics, 2008. AIM 2008. IEEE/ASME International Conference on.* IEEE. 2008, pp. 710–715.

[35] Farid Al-Bender. “On the modelling of the dynamic characteristics of aerostatic bearing films: From stability analysis to active compensation”. In: *Precision Engineering* 33.2 (2009), pp. 117–126.

[36] Federico Colombo, Luigi Lentini, Terenziano Raparelli, and Vladimir Viktorov. “Actively compensated aerostatic thrust bearing: design, modelling and experimental validation”. In: *Meccanica* 52.15 (2017), pp. 3645–3660.

[37] G Aguirre, F Al-Bender, and H Van Brussel. “Dynamic stiffness compensation with active aerostatic thrust bearings”. In: *Proceedings of ISMA*. 2008, pp. 105–118.

[38] Danial Ghodsiyeh, Federico Colombo, Terenziano Raparelli, Andrea Trivella, and Vladimir Viktorov. “Diaphragm valve-controlled air thrust bearing”. In: *Tribology International* 109 (2017), pp. 328–335.

[39] M Moradi, F Colombo, T Raparelli, A Trivella, and V Viktorov. “Dynamic lumped model of externally pressurized rectangular air bearings”. In: *Precision Engineering* (2018).

[40] Abderafi Charki, Khadim Diop, Stéphane Champmartin, and Abdelhak Ambari. “Numerical simulation and experimental study of thrust air bearings with multiple orifices”. In: *International Journal of Mechanical Sciences* 72 (2013), pp. 28–38.

[41] Ding HA Li YU. “Influences of the geometrical parameters of aerostatic thrust bearing with pocketed orifice-type restrictor on its performance”. In: *Tribology international* 40.7 (2007), pp. 1120–1126.

[42] Anton van Beek and Ron AJ van Ostayen. “The design of partially grooved externally pressurized bearings”. In: *Tribology international* 39.8 (2006), pp. 833–838.

[43] F Colombo, L Lentini, T Raparelli, A Trivella, and V Viktorov. “Dynamic model of a grooved thrust bearing: numerical model and experimental validation”. In: 4 (2017), pp. 506–517.

[44] G Belforte, T Raparelli, V Viktorov, and A Trivella. “Permeability and inertial coefficients of porous media for air bearing feeding systems”. In: *Journal of Tribology* 129.4 (2007), pp. 705–711.

[45] G Belforte, T Raparelli, V Viktorov, and A Trivella. “Metal woven wire cloth feeding system for gas bearings”. In: *Tribology International* 42.4 (2009), pp. 600–608.

[46] Guido Belforte, Federico Colombo, Terenziano Raparelli, Andrea Trivella, and Vladimir Viktorov. “Comparison between grooved and plane aerostatic thrust bearings: static performance”. In: *Meccanica* 46.3 (2011), pp. 547–555.

[47] BC Majumdar. “Dynamic characteristics of externally pressurized rectangular porous gas thrust bearings”. In: *Journal of Lubrication Technology* 98.1 (1976), pp. 181–186.

[48] Ming-Fei Chen and Yu-Ting Lin. “Static behavior and dynamic stability analysis of grooved rectangular aerostatic thrust bearings by modified resistance network method”. In: *Tribology International* 35.5 (2002), pp. 329–338.

[49] Masaaki Miyatake and Shigeka Yoshimoto. “Numerical investigation of static and dynamic characteristics of aerostatic thrust bearings with small feed holes”. In: *Tribology International* 43.8 (2010), pp. 1353–1359.

[50] Uichiro Nishio, Kei Somaya, and Shigeka Yoshimoto. “Numerical calculation and experimental verification of static and dynamic characteristics of aerostatic thrust bearings with small feedholes”. In: *Tribology International* 44.12 (2011), pp. 1790–1795.

[51] F Mohamed. “Prediction of the stability of air thrust bearing by numerical analytical and experiment methods”. In: *Wear* 198 (1996), pp. 1–6.

[52] YT Li and Han Ding. “Design analysis and experimental study of aerostatic linear guideways used in a high acceleration and high precision xy stage”. In: *Proceedings of the Institution of Mechanical Engineers, Part J: Journal of Engineering Tribology* 221.1 (2007), pp. 1–9.

[53] Haijun Zhang, Changsheng Zhu, and Qin Yang. “Approximate numerical solution of hydrodynamic gas journal bearings”. In: *International Conference on Intelligent Robotics and Applications*. Springer. 2008, pp. 260–268.

[54] Jyh-Chyang Renn and Chih-Hung Hsiao. “Experimental and CFD study on the mass flow-rate characteristic of gas through orifice-type restrictor in aerostatic bearings”. In: *Tribology International* 37.4 (2004), pp. 309–315.

[55] Siyu Gao, Kai Cheng, Shijin Chen, Hui Ding, and Hongya Fu. “CFD based investigation on influence of orifice chamber shapes for the design of aerostatic thrust bearings at ultra-high speed spindles”. In: *Tribology international* 92 (2015), pp. 211–221.

[56] Jyh-Chyang Renn and Jia-feng Yang. “A new mass flow-rate model of gas through orifice-type restrictors in aerostatic bearings”. In: *In proceeding of the JFPS In ternational Symposium on Fluid Power* 2005 (2005), pp. 760–765.

[57] Guido Belforte, Terenziano Raparelli, Andrea Trivella, Vladimir Viktorov, and Carmen Visconte. “Cfd analysis of aerostatic pads with simple orifice-type feeding system.” In: *Tribology Letters* 58.2 (2015), p. 25.

[58] Mohamed E Eleshaky. “CFD investigation of pressure depressions in aerostatic circular thrust bearings”. In: *Tribology International* 42.7 (2009), pp. 1108–1117.

[59] Brian H Thornton and David B Bogy. “Nonlinear aspects of air-bearing modeling and dynamic spacing modulation in sub-5-nm air bearings for hard disk drives”. In: *IEEE Transactions on Magnetics* 39.2 (2003), pp. 722–728.

[60] A Andrisano and A Maggiore. “Theoretical and experimental analysis of an externally pressurized porous gas thrust bearing”. In: *TRIBOLOGY international* 11.5 (1978), pp. 285–288.

[61] Danial Ghodsiyeh, Federico Colombo, Terenziano Raparelli, Andrea Trivella, and Vladimir Viktorov. “Diaphragm valve-controlled air thrust bearing”. In: *Tribology International* 109 (2017), pp. 328–335.

[62] Roberto Bassani, Enrico Ciulli, and Paola Forte. “Static behaviour of an integral externally pressurized gas bearing—comparison with other types of bearing”. In: *Tribology international* 22.3 (1989), pp. 177–188.

[63] F Colombo, D Ghodsiyeh, T Raparelli, A Trivella, and V Viktorov. “Theoretical and experimental study of a rectangular grooved air pad”. In: (2016), pp. 1–2.

[64] F Colombo, D Ghodsiyeh, T Raparelli, A Trivella, and V Viktorov. “Dynamic behavior of a rectangular grooved air pad”. In: (2017), pp. 7–9.

[65] Federico Colombo, Terenziano Raparelli, Andrea Trivella, and Vladimir Viktorov. “Lumped parameters models of rectangular pneumatic pads: static analysis”. In: *Precision Engineering* 42 (2015), pp. 283–293.

[66] Federico Colombo, Luigi Lentini, Terenziano Raparelli, Andrea Trivella, and Vladimir Viktorov. “Dynamic Characterisation of Rectangular Aerostatic Pads with Multiple Inherent Orifices Manuscript Number”. In: *Triboloy Letters* 5.1 (1962), pp. 254–260.

[67] Federico Colombo, Terenziano Raparelli, Andrea Trivella, and Vladimir Viktorov. “Investigation on the discharge coefficient of supply micro holes for gas bearings”. In: *5th World Tribology Congress, Sept. 8-13, Torino* (2013).

[68] Federico Colombo, Terenziano Raparelli, Andrea Trivella, and Vladimir Viktorov. “Lumped parameters models of rectangular pneumatic pads: static analysis”. In: *Precision Engineering* 42 (2015), pp. 283–293.

[69] G Belforte, F Colombo, T Raparelli, A Trivella, and V Viktorov. “Experimental analysis of air pads with micro holes”. In: *Tribology Transactions* 56.2 (2013), pp. 169–177.

[70] DC Allais. “The design of externally pressurized gas thrust bearings for maximum stiffness and stability”. In: *ASLE TRANSACTIONS* 5.1 (1962), pp. 254–260.

[71] Federico Colombo, Mona Moradi, Terenziano Raparelli, Andrea Trivella, and Vladimir Viktorov. “Evaluation of squeeze effect in a gas thrust bearing”. In: *8th International Conference on Computational Methods and Experiments in Material and Contact Characterisation* (2017).

[72] Mihai Arghir and Pierre Matta. “Compressibility effects on the dynamic characteristics of gas lubricated mechanical components”. In: *Comptes Rendus Mécanique* 337.11-12 (2009), pp. 739–747.